

**SYNTHESIS AND ELECTROCHEMICAL STUDY OF PALLADIUM-  
BASED NANOMATERIALS FOR GREEN ENERGY APPLICATIONS**

**A Thesis Presented to  
The Faculty of Graduate Studies  
Lakehead University**

**By  
CASSANDRA K. OSTROM**

**In partial fulfillment of the requirements for the degree of  
Master of Science  
September 2013**

**© Cassandra K. Ostrom, 2013**

## Abstract

Rising global energy consumption leads to increased environmental impacts. The continued use of current energy resources, e.g. fossil fuels, will exaggerate the cumulative nature of CO<sub>2</sub> byproduct emissions in the atmosphere. The development and implementation of a hydrogen economy, as a solution to offset degradative environmental impacts, will likely enable opportunities for maintaining or improving standards of living while significantly lowering carbon emissions. Palladium has proven to be a strong contender as an enabling material that encompasses many aspects of a prospective hydrogen economy, lending promise to applications such as hydrogen purification, storage and fuel cell catalysis. In my M.Sc. study, Pd-based nanomaterials have been synthesized and examined for their applications in hydrogen storage and fuel cell catalysis. The surface properties of synthesized Pd-based nanomaterials were characterized by scanning electron microscopy (SEM), transmission electron microscopy (TEM), energy dispersive X-ray spectrometry (EDS), X-ray diffraction (XRD), X-ray Photoelectron spectroscopy (XPS), and N<sub>2</sub> gas adsorption/desorption. Electrochemical analysis of the fabricated materials was performed using cyclic voltammetry (CV), linear sweep voltammetry (LSV), chronoamperometry (CA), and electrochemical impedance spectroscopy (EIS). Inductively coupled plasma atomic emission spectroscopy (ICP-AES) was employed to characterize the composition of the formed samples.

Hydrogen electrosorption onto activated carbon materials modified with different tri-metallic dissociation catalysts (Pd-Ag-Cd) was investigated in an acidic medium. A uniform distribution of the Pd-Ag-Cd catalysts was achieved using a facile room temperature sodium borohydride reduction method. By varying the composition of the alloys, synergistic effects between the metal and carbon support resulted in drastic increases in hydrogen sorption

capabilities in contrast to bi-metallic PdAg and PdCd catalysts. Utilizing electrochemical methods, the optimal composition of the Pd-Ag-Cd alloys was determined to be Pd<sub>80</sub>Ag<sub>10</sub>Cd<sub>10</sub>, with the highest hydrogen sorption capacity at a hydrogen desorption charge of 18.49 C/cm<sup>2</sup>·mg.

Further enhancement of the electroactivity of synthesized titanium dioxide nanotubes (TiO<sub>2</sub> NTs) was achieved using UV light and electrochemical pretreatment methods. The effects of these pretreatment methods on TiO<sub>2</sub> NTs were systematically investigated and compared. Using Pd as a dispersed catalyst, Pd/TiO<sub>2</sub> NT electrodes were examined in acidic medium, with both UV and electrochemical pretreatment methods revealing significant enhancements in the electroactivity of the TiO<sub>2</sub> NT substrate. The UV pretreated samples were found to dominate, when compared to those that underwent electrochemical pretreatment, in terms of overall efficacy for hydrogen sorption and the electrooxidation of formic acid. Improvements in nanotube conductivity resulted in an effective reduction of noble metal coating loads.

Nanostructured PdPb electrocatalysts were loaded directly onto TiO<sub>2</sub> NT substrates and tested for their activity towards formic acid oxidation. Comparative studies revealed the enhanced electrochemical oxidation of formic acid on Pd<sub>95</sub>Pb<sub>5</sub>/TiO<sub>2</sub> NTs in comparison to Pd/TiO<sub>2</sub> NTs, resulting in the successful reduction of Pd noble metal load.

The work performed in this M. Sc. thesis project reveals that modifications to both Pd catalysts and their associated supports can drastically alter their geometric and electronic properties. This has a major influence on the development of more cost effective materials with enhanced activity for use towards the commercialization of fuel cells.

“Every kid starts out as a natural-born scientist, and then we beat it out of them. A few trickle through the system with their wonder and enthusiasm for science still intact.”  
– Carl Sagan.

## **Acknowledgements**

First and foremost, I would like to express my heartfelt gratitude to my supervisor, Dr. Aicheng Chen, for his patience and knowledge throughout the course of my M.Sc. degree. His support during my research has given me the confidence and tools required for a successful future in this field. I would also like to thank my committee members, Dr. MacKinnon and Dr. Mawhinney, for their feedback on my thesis.

An extended thank you goes out to the entire Lakehead University Chemistry Department and to Graduate Studies. As well, thank you to Al MacKenzie and Dr. Guosheng Wu and Jiali Wen for their assistance in the Lakehead University Instrumentation Lab. The Surface Interface Ontario/Chemical Engineering & Applied Chemistry at the University of Toronto for carrying out the XPS analysis.

All my fellow lab members, both current and former, of Dr. Chen's research group deserve acknowledgement. For their direct aid in the development of my thesis I especially want to thank, Dr. Guosheng Wu, Dr. Min Tian, Jiali Wen, Sapanbir Thind, Brian Adams, Shuai Chen, Xin Chang, Kevin Gagnon, and Frank Boehm.

Last, but not least, I would like to extend my deepest appreciation to my family and close friends. Without their support, encouragement, and sense of humor in times of need, I would not have been able to accomplish what I have.

## Table of Contents

Abstract .....	i
Acknowledgements .....	iv
Table of Contents .....	v
List of Tables .....	viii
List of Figures .....	ix
List of Abbreviations and Symbols.....	xii
Chapter 1: Introduction	
1.1 The Hydrogen Economy.....	1
1.2 Role of Fuel Cells & Hydrogen .....	3
1.3 Hydrogen Purification & Storage Properties of Palladium.....	7
1.4 Palladium in Fuel Cell Catalysis.....	12
1.5 Stimulus and Scope of This Thesis .....	13
References.....	14
Chapter 2: Experimental Methods	
2.1 Introduction.....	19
2.2 Chemicals and Materials .....	19
2.3 Fabrication of Nanomaterials.....	20
2.4 Surface Analysis.....	22
2.5 Electrochemical Experiments.....	23
2.6 Gas Sorption Studies.....	23
2.7 Summary .....	24
References .....	24

Chapter 3:	Synthesis and Electrochemical Study of Pd-based Tri-metallic Nanoparticles for Enhanced Hydrogen Storage	
3.1	Introduction.....	25
3.2	Experimental Section.....	26
3.3	Surface Analysis of Catalyst Dispersed on Activated Carbon.....	28
3.4	General Cyclic Voltammetric Behaviors of the Pd-based Catalysts.....	36
3.5	Potential and Composition Dependence of Pd-based Catalysts on Hydrogen Electrosorption.....	38
3.6	Synergistic Effects of Activated Carbon Supported PdAg <sub>10</sub> Cd <sub>10</sub> Nanoparticles.....	42
3.7	Conclusions.....	47
	References.....	48
Chapter 4:	Enhanced Electrocatalytic Activity of Pd Nanoparticle Modified TiO <sub>2</sub> Nanotubes: A Comparison of UV and EC Pretreatment Methods	
4.1	Introduction.....	51
4.2	Experimental Section.....	52
4.3	Surface Analysis of the TiO <sub>2</sub> NT Electrodes.....	53
4.4	General Cyclic Voltammetric Behaviour of the Pd/TiO <sub>2</sub> NT Nanostructures.....	54
4.5	Electrosorption of Hydrogen.....	58
4.5.1	Potential and Treatment Method Dependence of Hydrogen Electrosorption in the Pd/TiO <sub>2</sub> NT Nanostructures.....	58
4.5.2	Kinetics of Hydrogen Electrosorption Pd/TiO <sub>2</sub> NT Nanostructures.....	63
4.6	Electrooxidation of Formic Acid on Pd/TiO <sub>2</sub> NT Nanostructures.....	65
4.7	Conclusions.....	70
	References.....	70
Chapter 5:	Palladium-Lead Nanoparticles deposited on TiO <sub>2</sub> Nanotubes towards Formic Acid Electro-oxidation	

5.1	Introduction .....	73
5.2	Experimental Section .....	74
5.3	Surface Analysis of the TiO <sub>2</sub> NT electrodes .....	75
5.4	General Cyclic Voltammetric Behaviour of the Pd, Pb and PdPb/TiO <sub>2</sub> NT Nanostructures .....	76
5.5	Electrooxidation of Formic Acid on Pd, Pb and Pb-based/TiO <sub>2</sub> NT Nanostructures .....	80
5.6	Conclusions .....	85
	References .....	85
Chapter 6: Summary and Future Work		
6.1	Synthesis and Electrochemical Study of Pd-based Tri-metallic Nanoparticles for Enhanced Hydrogen Storage .....	88
6.2	Enhanced Electrocatalytic Activity of Pd Nanoparticle Modified TiO <sub>2</sub> Nanotubes: A Comparison of UV and EC Pretreatment Methods .....	89
6.3	Palladium-Lead Nanoparticles Deposited on TiO <sub>2</sub> Nanotubes towards Formic Acid Electro-oxidation .....	90
6.4	Closing Remarks and Future Work .....	90

## List of Tables

<b>Table 1.1.</b> General characteristics of five types of fuel cells. ....	4
<b>Table 1.2</b> Hydrogen storage properties of intermetallic compounds. ....	10
<b>Table 3.1.</b> ICP results of the concentrations of Pd <sup>2+</sup> , Ag <sup>+</sup> , and Cd <sup>2+</sup> remaining in solution following NaBH <sub>4</sub> reduction. Initial concentrations were calculated based on the amount of Pd(NO <sub>3</sub> ) <sub>2</sub> , AgNO <sub>3</sub> , and Cd(NO <sub>3</sub> ) <sub>2</sub> added. ....	30
<b>Table 3.2.</b> Textural parameters of metal dispersed activated carbon samples from N <sub>2</sub> adsorption/absorption isotherms at 77 K. ....	36

## List of Figures

<b>Figure 3.1.</b> TEM images of Pd/PAC200 (a), PdAg <sub>5</sub> Cd <sub>15</sub> /PAC200 (b), PdAg <sub>10</sub> Cd <sub>10</sub> /PAC200 (c) and PdAg <sub>15</sub> Cd <sub>5</sub> /PAC200 (d).....	29
<b>Figure 3.2.</b> XPS comparative survey of palladium, silver and cadmium content samples (a); high resolution spectra of the Pd 3d region (b); Ag 3d region (c) and Cd 3d region (d) of PdAg <sub>10</sub> Cd <sub>10</sub> supported on PAC200. For the high resolution spectra, dots, dashed lines, and red, blue, and black lines represent the raw data, baseline, individual components (zero and high oxidation states), and total fit, respectively.....	31
<b>Figure 3.3.</b> EDX mapping distribution images of PAC200 (a), Pd (b), Ag (c) and Cd (d) content for PdAg <sub>10</sub> Cd <sub>10</sub> /PAC200 sample.....	33
<b>Figure 3.4.</b> N <sub>2</sub> adsorption/desorption isotherm at 77 K on the PdAg <sub>10</sub> Cd <sub>10</sub> /PAC200 sample (a), and corresponding desorption curve fitted using QSDFT method (b). The pore size distributions using QSDFT method are shown in (c). .....	34
<b>Figure 3.5.</b> Cyclic voltammograms of the Pd-based nanostructures in 0.5 M H <sub>2</sub> SO <sub>4</sub> at a scan rate of 5 mV/s.....	37
<b>Figure 3.6.</b> Anodic sweeps of desorption of hydrogen from Pd/PAC200 (a) and PdAg <sub>10</sub> Cd <sub>10</sub> /PAC200 (b) after holding the potential at various cathodic limits for one min in 0.5 M H <sub>2</sub> SO <sub>4</sub> . The scan rate was 5 mV/s.....	39
<b>Figure 3.7.</b> The overall hydrogen oxidation charges (Q <sub>H</sub> ) for each Pd based sample at various cathodic limits. ....	41
<b>Figure 3.8.</b> Cyclic voltammogram of the PAC200 sample in 0.5 M H <sub>2</sub> SO <sub>4</sub> at a scan rate of 5 mV/s.....	44
<b>Figure 3.9.</b> Cyclic voltammogram of the PdAg <sub>10</sub> Cd <sub>10</sub> nanostructures in 0.5 M H <sub>2</sub> SO <sub>4</sub> at a scan rate of 5 mV/s. ....	44
<b>Figure 3.10.</b> Anodic sweeps of desorption of hydrogen from PdAg <sub>10</sub> Cd <sub>10</sub> after holding the potential at various cathodic limits for one min in 0.5 M H <sub>2</sub> SO <sub>4</sub> . The scan rate was 5 mV/s. Hydrogen desorption charge (Q <sub>H</sub> ) of the PdAg <sub>10</sub> Cd <sub>10</sub> nanoparticles versus potential is shown in the inset. ....	45
<b>Figure 3.11.</b> Anodic sweeps of the PdAg <sub>10</sub> Cd <sub>10</sub> /PAC200 and PdAg <sub>10</sub> Cd <sub>10</sub> nanoparticle samples after holding the potential at -250 mV for one min. in 0.5 M H <sub>2</sub> SO <sub>4</sub> at a scan rate of 5 mV/s are shown in (a). Note: the PdAg <sub>10</sub> Cd <sub>10</sub> non-supported sample's current density (j) is multiplied by a factor of 50 for viewing purposes. Corresponding ratios of charge due to hydrogen desorption versus potential (b) follows.....	46

<b>Figure 4.1.</b> SEM images of TiO <sub>2</sub> NTs (a), at 50,000 × magnification. EDX spectra (b) and XRD patterns (c) of the prepared TiO <sub>2</sub> NT samples before and after UV and EC pretreatment. Defraction peaks belonging to the Ti substrate and the anatase phase of the TiO <sub>2</sub> NTs are labeled with (*) .....	55
<b>Figure 4.2.</b> SEM images of Pd-doped TiO <sub>2</sub> NT with UV pretreatment (a), and EC pre-treatment (b), at 50,000 × magnification, and EDX spectra of the samples (c).....	56
<b>Figure 4.3.</b> Cyclic voltammograms of TiO <sub>2</sub> NTs after varying treatment methods in 0.5M H <sub>2</sub> SO <sub>4</sub> at a scan rate of 20 mV/s. ....	57
<b>Figure 4.4.</b> Cyclic voltammograms of Pd-doped TiO <sub>2</sub> NTs in 0.5M H <sub>2</sub> SO <sub>4</sub> at a scan rate of 20 mV/s.....	59
<b>Figure 4.5.</b> Anodic sweeps of desorption of hydrogen from untreated (a), UV treated (b), and EC treated (c) Pd/TiO <sub>2</sub> NTs after holding the potential at various cathodic limits for ten minutes in 0.5M H <sub>2</sub> SO <sub>4</sub> . The scan rate was 20 mV/s. ....	60
<b>Figure 4.6.</b> Hydrogen oxidation charges (Q <sub>H</sub> ) versus potential for the prepared Pd/TiO <sub>2</sub> NT electrodes at various cathodic limits. ....	62
<b>Figure 4.7.</b> The time necessary for obtaining steady state saturation of the Pd/TiO <sub>2</sub> NT electrodes with absorbed hydrogen with respect to potential. ....	64
<b>Figure 4.8.</b> Linear sweep voltammograms of Pd/TiO <sub>2</sub> NT electrodes in 0.5 M H <sub>2</sub> SO <sub>4</sub> + 0.1 M HCOOH at a scan rate of 20 mV/s.....	66
<b>Figure 4.9.</b> Amperometric <i>i-t</i> curves of HCOOH electro-oxidation on the Pd/TiO <sub>2</sub> NTs in 0.5 M H <sub>2</sub> SO <sub>4</sub> + 0.1 M HCOOH at a potential of 100 mV (a) and 200 mV (b) vs. Ag/AgCl. ....	68
<b>Figure 4.10.</b> Mott-Schottky plot of the TiO <sub>2</sub> nanotubes in 0.5 M H <sub>2</sub> SO <sub>4</sub> at 1000 Hz without (grey) and with (blue + red) pre-treatment. UV pre-treatment (a) and EC pre-treatment (b) of Pd/TiO <sub>2</sub> NT Mott-Schottky plot is shown in the inset. ....	69
<b>Figure 5.1.</b> SEM images at 15,000× magnification of Pd (a) and PdPb <sub>5</sub> (b) deposited TiO <sub>2</sub> NT samples.....	77
<b>Figure 5.2.</b> EDX spectra of pure Pd and PdPb <sub>5</sub> nanoparticles deposited on the TiO <sub>2</sub> NT substrates. ....	78
<b>Figure 5.3.</b> Cyclic voltammograms of the Pd-based nanoparticles recorded in 0.5 M H <sub>2</sub> SO <sub>4</sub> at a scan rate of 20 mV/s.....	79
<b>Figure 5.4.</b> Linear sweep voltammograms of Pd-based/TiO <sub>2</sub> NT electrodes recorded in 0.5 M H <sub>2</sub> SO <sub>4</sub> + 0.1 M HCOOH at a scan rate of 20 mV/s. ....	81

**Figure 5.5.** Chronoamperometric curves for the electrooxidation of HCOOH on the Pd and PdPb catalysts recorded in 0.5 M H<sub>2</sub>SO<sub>4</sub> + 0.1 M HCOOH at a potential of 150 mV vs. Ag/AgCl ..... 82

**Figure 5.6.** Mott-Schottky plot of the Pd and PdPb doped TiO<sub>2</sub> nanotubes in 0.5 M H<sub>2</sub>SO<sub>4</sub> at 500 Hz after UV pretreatment..... 84

## List of Abbreviations and Symbols

Abbreviation	Name
AFC	Alkaline Fuel Cell
BET	Brunauer-Emmett-Teller
BCC	Body-Centred Cubic
BJH	Barrett-Joyner-Halenda
C	Capacitance
CA	Chronoamperometry
CV	Cyclic Voltammetry
DA	Dubinin-Astakhov
DEFC	Direct Ethanol Fuel Cell
DFAFC	Direct Formic Acid Fuel cell
DMFC	Direct Methanol Fuel Cell
E	Potential
EDX	Energy Dispersive X-ray Spectroscopy
EIS	Electrochemical Impedance Spectroscopy
GCE	Glassy Carbon Electrode
ICP-AES	Inductively Coupled Plasma Atomic Emission Spectroscopy
j	Current Density
LSV	Linear Sweep Voltammetry
MCFC	Molten Carbonate Fuel Cell
$N_D$	Donor Density
NT	Nanotube
PAC200	Commercially Available Norit Powdered Activated Carbon

PAFC	Phosphoric Acid Fuel Cell
PEMFC	Proton Exchange Membrane Fuel Cell
$Q_H$	Hydrogen Oxidation Charge
QSDFT	Quenched Solid Density Functional Theory
SEM	Scanning Electron Microscopy
SOFC	Solid Oxide Fuel Cell
TEM	Transition Electron Microscopy
UV	Ultraviolet
XPS	X-ray Photoelectron Spectroscopy
XRD	X-ray Diffraction

## Chapter 1. Introduction

A significant growth in global energy consumption is inevitable as both worldwide population and the standards of living increase.<sup>1</sup> At the same time, current global energy use only exacerbates the cumulative nature of CO<sub>2</sub> emissions in the atmosphere.<sup>2</sup> Conventional fossil fuel derived energy resources could meet this increase in demand; however, they offer particularly undesirable effects. The avoidance of further progress towards climate change can only be achieved by altering the way that we currently consume and supply energy. Meeting the energy demands of the global growing population in an environmentally and economically sustainable fashion is arguably the most critical technological challenge that is faced by today's society.

### 1.1 The Hydrogen Economy

Over the past several decades global societies dependence on energy use has grown exponentially.<sup>1</sup> Technological advances lead to improved living conditions, but they often come at a cost. Half of all greenhouse gas emissions, as well as a large fraction of air pollutants, are byproducts of the combustion of fossil fuels for transportation and heating.<sup>3</sup> To offset negative environmental impacts, the idea of implementing a hydrogen economy has been suggested. The core objective of a hydrogen economy is to utilize renewable energy sources to generate hydrogen and then to harness the energy by means of combustion or with a fuel cell.<sup>4-6</sup> The overall goal is to produce an economy in which hydrogen is the main energy carrier in conjunction with electricity.<sup>5</sup>

Hydrogen itself possesses many unique characteristics that make it an ideal energy carrier.<sup>5,6</sup> Unlike fossil fuels, the combustion of hydrogen produces zero or near-zero emissions at the point of use and is a completely renewable fuel.<sup>3,5,7</sup> Hydrogen's multiple potential storage

modes (liquid/solid/gas) allow for the relative ease of transport. Further, energy stored in the form of hydrogen can be efficiently converted into various forms of usable energy.<sup>5-7</sup> However, the creation of a viable and sustainable hydrogen economy will necessitate a heavy reliance on technological advances.

The hydrogen economy spans three functional areas: production, storage and use, each with its own inherent technical challenges. Production of hydrogen can be achieved in a manner of ways, from logical sources such as hydrocarbon fuels ( $C_xH_y$ ) and water. Currently, the majority of  $H_2$  is produced via thermochemical methods by processing hydrocarbons such as natural gas, coal, biomass, or wastes to produce “syngas” composed of  $H_2$ ,  $CO$ ,  $CO_2$ ,  $H_2O$  and  $CH_4$ .<sup>3</sup> Further processing of the syngas results in an increase of hydrogen content at a desired purity. The use of syngas as a  $H_2$  supply can eliminate end use pollutant emissions; however, within the reforming process undesirable reactions occur. The creation of undesirable by-products through the use of hydrocarbons as a fuel source drives the development of alternative renewable energy production processes such as the electrolysis of water. The dissociation of water to its elemental constituents via the use of electricity is highly ideal in the sense of low environmental contaminant production and high hydrogen purity. Due to economical feasibility in several cases, hydrogen production via the electrolysis of water remains an area of ongoing research.<sup>3,5,6</sup>

The hydrogen economy requires two basic storage functions: hydrogen storage for stationary applications and for transportation. Although hydrogen has many ideal attributes, its characteristically low density needs to be addressed for application in practical settings. For instance, a key element to the hydrogen economy is the storage of hydrogen in a high energy density.<sup>1,3,5,6</sup> Current storage modes attempt to achieve efficient storage through various

alterations to the state of hydrogen. These modes of storage include: compressed hydrogen storage, cryogenic hydrogen storage and solid storage of hydrogen. For stationary applications, the weight and volume of the system employed are not a key factor. Regarding mobile applications, hydrogen tanks must be compact, lightweight, safe and affordable for practical use.

## **1.2 Role of Fuel Cells & Hydrogen**

Following the production of hydrogen, the energy can be harnessed either by combustion to produce heat or in a fuel cell to produce electricity.<sup>4-6</sup> A fuel cell is an electrochemical device that converts chemical energy into electricity. It does this through the combination of hydrogen, or a hydrogen containing fuel, and an oxidant (e.g. oxygen, either pure or in ambient atmosphere). Under the continuous supply of a fuel and oxidant, a fuel cell will continuously produce electricity on demand. For applications in transportation, stationary, and portable power, fuel cells offer several benefits. In contrast to other energy conversion devices, the advantages of high-efficiency energy conversion and low pollution output makes further fuel cell development very appealing.<sup>8,9</sup>

There are several types of fuels cells, each categorized according to the electrolyte used. Table 1.1 depicts the general characteristics of the principal fuel cells: proton exchange membrane fuel cells (PEMFCs), alkaline fuel cells (AFCs), phosphoric acid fuel cells (PAFCs), molten carbonate fuel cells (MCFCs) and solid oxide fuel cells (SOFCs).<sup>8-10</sup> Proton exchange membrane fuel cells have a subclass of their own, classified by the type of fuels used such as hydrogen, methanol, ethanol or formic acid. These small organic fuels give the fuel cell its name: hydrogen fuel cell, direct methanol fuel cell (DMFC), direct ethanol fuel cell (DEFC) and direct formic acid fuel cell (DFAFC). The fuel is fed directly into the fuel cell rather than being initially reformed into H<sub>2</sub>. This allows for a compact and lightweight design with a high

power density output at low temperatures. Compared to the other available fuel cells, PEMFCs offer superior characteristics that are essential for stationary power supplies, personal transportation applications, and small portable electronics.<sup>3,8-10</sup>

**Table 1.1.** General characteristics of five types of fuel cells.<sup>8,10</sup>

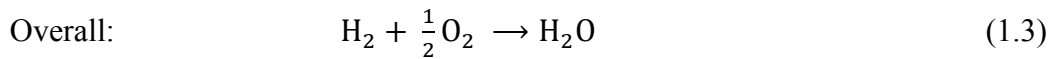
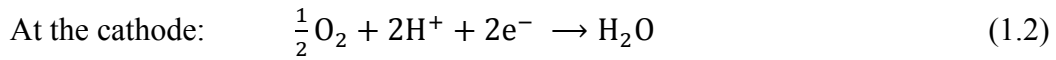
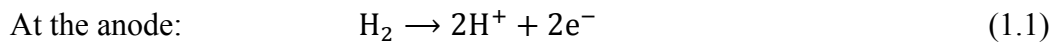
	<b>PEMFC</b>	<b>AFC</b>	<b>PAFC</b>	<b>MCFC</b>	<b>SOFC</b>
Primary Applications	Automotive and stationary power	Space vehicles and drinking water	Stationary power	Stationary power	Vehicle auxiliary power
Electrolyte	Polymer (plastic) membrane	Concentrated (30-50%) KOH in H <sub>2</sub> O	Concentrated 100% phosphoric acid	Molten Carbonate retained in a ceramic matrix of LiAlO <sub>2</sub>	Yttrium-stabilized Zirkondioxide
Operating Temperature Range	50-100°C	50-200°C	150-220°C	600-700°C	700-1000°C
Charge Carrier	H <sup>+</sup>	OH <sup>-</sup>	H <sup>+</sup>	CO <sub>3</sub> <sup>-2</sup>	O <sup>-2</sup>
Catalyst	Pt-based	Pt-based	Pt-based	Ni-based	Perovskites
Primary Fuel	H <sub>2</sub>	H <sub>2</sub>	H <sub>2</sub>	H <sub>2</sub> , CO, CH <sub>4</sub>	H <sub>2</sub> , CO
Start-up Time	Sec-min	Sec-min	Hours	Hours	Hours
Power Density (kW/m <sup>3</sup> )	3.8-6.5	~1	0.8-1.9	1.5-2.6	0.1-1.5
Combined Cycle Efficiency	50-60%	50-60%	55%	55-65%	55-65%

### 1.2.1 Hydrogen Fuel Cells

Proton exchange membrane fuel cells in their simplest form use hydrogen/oxygen as fuel. The basic components of a fuel cell include the anode, anodic catalyst layer, electrolyte, cathodic catalyst layer, and the cathode. Hydrogen is fed to the anode compartment, where it

splits into its primary constituents, protons and electrons. The protons pass through the membrane, leaving the electrons to pass through electrically conductive electrodes to generate an electric current. On the cathode side, oxygen diffuses through the membrane, splits up at the catalyst layer surface, and then reacts with both protons and electrons to form water. The net result of these simultaneous reactions is a flow of electrons creating a direct electrical current.<sup>9-</sup>

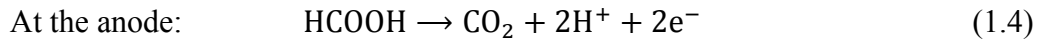
<sup>12</sup> The basic fuel cell reactions are:

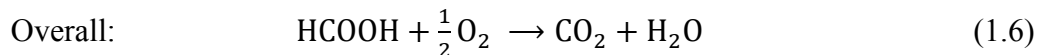
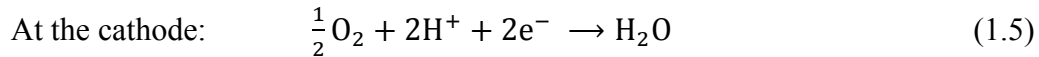


Hydrogen, like electricity, is not available in a freely usable form, but can be produced using primary energy sources. The main difference between the two is the end product, electrons or hydrogen molecules. The attraction of hydrogen as an energy currency is the clean emission prospects depending on the primary source used, as well as high electrochemical efficiency.<sup>3,5,8-12</sup> In order for the commercialized use of hydrogen, as a major energy carrier, technological advances in hydrogen production and storage need to be addressed.

### 1.2.2 Direct Formic Acid Fuel Cells (DFAFC)

Direct liquid fuel cells, unlike H<sub>2</sub>-fed PEMFCs, use liquid fuel fed to the anode in place of hydrogen. In the case of direct formic acid fuel cells (DFAFCs), formic acid is used as the hydrogen carrier. The cathodic, anodic and overall reactions of a direct formic acid fuel cell are as follows:





In recent years, direct formic acid fuel cells have received increased attention for applications towards miniaturized portable devices. Traditionally, H<sub>2</sub>-fed PEMFC and direct methanol fuel cells (DMFC) are considered dominant choices as candidates for the replacement of batteries and portable devices. However, inherent limitations for both remain an issue for commercialization. DFAFCs have a higher power output compared to that of other liquid fuel cells, and offer fast electro-oxidation while using a non-flammable, non-toxic, easily available fuel.<sup>13-15</sup> However, the use of small organic molecules (e.g. formic acid) comes with disadvantages. The electro-oxidation of formic acid (equation 1.6) produces CO<sub>2</sub>. Using DFAFCs would not directly reduce anthropogenic impacts on global warming, unless supplied from a renewable energy source.

The most commonly accepted mechanism for formic acid oxidation is the ‘parallel or dual pathway mechanism’. The first pathway is referred to as direct oxidation, which occurs via a dehydrogenation reaction, without forming CO as a reaction intermediate.<sup>13,14</sup> The second pathway forms adsorbed carbon monoxide (CO) onto the catalyst surface as a reaction intermediate, which is then oxidized into the gaseous CO<sub>2</sub> end product. This pathway occurs via dehydration and is referred to as indirect oxidation. In DFAFCs, the preferred reaction pathway is dehydrogenation. The dehydrogenation pathway enhances the overall cell efficiency and reduces the poisoning of the catalyst. Research into anode catalyst selection is fundamental in directing formic acid oxidation to the desired reaction pathway.<sup>14,15</sup>

### 1.3 Hydrogen Purification & Storage Properties of Palladium

In order for the hydrogen economy to be implemented in an economical fashion, the technological development challenges of hydrogen production and storage must be met. As previously discussed, the primary production of hydrogen is currently achieved via fossil fuels. The prospect of its alternative production through the electrolysis of water remains an ongoing area of research. The use of fossil fuels warrants concern due to the resulting greenhouse gas emissions. The electrolysis of water, on the other hand, when coupled with renewable energy sources, eliminates unwanted hazardous emissions.<sup>5</sup> In a fuel cell, electrical energy is generated by the exothermic oxidation of hydrogen. In reverse, the electrolysis of water entails the endothermic reaction, splitting of water into its primary constituents, using electricity:



The purity of the hydrogen fuel is crucial to the performance of PEMFCs. Depending on its desired use, certain species within the hydrogen stream can act as poisons to the catalysts even in low concentrations. Industrially, high-purity hydrogen rich streams via steam reforming of natural gas are produced, and then further purified to achieve the desired quality. Not only is steam reforming environmentally taxing, it is also both energetically and cost demanding. Alternatively, membrane based separation processes possess high hydrogen selectivity – produce high-purity levels of hydrogen – along with low energy consumption and cost effectiveness.<sup>16-18</sup>

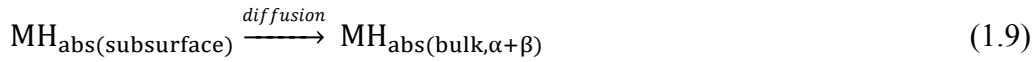
Separation membranes are classified according to composition: metallic (pure metals or alloys), inorganics (oxides, zeolites, glasses and ceramics), porous carbons, pure organic polymers and hybrids.<sup>17,18</sup> Metallic and dense ceramic membranes are currently the most suitable materials to obtain high purity hydrogen. Historically, metallic membranes separations

have been extensively studied and performed using Pd and Pd alloys. The mechanism of hydrogen permeation through palladium proceeds over several steps: (a) diffusion of molecular hydrogen to the metal membrane surface, (b) reversible dissociative adsorption on the metal surface, (c) dissolution of atomic hydrogen into the bulk metal, (d) diffusion of atomic hydrogen through the bulk metal, (e) accumulation of hydrogen atoms on the metal surface, (f) desorption of molecular hydrogen from the surface, and (g) diffusion of molecular hydrogen away from the surface.<sup>18</sup>

A major drawback associated with the use of pure Pd membranes is hydrogen embrittlement. This phenomenon is related to the cracking of the membrane upon large expansions of the lattice constant.<sup>19</sup> Palladium absorbs hydrogen in two distinct phases; at low concentrations of hydrogen the  $\alpha$ -phase appears (solid solution), whereas at high concentrations of hydrogen the  $\beta$ -phase (metal hydride) is found.<sup>19-21</sup> At low concentrations the lattice constant is very similar to pure Pd; as the concentration of hydrogen increases, so does the lattice constant. The transition between phases is referred to as the  $\alpha$ - $\beta$  phase transition, which is associated with the dilation of the face-centered cubic lattice constant. Changing the size of the Pd particles (nanomaterial's) or alloying them with other metals has shown to have an effect on the phase transition, limiting the amount of cracking caused by the phase transition expansion.<sup>18-21</sup>

An important factor in both hydrogen purification and hydrogen storage is the catalytic ability of the hydrogen dissociation catalysts. Palladium and its alloys present several benefits as dissociation catalysts, a key factor being their potential for applications at ambient conditions.<sup>22</sup> The palladium–hydride system has been extensively studied, revealing that hydrogen atoms are usually considered to enter the metal either by a two-step (indirect) or

direct process for hydrogen absorption. Indirect hydrogen absorption first adsorbs hydrogen on the electrode surface, followed by absorption in the subsurface layer and further diffusion into the bulk of the metal. In comparison, direct hydrogen absorption involves the reduction of protons to form the subsurface absorbed hydrogen. The following processes can describe the adsorption/absorption process of the indirect mechanism<sup>20,23,24</sup>:



As well, Pd–H interactions of the adsorbed hydrogen can form gaseous hydrogen through electrochemical desorption (1.13) and chemical recombination (1.14):<sup>20, 23,24</sup>



As mentioned previously, storage of produced hydrogen is necessary for onboard vehicular storage and stationary power applications. For automotive applications, critical hydrogen storage properties of importance are (i) lightweight, (ii) economical and readily available, (iii) high volumetric and gravimetric density of hydrogen, (iv) fast kinetics, (v) easy activation, (vi) low temperature of dissociation or decomposition, (vii) appropriate thermodynamic properties, (viii) long-term cycling stability, and (ix) high degree of reversibility.<sup>16,20,25</sup> In the automotive industry, palladium has received a great deal of attention for its ability to reversibly store large volumetric amounts of hydrogen and its high stability. However, due to its expense and low gravimetric hydrogen density, palladium should not be

considered as the sole hydrogen storage material.

Most metals, excluding Pd, require input energy to overcome an activation barrier in order to dissociate molecular hydrogen. This can be achieved in the form of high hydrogen pressures or elevated temperatures. Temperature and equilibrium pressure comparisons required for metal hydride hydrogen storage properties of intermetallic compounds can be found in Table 1.2. From the table it is evident that Pd is the only metal to form a hydride at ambient conditions with the advantage of exhibiting superior dissociative properties.<sup>22</sup> In an effort to reduce the cost, alternative methods for use and treatment of palladium have been employed. Most prominent is the incorporation of transition metals to form alloys.<sup>24,26-28</sup> Ideally, alloyed metals are of significantly lesser cost and act to enhance rather than hinder adsorption properties.<sup>29</sup> Pd alloying acts to alter the crystal lattice structure, as well as electronic, and elastic properties, resulting in different thermodynamic and kinetic characteristics.<sup>22</sup> By alloying Pd with less expensive metals, the overall amount of Pd used may be reduced, marginally cutting costs.

**Table 1.2** Hydrogen storage properties of intermetallic compounds.<sup>22</sup>

Type	Metal	Hydride	Structure	wt. % H	$P_{eg}$ , T
Elemental	Pd	$PdH_{0.6}$	Fm3m	0.56	0.020 bar, 298 K
$AB_5$	$LaNi_5$	$LaNi_5H_6$	P6/mmm	1.37	2 bar, 298 K
$AB_2$	$ZrV_2$	$ZrV_2H_{5.5}$	Fd3m	3.01	$10^{-8}$ bar, 323 K
AB	FeTi	$FeTiH_2$	Pm3m	1.89	5 bar, 303 K
$A_2B$	$Mg_2Ni$	$Mg_2NiH_4$	P6222	3.59	1 bar, 555K
Body-centred cubic	$TiV_2$	$TiV_2H_4$	b.c.c.	2.6	10 bar, 313 K

From a hydrogen storage point of view, Pd-based alloys suffer from low gravimetric capacities.<sup>30</sup> Further reduction of the mass of bulk Pd will enable the use of Pd and Pd-based alloys for practical applications. Hydrogen storage properties of metal hydrides change with

particle size.<sup>30-32</sup> Forming materials on the nanoscale level strongly influences the thermodynamics and kinetics of hydrogen adsorption and dissociation by increasing the diffusion rate and decreasing the required diffusion length. The novel properties of nanostructured materials, such as surface adsorption, inter- and intragrain boundaries, and bulk adsorption, show potential promise in hydrogen storage.<sup>30-32</sup> With regards to the Pd-H system, hydrogen solubility and equilibrium pressure for formation of Pd-H decreases as particle size decreases. In general, metal nanoparticles offer practical hydrogen storage and excellent catalytic abilities due to their large surface areas and particular electronic states resulting from the size effect.<sup>31,32</sup> Materials at the nanoscale level offer the possibility of controlled material parameters which can lead to a lightweight hydrogen storage system design with enhanced characteristics.<sup>25</sup>

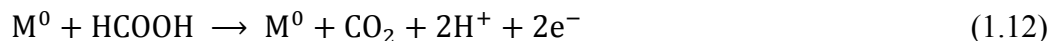
Taking the reduction of cost one step further, the use of inexpensive support materials for metal catalysts offers advantages such as low mass density and high storage capacity.<sup>33,34</sup> Carbon materials have garnered ample attention as hydrogen storage materials due to their considerable hydrogen adsorption/desorption kinetics and high catalytic stability. Solely, without modification, high surface area carbon materials cannot store (physisorb) sufficient quantities of H<sub>2</sub> at ambient temperatures for enabling practical applications.<sup>35-38</sup> An effective mode for the enhancement of hydrogen storage is hydrogen dissociation followed by a spillover effect through metallic doping.<sup>16,35,36,39-43</sup> The elementary mechanistic details of hydrogen spillover remain unclear in most cases, although it is apparent that two fundamental processes occur: hydrogen dissociation at the metal surface and its subsequent transfer to the support.<sup>42-51</sup> As discussed earlier, Pd offers superior dissociative properties, which enables it to serve as a promising hydrogen dissociation catalyst.<sup>16,22,35</sup> As well, an advantageous property offered

through the use of Pd as a hydrogen dissociation catalysts is its ability to form a hydride (PdH<sub>x</sub>). Using Pd and Pd alloys as the catalyst would lead to enhanced hydrogen capacity of the overall material as compared to that of a non-absorbing metal.

#### 1.4 Palladium in Fuel Cell Catalysis

The development of electrocatalysts is essential in driving progress towards the development of fuel cells with high catalytic activity. Platinum (Pt) has been the most commonly employed electrocatalyst in low temperature fuel cells. To date, Pt has been unable to satisfy commercial needs due to its high cost and vulnerability to CO.<sup>49-53</sup> As an alternative, Pd-based catalysts have been studied intensively for their desirable activity towards the catalysis of small organic molecules, such as alcohol, methanol and formic acid.<sup>15,52-58</sup> More specifically, Pd has been shown to be far superior than Pt concerning formic acid oxidation.

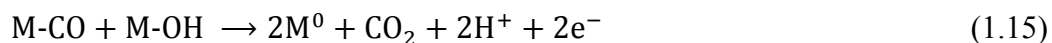
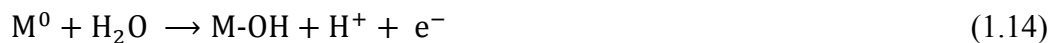
As previously mentioned, the most commonly accepted mechanism, originally proposed by Capon and Parsons, for formic acid oxidation on noble metal is the “dual pathway mechanism”.<sup>14,15,62-64</sup> In the first reaction pathway, the direct pathway, adsorption of formic acid leads to the formation of an adsorbed intermediate, which then further oxidizes to CO<sub>2</sub>. The direct pathway can be represented by the following reaction.<sup>13, 65-71</sup>:



(M<sup>0</sup> = Pt, Pd and other)

The second reaction pathway, indirect pathway, forms adsorbed carbon monoxide as a stable reaction intermediate via the dehydration of formic acid<sup>13, 65-71</sup>:





For enhanced overall cell efficiency in DFAFCs, dehydrogenation (direct pathway) is the desired reaction pathway.<sup>13, 15, 65-72</sup> The superior performance of Pd, as opposed to Pt, is a result of palladium's ability to promote the direct reaction pathway. However, despite the promotion of the direct pathway, a slow and continuous decay after discharging for several hours is commonly observed.<sup>14, 52, 65, 71, 72</sup> This decay is believed to be caused by the accumulation of CO-like species on the Pd surface, such as adsorbed  $-OH$ ,  $(COOH)_{ad}$  or other adsorbed anions.<sup>65, 71, 72</sup> Methods employed to limit the effects of poisoning species include metal alloying; the incorporation of a second metal to weaken CO adsorption, and catalyst regeneration. Investigations aimed at a further understanding of the mechanism of formic acid oxidation can lead to the development of improved electrocatalysts for DFAFC. The transition from Pt-based to Pd-based catalysts will likely result in the development of more cost effective materials with enhanced activity toward the commercialization of fuel cells.

## 1.5 Stimulus and Scope of This Thesis

An overview of the fundamentals of the hydrogen economy, including fuel cells and palladium-based electrocatalyst applications was provided in this chapter. It becomes apparent that limitations that are imposed by the cost of modern technology inhibit the transition towards a hydrogen economy. The basic properties of PEMFCs are discussed with a focus on hydrogen storage/production and anode development for formic acid oxidation. The scope of this thesis will encompass investigations into the properties of Pd-based nanomaterials in relation to their

applications in fuel cell technologies. A core focus will be the design of palladium-based nanostructured catalysts with high electrocatalytic activity towards hydrogen storage and/or formic acid oxidation. Promising ongoing research into the development and integration of low cost in materials required for a given application is a prominently addressed goal. Modification methods of both catalysts and supports are investigated in order to develop efficient Pd-based nanostructured catalysts.

The following chapter, Experimental Methods, will give information pertaining to the fabrication of nanostructured materials, as well as the methods used to analyze their structure and physical properties. Chapter 3 presents the results of the electrosorption of hydrogen into activated carbon supported Pd, PdAg, PdCd, and PdAgCd nanostructures. Chapter 4 details the electrocatalytic properties of pre-treated Pd-modified TiO<sub>2</sub> NTs towards hydrogen electrosorption and formic acid oxidation. The electrooxidation of formic acid on TiO<sub>2</sub> NT supported PdPb nanoparticles is examined in Chapter 5. The final chapter, Chapter 6, will provide a synopsis of results and a prospective outlook regarding future work.

## References

- (1) Brinker, C. J.; Ginger, D. *Science Policy Reports, Chapter 6: Nanotechnology for Sustainability - Energy Conversion, Storage, and Conservation* Springer, Netherlands, **2011**, *1*, 261.
- (2) Matthews, H. D.; Gillett, N. P.; Stott, P. A.; Zickfeld, K. *Nature*, **2009**, *459*, 829.
- (3) Ogden, J. M. *Annu. Rev. Energy Environ.* **1999**, *24*, 227.
- (4) Chen A.; Holt-Hindle, P. *Chem. Rev.* **2010**, *110*, 3767.
- (5) Sherif, S. A.; Barbir, F.; Veziroglu, T. N. *The Electricity Journal* **2005**, *18*, 62.
- (6) Crabtree, G. W.; Dresselhaus, M. S.; Buchanan, M. V. *Physics Today* **2004**, *57*, 39.
- (7) Potter, A.; Newell, M. *Home Power* **1993**, *32*, 42.

- (8) Shah, R.K. *Recent Trends in Fuel Cell Science and Technology, Chapter 1: Introduction to Fuel Cells*, Anamaya Publishers, New Delhi, **2007**.
- (9) Kordesch, K. V.; Simander, G. R. *Chem Rev.* **1995**, *95*, 191.
- (10) Sadiq Al-Baghdadi, M. A. R., *Fuel Cell Research Trends, Chapter 7: PEM Fuel Cell Modeling* Nova Science Publisher, New York, **2007**.
- (11) Dincer, I. *JJMIE* **2008**, *2*, 1.
- (12) Pant, K. K. Gupta, R. B. *Hydrogen Fuel: Production, Transport and Storage* CRC Press, Boca Raton, FL, **2009**.
- (13) Rice, C.; Ha, S.; Masel, R. I.; Waszczuk, P.; Wieckowski, A.; Barnard, T. *J Power Source.* **2002**, *111*, 83.
- (14) Yu, X.; Pickup, P. G. *J Power Source.* **2008**, *182*, 124.
- (15) Rice, C.; Ha, S.; Masel, R. I.; Wieckowski, A.; Barnard, T. *J Power Source.* **2003**, *115*, 229.
- (16) Adams, B.; Chen, A. *Mater. Today* **2011**, *14*, 282.
- (17) Ockwig, N. W.; Nenoff, T. M. *Chem. Rev.* **2007**, *107*, 4078
- (18) Gallucci, F.; Fernandez, E.; Corengia, P.; van Sint Annaland, M. *Chem. Eng. Sci.* **2013**, *92*, 40.
- (19) Łukaszewski, M.; Hubkowska, K.; Czerwiński, A. *J Electroanal. Chem.* **2011**, *651*, 131.
- (20) Gabrielli, C.; Grand, P. P.; Lasia, A.; Perrot, H. *J. Electrochem Soc.* **2004**, *151*, A1937.
- (21) Gabrielli, C.; Grand, P. P.; Lasia, A.; Perrot, H. *J. Electrochem Soc.* **2004**, *151*, A1925.
- (22) Schlapbach, L.; Züttel, A. *Nature* **2001**, *414*, 353.
- (23) Lasia, A. *J. Electroanal. Chem.* **2006**, *593*, 159.
- (24) Adams, B. D.; Ostrom, C. K.; Chen, A. *Langmuir* **2009**, *26*, 7632.
- (25) Niemann, M. U.; Srinivasan, S. S.; Phani, A. R.; Kumar, A.; Goswami, D. Y.; Stefanakos, E. K. *J. Nanomater.* **2008**, *950967*, 1.
- (26) Adams, B. D.; Wu, G.; Nigro, S.; Chen, A. *J. Am. Chem. Soc.* **2009**, *131*, 6930.
- (27) Adams, B. D.; Ostrom, C. K.; Chen, S.; Chen, A. *J. Phys. Chem. C.* **2010**, *114*, 19875

- (28) Chen, S.; Adams, B. D.; Chen, A. *Electrochim. Acta* **2010**, *56*, 61.
- (29) Flanagan, T. B.; Oates, W. A. *Annu. Rev. Mater. Sci.* **1991**, *21*, 269.
- (30) Broom, D.P. *Green Energy and Technology, Chapter 2: Hydrogen Storage Materials* Springer-Verlag, London, **2011**, *1*, 19.
- (31) Yamauchi, K.; Kitagawa, H.; Kobayashi, H. *ChemPhysChem* **2009**, *10*, 2566.
- (32) Liang, H.-P.; Lawrence, N. S.; Jones, T. G. J.; Banks, C. E.; Ducati, C. *J. Am. Chem. Soc.* **2007**, *129*, 6068.
- (33) Zieliński, M.; Wojcieszak, R.; Monteverdi, S.; Mercy, M.; Bettahar, M. M. *Int. J. Hydrogen Energy* **2007**, *32*, 1024.
- (34) Wang, L.; Yang, R. T. *Catal. Rev. Sci. & Eng.* **2010**, *52*, 411.
- (35) Ströbel, R.; Garche, J.; Moseley, P. T.; Jörissen, L.; Wolf, G. *J. Power Sources* **2006**, *159*, 781.
- (36) Chen, C.-Y.; Chang, J.-K.; Tsai, W.-T. *Int. J. Hydrogen Energy* **2012**, *37*, 3305.
- (37) Im, J. S.; Park, S.-J.; Kim, T.; Lee, Y.-S. *Int. J. Hydrogen Energy* **2009**, *34*, 3382.
- (38) Ding, F.; Lin, Y.; Krasnov, P. O.; Yakobson, B. I. *J. Chem. Phys.* **2007**, *127*, 164703.
- (39) Jiménez, V.; Ramírez-Lucas, A.; Sánchez, P.; Valverde, J. L.; Romero, A. *Int. J. Hydrogen Energy* **2012**, *37*, 4144.
- (40) Yang, Y. X.; Singh, R. K.; Webley, P. A. *Adsorption* **2008**, *14*, 256.
- (41) Zhao, W.; Fierro, V.; Zoltea, C.; Izquierdo, M. T.; Chevalier-César, C.; Latroche, M.; Celzard, A. *Int. J. Hydrogen Energy* **2012**, *37*, 5072
- (42) Lueking, A.; Yang, R. T. *J. Catal.* **2002**, *206*, 165.
- (43) Lueking, A. D.; Yang, R. T. *Appl. Catal., A* **2004**, *265*, 259.
- (44) Parambath, V. B.; Nagar, R.; Sethupathi, K.; Ramaprabhu, S. *J. Phys. Chem. C* **2011**, *115*, 15679.
- (45) Lykhach, Y.; Staudt, T.; Vorokhta, M.; Skála, T.; Johánek, V.; Prince, K. C.; Matolín, V.; Libuda, J. *J. Catal.* **2012**, *285*, 6.

- (46) Łukaszewski, M.; Żurowski, A.; Grdeń, M.; Czerwiński, A. *Electrochem. Commun.* **2007**, *9*, 671.
- (47) Łukaszewski, M.; Kędra, T.; Czerwiński, A. *Electrochim. Acta* **2010**, *55*, 1150.
- (48) Łukaszewski, M.; Klimek, K.; Żurowski, A.; Kędra, T.; Czerwiński, A. *Solid State Ionics* **2011**, *190*, 18.
- (49) Hao, S.; Shol, D. S. *J. Phys. Chem. C* **2013**, *117*, 1217.
- (50) Chen, C.-H.; Chung, T.-Y.; Shen, C.-C.; Yu, M.-S.; Tsao, C.-S.; Shi, G.-N.; et al. *Int. J. Hydrogen Energy* **2013**, *38*, 3681.
- (51) Singh, A. K.; Ribas, M. A.; Yakobson, B. I. *ACS Nano* **2009**, *3*, 1657.
- (52) Baik, S. M.; Han, J.; Kim, J.; Kwan, Y. *Int. J. Hydrogen Energy* **2011**, *36*, 14719.
- (53) Arenz, M.; Stamenkovic, V.; Schmidt, T. J.; Wandelt, K.; Ross, P. N.; Markovic, N. M. *Phys. Chem. Chem. Phys.*, **2003**, *5*, 4242.
- (54) Guo, P.; Wei, Z.; Ye, W.; Qin, W.; Wang, Q.; Guo, X.; Lu, C.; Zhao, X. S. *Colloids Surf., A* **2012**, *395*, 75.
- (55) Ha, S.; Larsen, R.; Masel, R. I. *J. Power Sources* **2005**, *144*, 28.
- (56) Larsen, R.; Ha, S.; Zakzeski, J.; Masel, R. I. *J. Power Sources* **2006**, *157*, 78.
- (57) Cui, G. F.; Song, S. Q.; Shen, P.K.; Kowal, A.; Bianchini, C. *J. Phys. Chem. C* **2009**, *113*, 15639.
- (58) Lee, Y.-W.; Oh, J.-K.; Kim, H.-S.; Lee, J.-k.; Han, S.-B.; Choi, W.; Park, K.-W. *J. Power Sources* **2010**, *195*, 5896.
- (59) Shao, M. H.; Liu, P.; Zhang, J. L.; Adzic, R. *J. Phys. Chem. B* **2007**, *111*, 6772.
- (60) Shao, M. H.; Sasaki, K.; Adzic, R. R. *J. Am. Chem. Soc.* **2005**, *128*, 3526.
- (61) Zhu, Y.; Khan, Z.; Masel, R. I. *J. Power Source.* **2005**, *139*, 15.
- (62) Capon, A.; Parsons, R. *J. Electroanal. Chem.* **1973**, *44*, 1.
- (63) Capon, A.; Parsons, R. *J. Electroanal. Chem.* **1973**, *44*, 239.
- (64) Capon, A.; Parsons, R. *J. Electroanal. Chem.* **1973**, *45*, 205.
- (65) Zhou, Y.; Liu, J.; Ye, J.; Zou, Z.; Ye, J.; Gu, J.; Yu, T.; Yang, A. *Electrochim. Acta* **2010**,

55, 5024.

(66) Wang, X.; Hu, J.-M.; Hsing, I.-M. *J. Electroanal. Chem.* **2004**, *562*, 73.

(67) Lu, Y.; Chen, W. *J. Phys. Chem. C* **2010**, *114*, 21190.

(68) Jiang, J.; Kucernak, A. *J. Electroanal. Chem.* **2002**, *520*, 64.

(69) Zhang, L. J.; Wang, Z. Y.; Xia, D. G. *J. Alloys Compd.* **2006**, *426*, 268.

(70) Winjobi, O.; Zhang, Z.; Liang, C.; Li, W. *Electrochim. Acta* **2010**, *55*, 4217.

(71) Seland, F.; Tunold, R.; Harrington, D. A. *Electrochim. Acta* **2008**, *53*, 6851.

(72) Niquirilo, R. V.; Teixeira-Neto, E.; Buzzo, G. S.; Suffredini, H. B. *Int. J. Electrochem. Sci.* **2010**, *5*, 344.

## Chapter 2. Experimental Methods

### 2.1 Introduction

The motivations for studying Pd-based nanomaterials for anodes that may be employed in hydrogen storage/production and formic acid were presented in the previous chapter, as well as a discussion of the underlying challenges for commercial applications. In this chapter, the main experimental methodologies and techniques that are used in this M.Sc. research will be introduced. Details of the experimental procedures and equipment pertaining to each specific study are presented in Chapters 3-5.

### 2.2 Chemicals and Materials

Sulfuric acid (99.999%); hydrochloric acid (37.5%); sodium borohydride ( $\geq 98\%$ );  $\text{AgNO}_3$  ( $\geq 99\%$ );  $\text{Pd}(\text{NO}_3)_2$ ;  $\text{Pb}(\text{NO}_3)_2$  ( $\geq 99\%$ ); formic acid ( $> 96\%$ ); dimethyl sulfoxide (DMSO) (99.99%); hydrofluoric acid (50%); 2-propanol ( $\geq 99.5\%$ ), and Nafion<sup>®</sup> perfluorinated ion-exchange resin (10 wt.% dispersion in water), were used as received from Sigma-Aldrich.

Titanium wire (2 mm diameter); Pt wire (99.9%, 0.5 mm diameter);  $\text{PdCl}_2$  (99.9%); and  $\text{Cd}(\text{NO}_3)_2$  (99.9%), were used as received from Alfa-Aesar.

Gases used throughout this thesis research were: argon (PRAXAIR, UHP, 99.999%), and nitrogen (PRAXAIR, UHP, 99.999%).

Activated carbon and  $\text{TiO}_2$  NTs were used as support materials for nanoparticles. Powdered activated carbon, Norit PAC 200 (M-1620), was obtained from Norit Americas Inc.  $\text{TiO}_2$  NTs were fabricated from titanium plates (99.2%), purchased from Alfa Aesar and cut into 1.25 x 0.8 cm rectangles with a thickness of 0.5 cm.

Pure water (18 M $\Omega$ cm) obtained from a NANOpure<sup>®</sup> Diamond<sup>™</sup> UV ultrapure water purification system was used for cleaning purposes and the preparation of all solutions and electrolytes.

## **2.3 Fabrication of Nanomaterials**

### **2.3.1 Carbon-Supported Nanomaterials**

Carbon-supported nanomaterials were employed for hydrogen electrosorption and nitrogen gas adsorption studies (Chapter 3). All of the carbon-supported samples were prepared using a facile room temperature impregnation method.<sup>1</sup> The metal precursors, water (5 mL) and 0.5 g PAC200 were combined in a beaker such that the coating load was 5 wt.% metal in all cases. The mixture was then sonicated for 20 minutes. The pH of the mixture was adjusted to between 9.5 and 10 using 0.5 M NaOH and was allowed to stir for five minutes, providing a better overall dispersion of the metal precursors on the carbon support. The reducing agent (0.125 M NaBH<sub>4</sub>), in 10 times molar excess of the metal content, was added dropwise under constant stirring. The reactive reduction process proceeded for one hour prior to the catalysts being centrifuged and rinsed with pure water. Rinsing of the nanoparticles continued until all of the NaBH<sub>4</sub> was removed and the pH remained constant. The catalysts were then dried overnight in an oven at 60 °C.

Verification of the reduction of the metal catalysts and the final composition of the carbon-supported nanomaterials was obtained through use of inductively coupled plasma atomic emission spectroscopy (ICP-AES). This was accomplished by analyzing the solution subsequent to reduction with sodium borohydride to ensure that no metal remained.

The working electrodes were prepared by coating a glassy carbon electrode (0.1964 cm<sup>2</sup> surface area) with the activated carbon modified with Pd, PdCd, PdAg and PdAgCd

nanoparticles. The electrode coating solutions consisted of a 1 mL : 1 mg ratio of 40% isopropanol: carbon-supported Pd-based nanoparticles. All solutions were sonicated for 20 minutes, or until no nanoparticles remained at the bottom of the container. This was followed by the addition of 15  $\mu$ L Nafion with further sonication for an additional hour. Prior to coating the electrode, the glassy carbon surface was polished until visibly lustrous, and then weighed. Eight coats of 10  $\mu$ L aliquots of coating solution were applied and allowed to air dry. The GCE were then weighed once again, using a high-precision (0.01mg) balance (Mettler-Toledo), in order to determine the coating load.

### **2.3.2 TiO<sub>2</sub> NT-Supported Nanomaterials**

TiO<sub>2</sub> nanotubes were fabricated in a two electrode electrochemical cell.<sup>2</sup> Using Ti substrate plates (1.25 cm x 0.80 cm x 0.5 mm) as the working electrode, they were first degreased in an ultrasonic bath of acetone for 10 minutes followed by 10 minutes in pure water. The substrates were then etched in 18% HCl at 85 °C for 30 minutes, and then thoroughly rinsed with pure water. The counter electrode consisted of a Pt wire coil (2 cm<sup>2</sup>), which was cleaned prior to each experiment via flame annealing. Anodization proceeded in a solution that contained dimethyl sulfoxide (DMSO) with 2% (wt.) HF and 2% (wt.) H<sub>2</sub>O at 40 V for eight hours. Following the electrochemical treatment, the sample was thoroughly rinsed with pure water and then baked at 450 °C for three hours to form the anatase structured TiO<sub>2</sub> NTs.

TiO<sub>2</sub> NT supported nanoparticles were used for hydrogen sorption (Chapter 4) and formic acid oxidation (Chapter 4 and 5). Ultraviolet light irradiation<sup>3</sup> and electrochemical pretreatment methods were used to enhance the activity of the TiO<sub>2</sub> NT supports. For the UV pretreatment, a TiO<sub>2</sub> NT sample was placed in a quartz tube containing 50% methanol-H<sub>2</sub>O (v/v) and then bubbled with Ar for 20 minutes. The quartz tube was then capped and irradiated

under intense UV light for one hour. Electrochemically pretreated TiO<sub>2</sub> NT samples were placed in a three-electrode electrochemical cell containing 0.5 M H<sub>2</sub>SO<sub>4</sub> as the supporting electrolyte, after which a constant current of -5 mA was applied for ten minutes.

All TiO<sub>2</sub> NT supported samples were prepared using a facile room temperature impregnation method, with NaBH<sub>4</sub> as the reducing agent. The appropriate metal precursors, water, and 0.5 M NaOH (enough to adjust the pH between 9.5 and 10) were combined and sonicated for 20 minutes. The Pd-containing coating solution (20 μL) was then placed directly onto the surface of the pre-weighed TiO<sub>2</sub> NT electrode. Immediately following, 0.125 M NaBH<sub>4</sub> was added dropwise to the surface solution and allowed to sit for five minutes. Once complete, the electrodes were thoroughly rinsed with pure water and allowed to dry. This procedure was repeated up to four times to obtain the desired coating loads.

## 2.4 Surface Analysis

Synthesized PAC200 nanomaterials were characterized by transmission electron microscopy (TEM), X-ray photoelectron spectroscopy (XPS), energy dispersive X-ray spectroscopy (EDX), X-ray diffraction (XRD), and gas adsorption/desorption analysis. The TEM instrument used in this study was a JOEL 2010, whereas XPS was performed using a Thermo Scientific K-Alpha XPS spectrometer. The samples were run at a takeoff angle (relative to the surface) of 90°. A monochromatic Al Kα X-ray source was employed with a spot size of 400 μm. The position of the energy scale was adjusted to place the main C1s feature (C-C) at 284.6 eV. All data acquisition was enabled by XPSpeak software. Elemental mapping of the samples was recorded by the EDX technique using a Hitachi Su-70 Schottky Field Emission SEM with the application of 15 kV. The XRD patterns were recorded using a Philips PW 1050-3710 Diffractometer with a Cu Kα ( $\lambda = 1.5405 \text{ \AA}$ ) radiation source. The N<sub>2</sub>

gas adsorption and desorption studies were conducted using a Quantachrome Nova 2200 Surface Area and Pore Size Analyzer (See Section 2.6). Inductively coupled plasma atomic emission spectroscopy (ICP-AES) was employed to determine the concentrations of Pd<sup>2+</sup>, Ag<sup>+</sup>, and Cd<sup>2+</sup> in the precursor solutions, prior to and following the NaBH<sub>4</sub> reduction.

The surface morphology of the fabricated TiO<sub>2</sub> NT-supported samples was characterized by scanning electron microscopy (SEM) using a Hitachi Su-70 Schottky Field Emission SEM, along with elemental mapping recorded by the EDX technique with an application of 15 kV.

## **2.5 Electrochemical Experiments**

All electrochemical experiments were carried out using a three-electrode cell system and a VoltaLab PGZ402 potentiostat. The reference electrode was silver-silver chloride (Ag/AgCl) 1 M KCl electrode. All electrode potentials are reported herein are with respect to the Ag/AgCl electrode. The counter electrode consisted of a Pt wire coil (10 cm<sup>2</sup>), which was cleaned prior to each experiment via flame annealing and quenching with the NANOpure water. The prepared nanoparticle materials were used as the working electrode in all cases. Prior to the electrochemical experiments, ultrapure argon gas was bubbled through the electrolyte solution (H<sub>2</sub>SO<sub>4</sub> or H<sub>2</sub>SO<sub>4</sub> + HCOOH) for approximately 15 minutes to remove any dissolved oxygen. Argon flowed continuously above the solution during the electrochemical measurements, which were conducted at ambient temperature, 20 ± 2 °C. Data acquisition and analysis were performed using VoltMaster 4 software.

## **2.6 Gas Sorption Studies**

N<sub>2</sub> gas adsorption/desorption studies were performed using a Quantachrome Nova 2200 Surface Area and Pore Size Analyzer. The samples were initially degassed for a minimum of

three hours under vacuum. Adsorption/desorption of N<sub>2</sub> was performed at liquid nitrogen temperature (77 K). The Brunauer-Emmett-Teller (BET) surface area was calculated from N<sub>2</sub> adsorption with a multipoint method using five points within the relative pressure (P/P<sub>0</sub>) range of 0.10 to 0.30. The total pore volumes were calculated at a relative pressure of 0.99. The micropore volumes and modal micropore diameters were obtained using Dubinin–Astakhov (DA) method of analysis. The Barrett–Joyner–Halenda (BJH) method was used to determine the volume of mesopores and modal mesopore diameters using the desorption branch and ignoring points below a relative pressure of 0.35.

## 2.7. Summary

This chapter has presented the materials used in this M. Sc. thesis project. The experimental methods and equipment employed for synthesizing and characterizing Pd-based nanomaterials were discussed in detail. The following chapter will present a study of carbon supported Pd-based tri-metallic nanoparticles for the electrosorption of hydrogen.

## References

- (1) Adams, B.A.; Ostrom, C.K.; Chen, S.; Chen, A. *J. Phys. Chem. C*. **2010**, *114*, 19875.
- (2) Tian, M.; Malig, M.; Chen, S.; Chen, A. *Electrochem. Commun.* **2011**, *13*, 370.
- (3) Tian, M.; Thind, S. S.; Chen, S.; Matyasovsky, N.; Chen, A. *Electrochem. Commun.* **2011**, *13*, 1186.

## Chapter 3. Synthesis and Electrochemical Study of Pd-based Tri-metallic Nanoparticles for Enhanced Hydrogen Storage\*

### 3.1 Introduction

As prerequisites for enabling the reality of a hydrogen-based economy, the issues of hydrogen storage and production must be met. Unlike many other fuels, hydrogen is gaseous at ambient temperature and pressure, making confined storage impractical. Currently implemented hydrogen storage technologies, such as cryogenic liquefied hydrogen, pressurized hydrogen gas tanks, organic chemical hydrides, metal hydrides, and carbon materials,<sup>1-6</sup> fail to meet the standardized requirements.<sup>7</sup> Recently, carbon materials have received considerable attention due to their low density, high surface areas and low costs.<sup>8-11</sup> Unfortunately, carbon materials do not have the capacity for the storage of sufficient amount of hydrogen solely by physical adsorption at ambient temperature.<sup>12,13</sup>

Physisorption onto carbon materials is based on van der Waals interactions between gases and solids. This allows for the advantages of a lightweight and low cost material with reversible hydrogen capacities. Activated carbon materials attain high hydrogen storage capacity at high pressures or cryogenic temperatures by means of physisorption.<sup>14-16</sup> On the other hand, chemisorption in metal hydrides offers dissociation of H-H bonds at room temperature.<sup>17</sup> Physisorption, in contrast to the phenomenon of chemical adsorption, accumulates the undissociated hydrogen molecules on the surface of microporous activated carbon. In terms of hydrogen storage, an ideal composite material would integrate the binding energy properties of physisorption and chemisorption, and be readily reversible.<sup>9,18-20</sup>

---

\* This chapter has been accepted by *J. Phys. Chem. C*, September 2013, *in press*.

The enhancement of hydrogen storage on adsorbents such as activated carbon may be achieved by exploiting hydrogen spillover.<sup>21-26</sup> The dispersal of metal catalysts onto the surface allows for the dissociation of dihydrogen molecules, leading to the subsequent spillover of hydrogen atoms to carbon, thus in turn, increasing the amount of hydrogen sorbed.<sup>27,28</sup> As a metal catalyst, palladium exhibits a good compromise between suitable dissociation abilities and low sticking strengths for the use in hydrogen spillover. By alloying Pd with other metals such as Ag and Cd, the phenomena may be further enhanced.<sup>29-31</sup> In the present study, we have investigated the electrochemical hydrogen adsorption capabilities of activated carbon supported nanoparticles at room temperature. Through the dispersal of catalysts onto the surface of the activated carbon (Norit PAC200 (M-1620)), the effect of the tri-metallic Pd-Ag-Cd hydrogen dissociation catalysts were examined for the first time. Six different catalyst compositions (Pd, PdAg<sub>5</sub>Cd<sub>15</sub>, PdAg<sub>10</sub>Cd<sub>10</sub>, PdAg<sub>15</sub>Cd<sub>5</sub>, PdAg<sub>20</sub> and PdCd<sub>20</sub>, where the total composition of each catalyst was 100 percent) were selected and prepared for systematical investigation. The objectives of this study were two-fold: (i) to explore the possible synergistic effect of Pd, Ag and Cd on hydrogen storage and (ii) to determine the ideal catalyst composition that may facilitate increased hydrogen sorption. Our study has shown that the tri-metallic alloy, PdAg<sub>10</sub>Cd<sub>10</sub>, significantly enhances the hydrogen sorption capabilities of Pd-based dissociation catalysts, in comparison to Pd-Ag and Pd-Cd nanomaterials.

### **3.2 Experimental Section**

Commercially available activated carbon, Norit PAC200 (M-1620), from Norit Americas Inc. was utilized in this study. The Pd/PAC200, PdAg/PAC200, PdCd/PAC200 and PdAgCd/PAC200 samples were prepared using a facile room temperature impregnation method described in Chapter 2. Sodium borohydride was used as the reducing agent and the metal

precursors were as follows: PdCl<sub>2</sub>, Pd(NO<sub>3</sub>)<sub>2</sub>·2H<sub>2</sub>O; AgNO<sub>3</sub>; and Cd(NO<sub>3</sub>)<sub>2</sub>·4H<sub>2</sub>O. Varying amounts of the precursors were added to obtain the desired ratio of Pd to Cd and/or Ag.

Synthesized PAC200 nanoparticles were characterized by TEM, XPS, EDX and gas adsorption/desorption analysis. The TEM instrument used in this study was a JOEL 2010, whereas XPS was performed using a Thermo Scientific K-Alpha XPS spectrometer. Elemental mapping of the samples was recorded by the EDX technique using a Hitachi Su-70 Schottky Field Emission SEM. The N<sub>2</sub> gas adsorption and desorption studies were conducted using a Quantachrome Nova 2200 Surface Area and Pore Size Analyzer as described in Chapter 2. ICP-AES was employed to determine the concentrations of Pd<sup>2+</sup>, Ag<sup>+</sup>, and Cd<sup>2+</sup> in the precursor solutions before and after the NaBH<sub>4</sub> reduction.

All the electrochemical experiments, including CV and CA, were carried out using a three-electrode cell system and VoltaLab PGZ402 potentiostat as described in Chapter 2. The reference electrode was silver-silver chloride (Ag/AgCl) 1 M KCl electrode. All electrode potentials are mentioned from here on out with respect to the Ag/AgCl electrode. The working electrodes were prepared by coating a GCE (0.1964 cm<sup>2</sup>) with the activated carbon modified with Pd, PdCd, PdAg and PdAgCd nanoparticles as describe in Chapter 2. Eight coats of 10 μL aliquots of coating solution were applied and allowed to air dry. The GCE were then weighed once again to determine the coating load. Prior to the electrochemical experiments ultrapure argon gas (99.999%) was bubbled through a 0.5 M H<sub>2</sub>SO<sub>4</sub> electrolyte solution for approximately 15 minutes. The argon flowed continuously above the solution during the electrochemical measurements and all experiments were conducted at ambient temperature, 20 ± 2 °C.

Chronoamperometry (CA) was utilized to completely saturate the films with hydrogen. The potential was held at a range of -200 mV to -250 mV for one minute. Immediately following CA, a cyclic voltammogram (CV) spanning -200 to -250 mV was swept to 200 mV to desorb all of the adsorbed/absorbed hydrogen. Each CV was run at a scan rate of 5 mV/s for two cycles. All current densities ( $j$ ) and charges due to desorption of hydrogen ( $Q_H$ ) are reported in terms of per milligram of Pd-based catalyst unless stated otherwise. Data acquisition and analysis were performed using VoltMaster 4 software.

### **3.3 Surface Analysis of Catalyst Dispersed on Activated Carbon.**

The surface morphology of the prepared catalysts dispersed on the activated carbon was characterized using TEM. Typical TEM images of Pd/PAC200, PdAg<sub>5</sub>Cd<sub>15</sub>/PAC200, PdAg<sub>10</sub>Cd<sub>10</sub>/PAC200 and PdAg<sub>15</sub>Cd<sub>5</sub>/PAC200 are depicted in Figure 3.1. Of note is that the Pd nanoparticles (Figure 3.1a) were very well dispersed with a narrow size distribution ( $< \text{\AA} 3$  nm), and appeared to be embedded within the porous structure of PAC200. The tri-metallic nanoparticles of PdAg<sub>5</sub>Cd<sub>15</sub>/PAC200 (Figure 3.1b), PdAg<sub>10</sub>Cd<sub>10</sub>/PAC200 (Figure 3.1c), and PdAg<sub>15</sub>Cd<sub>5</sub>/PAC200 (Figure 3.1d) were dimensionally larger than the Pd nanoparticles (Figure 3.1a). In comparison to Pd/PAC200, the Pd-Ag-Cd nanoparticles ranged from 4 to 10 nm, and were situated on the surface of the carbon support rather than within the micropores, since most of them were too large to be embedded within the pores of the carbon. The Pd-Ag-Cd nanoparticles were not as well dispersed as the Pd nanoparticles and tended to concentrate at particular sites on the activated carbon.

The composition of the Pd-based catalysts dispersed on the carbon materials was analyzed directly and indirectly using EDX, XPS and ICP-AES. The initial concentrations and final concentrations of the metal precursors that remained within the solution following the

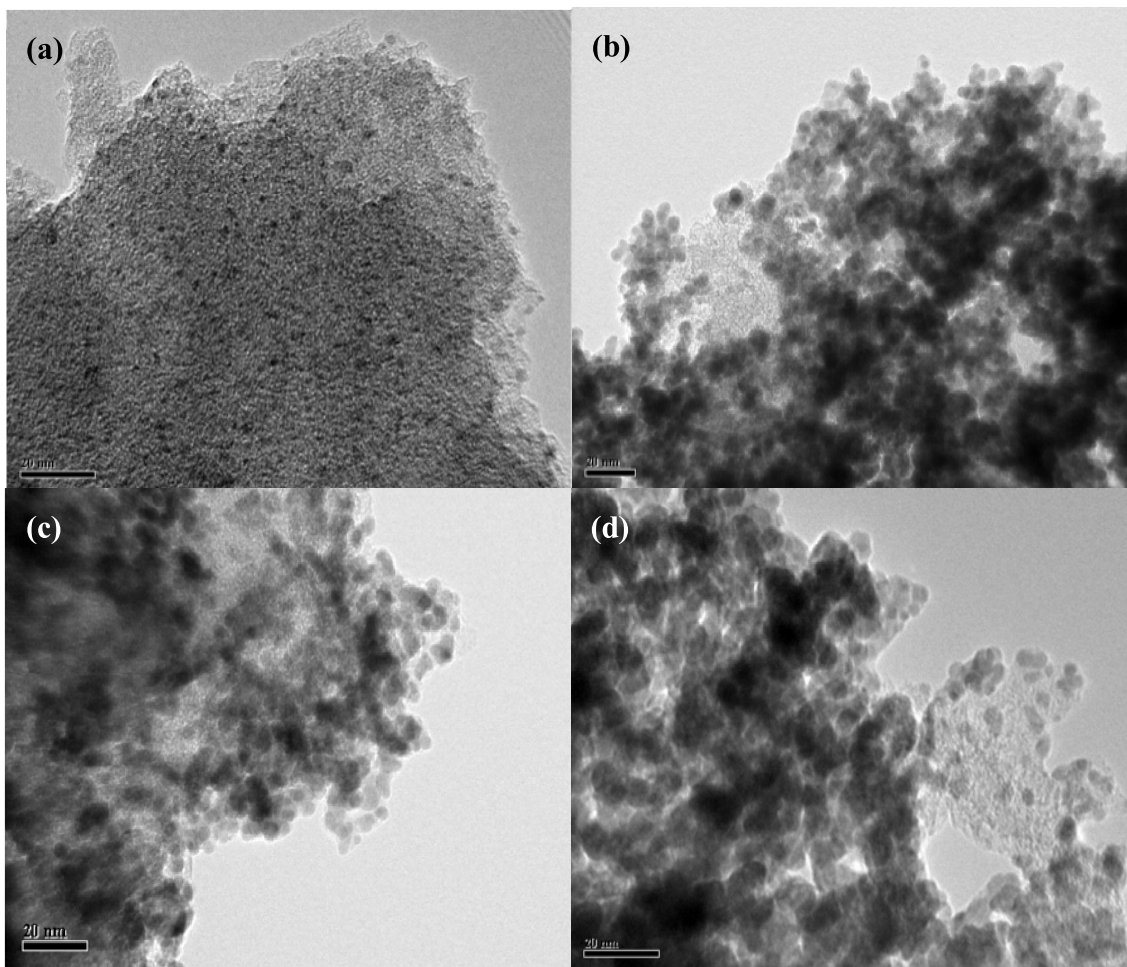


**Figure 3.1.** TEM images of Pd/PAC200 (a), PdAg<sub>5</sub>Cd<sub>15</sub>/PAC200 (b), PdAg<sub>10</sub>Cd<sub>10</sub>/PAC200 (c) and PdAg<sub>15</sub>Cd<sub>5</sub>/PAC200 (d).

preparation of the NaBH<sub>4</sub> reduction are listed in Table 3.1. It was found that less than 0.2 ppm of the metal ions remained within the solution in all cases, indicating that the metal precursors were completely reduced by sodium borohydride. By subtracting the final metal concentration from the initial value, it was found that the bulk composition of the dispersed catalysts was equivalent to the input concentrations, showing that the facile method used in this study can effectively control the compositions of the formed tri-metallic nanoparticles.

**Table 3.1.** ICP results of the concentrations of Pd<sup>2+</sup>, Ag<sup>+</sup>, and Cd<sup>2+</sup> remaining in solution following NaBH<sub>4</sub> reduction. Initial concentrations were calculated based on the amount of Pd(NO<sub>3</sub>)<sub>2</sub>, AgNO<sub>3</sub>, and Cd(NO<sub>3</sub>)<sub>2</sub> added.

sample	Pd(initial) /ppm	Pd(final) /ppm	Ag(initial) /ppm	Ag(final) /ppm	Cd(initial) /ppm	Cd(final) /ppm	molar ratio Pd:Ag:Cd
PdAg <sub>5</sub> Cd <sub>15</sub> /PAC200	532.10	0.01	33.71	0.00	105.66	0.01	80:5:15
PdAg <sub>10</sub> Cd <sub>10</sub> /PAC200	532.10	0.01	67.42	0.01	70.26	0.01	80:10:10
PdAg <sub>15</sub> Cd <sub>5</sub> /PAC200	532.10	0.13	101.40	0.16	35.13	0.01	80:15:5

The XPS survey scans of the four samples, along with PAC200 and PdAg<sub>20</sub>/PAC200, are shown in Figure 3.2a. For all samples, a carbon 1s peak at approximately 284.6 eV and an oxygen 1s peak at approximately 531.9 eV were observed. The intensity of the oxygen 1s peak is greater for the metal dispersed samples than the pure PAC200 sample, indicating the partial oxidation of the surface metal nanoparticles. Pd 3d and Pd 3p peaks were observed for all metal dispersed samples at ~335.6 and 560.1 eV, respectively. For the tri-metallic metal doped samples, Ag 3d and Cd 3d peaks can be seen at 367.7 eV and 404.9 eV, respectively. The Pd 3d, Ag 3d, and Cd 3d domains are shown for PdAg<sub>10</sub>Cd<sub>10</sub>/PAC200 (Figure 3.2b, 3.2c and 3.2d). The spectra display doublet peaks located at a low binding energy (3d<sub>3/2</sub>) and a high binding energy (3d<sub>5/2</sub>). The binding energies of the Pd 3d<sub>3/2</sub> and Pd 3d<sub>5/2</sub> peaks (Figure 3.2b) were measured at 340.9 and 335.6 eV, respectively. The Ag 3d and Cd 3d doublets were also

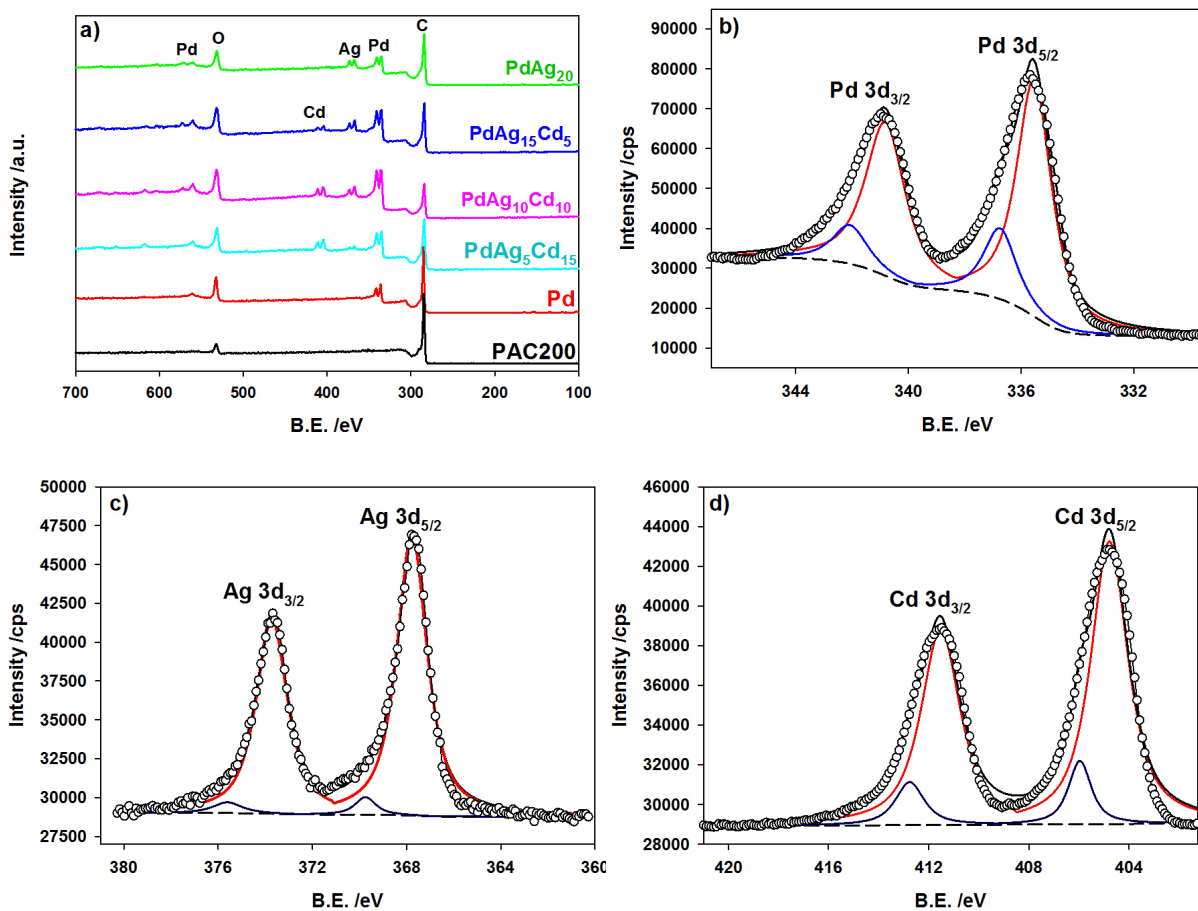


**Figure 3.2.** XPS comparative survey of palladium, silver and cadmium content samples (a); high resolution spectra of the Pd 3d region (b); Ag 3d region (c) and Cd 3d region (d) of PdAg<sub>10</sub>Cd<sub>10</sub> supported on PAC200. For the high resolution spectra, dots, dashed lines, and red, blue, and black lines represent the raw data, baseline, individual components (zero and high oxidation states), and total fit, respectively.

measured at  $\sim 373.7$  and  $367.7$ , and  $411.5$  and  $404.7$  eV, respectively. Using the area of the fitted curves for the Pd, Ag and Cd, in the metallic and higher oxidation states, the ratio of metal to metal oxide was calculated. It was found that 75%, 96%, and 88% of the Pd, Ag, and Cd, respectively, were in their metallic states. The surface composition of the metallic nanoparticles was calculated using the area under the high resolution 3d metal peaks. It was found that the surface composition varied slightly from the bulk composition, which is consistent with the ICP-AES analysis.

For a further examination of the PdAgCd/PAC200 sample composition, EDX analysis was performed to determine the metal ratio. For PdAg<sub>10</sub>Cd<sub>10</sub>/PAC200 sample, the metal atomic ratio for Pd, Ag, and Cd was calculated to be 78.96%, 11.56% and 9.48%, respectively, which is consistent with XPS analysis and the composition of the initial precursor solution and the ICP analysis listed in Table 3.1. Elemental mapping can provide a meaningful picture of the element distribution of a surface, as shown in Figure 3.3, which displays the PAC200 (a), Pd (b), Ag (c) and Cd (d) elemental mapping of the PdAg<sub>10</sub>Cd<sub>10</sub>/PAC200 sample. Relatively uniform dispersion of the Pd, Ag and Cd elements on the activated carbon is evident, which is consistent with the TEM analysis (Figure 3.1c).

The Brunauer – Emmett – Teller (BET) surface areas and pore structures of the fabricated catalysts were characterized via N<sub>2</sub> adsorption and desorption at 77 K. The typical N<sub>2</sub> adsorption/desorption isotherm at 77K for the PdAg<sub>10</sub>Cd<sub>10</sub>/PAC200 sample is shown in Figure 3.4a. This type IV isotherm was shown for all samples with closure occurring at approximately  $P/P_0 \sim 0.40$ , revealing that the synthesized PAC200 supported Pd-based nanoparticles possessed mesopore structure. The isotherm was further fitted using the quenched–solid density functional theory (QSDFT) method, as shown in Figure 3.4b, which is

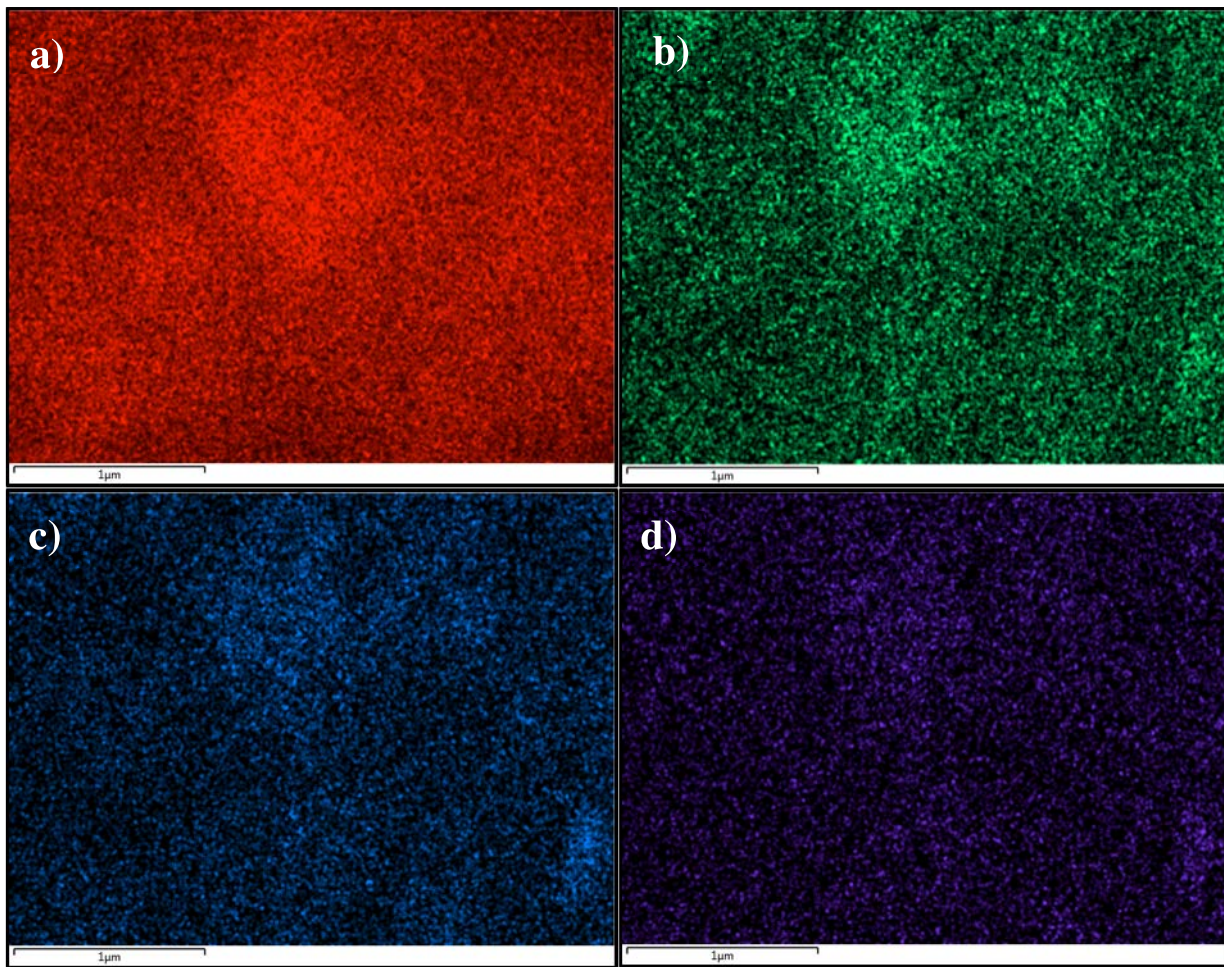


**Figure 3.3.** EDX mapping distribution images of PAC200 (a), Pd (b), Ag (c) and Cd (d) content for PdAg<sub>10</sub>Cd<sub>10</sub>/PAC200 sample.

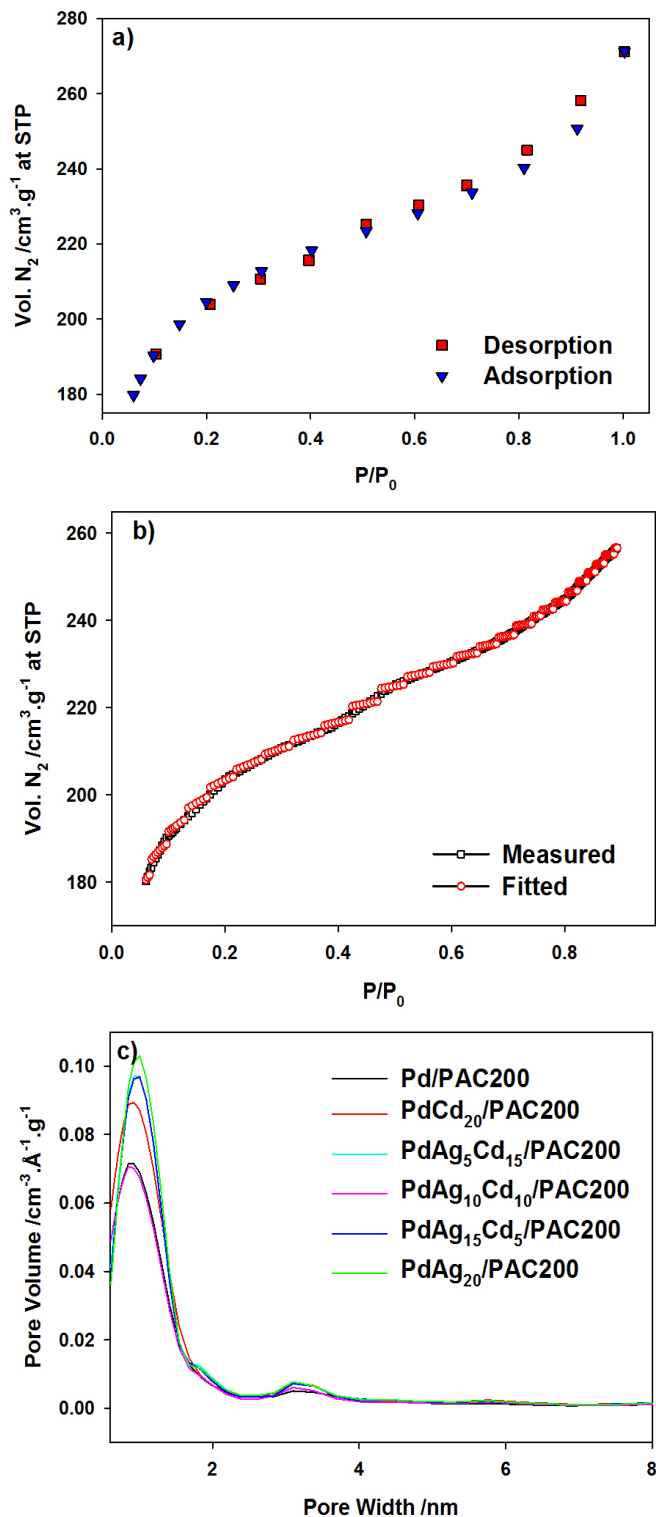


**Figure 3.4.** N<sub>2</sub> adsorption/desorption isotherm at 77 K on the PdAg10Cd10/PAC200 sample (a), and corresponding desorption curve fitted using QSDFT method (b). The pore size distributions using QSDFT method are shown in (c).

commonly employed for the characterization of pore sizes, with a fitting error of less than 0.3% in all cases. Pore size distribution was determined for each using this technique and plotted in Figure 3.4c. The pore size distribution plots reveal the presence of two primary pore structures. A micropore peak at approximately 0.94 nm, followed by a mesopore peak at roughly 3.1 nm can be seen. The micropore and mesopore peaks follow similar trends in order of peak height for all the synthesized PAC200 supported Pd-based nanoparticles.

The BET surface areas, total pore volumes, micropore volumes, mesopore volumes, and modal micropore and mesopore diameters of the fabricated samples are listed in Table 3.2, confirming that the synthesized Pd-based catalysts possessed a high surface area as well as microporous and mesoporous structures. In comparison to the reported value of PAC200 (1037 m<sup>2</sup>/g),<sup>9</sup> it becomes evident that the introduction of metal catalysts to the carbon surface decreased the surface area. This can be attributed to the blocking of micropores within the carbon by the metal nanoparticles. In comparing the mono-, bi-, and tri-metallic modified activated carbon samples, it is clear that the addition of multiple metal dopants serves to increase the mesopore volume. Interestingly, among all bi- and tri-metallic doped samples, the micropore volume remains relatively consistent, with the exception of PdAg<sub>10</sub>Cd<sub>10</sub>. This may be caused by the impregnation method, NaBH<sub>4</sub> reduction, increasing the volume of some mesopores while maintaining consistent nanoparticle size morphology among all samples. Inconsistencies arise between the methods used to acquire pore volumes, where mesopore and micropore volumes exceed that of the total pore volume. This discrepancy might be caused by an overlap in pore diameters measured by the Dubinin–Astakhov (DA) and Barrett–Joyner–Halenda (BJH) methods. The Dubinin–Astakhov method measures micropores at a pore diameter range between 0.2 and 60 Å, whereas the Barrett–Joyner–Halenda technique for

quantifying mesopore volumes examines pores with a diameter range between 32.8 and 189 Å. The modal micropore diameter obtained using the DA method varies from 1.52 to 1.60 nm. The modal mesopore diameter obtained using the BJH method ranges from 3.59 to 3.65 nm. The QSDFT method shows a modal micropore diameter of 0.94 nm and a mesopore diameter of 3.1 nm, indicating a diameter shift of approximately 0.5 nm between the two methods.

**Table 3.2.** Textural parameters of metal dispersed activated carbon samples from N<sub>2</sub> adsorption/absorption isotherms at 77 K.

Sample	SA <sub>BET</sub> (m <sup>2</sup> g <sup>-1</sup> ) <sup>a</sup>	V <sub>t</sub> (cc/g) <sup>b</sup>	V <sub>micro,DA</sub> (cm <sup>3</sup> g <sup>-1</sup> ) <sup>c</sup>	V <sub>meso,BJH</sub> (cm <sup>3</sup> g <sup>-1</sup> ) <sup>d</sup>	D <sub>micro</sub> (nm) <sup>e</sup>	D <sub>meso</sub> (nm) <sup>f</sup>
<b>Pd/PAC200</b>	721	0.414	0.364	0.087	1.56	3.64
<b>PdCd<sub>20</sub>/PAC200</b>	895	0.535	0.449	0.123	1.58	3.63
<b>PdAg<sub>5</sub>Cd<sub>15</sub>/PAC200</b>	742	0.523	0.444	0.116	1.52	3.63
<b>PdAg<sub>10</sub>Cd<sub>10</sub>/PAC200</b>	660	0.420	0.354	0.097	1.60	3.59
<b>PdAg<sub>15</sub>Cd<sub>5</sub>/PAC200</b>	861	0.516	0.427	0.117	1.58	3.65
<b>PdAg<sub>20</sub>/PAC200</b>	826	0.534	0.447	0.122	1.54	3.61

<sup>a</sup> The Brunauer–Emmett–Teller (BET) surface area (SA<sub>BET</sub>) was obtained using points within the relative pressure range 0.1–0.3. <sup>b</sup> The total pore volume (V<sub>t</sub>) was calculated at a relative pressure of 0.99. <sup>c</sup> The micropore volume (V<sub>micro,DA</sub>) was obtained using Dubinin–Astakhov (DA) method of analysis. <sup>d</sup> The Barrett–Joyner–Halenda (BJH) method was used to determine the volume of mesopores (V<sub>meso,BJH</sub>) using the desorption branch and ignoring points below a relative pressure of 0.35. <sup>e</sup> The modal micropore diameter (D<sub>micro,DA</sub>) was obtained using the Dubinin–Astakhov (DA) method. <sup>f</sup> The modal mesopore diameter (D<sub>meso,BJH</sub>) was obtained using the Barrett–Joyner–Halenda (BJH) method.

### 3.4 General Cyclic Voltammetric Behaviors of the Pd–based Catalysts.

Typical cyclic voltammograms (CVs) of the PAC200 supported Pd-based catalysts recorded in 0.5 M H<sub>2</sub>SO<sub>4</sub> at a scan rate of 5 mV/s are shown in Figure 3.5. The primary regions present in these CVs include the hydrogen region and the double layer region. The hydrogen region includes absorption/adsorption and subsequent desorption. In the hydrogen region, it can be noted that the decoupling of the adsorption from the absorption process became difficult as a result of the high current caused by hydrogen absorption. A broad peak due to desorption of hydrogen, ranging from -250 to -100 mV, appeared when scanning the electrode potential

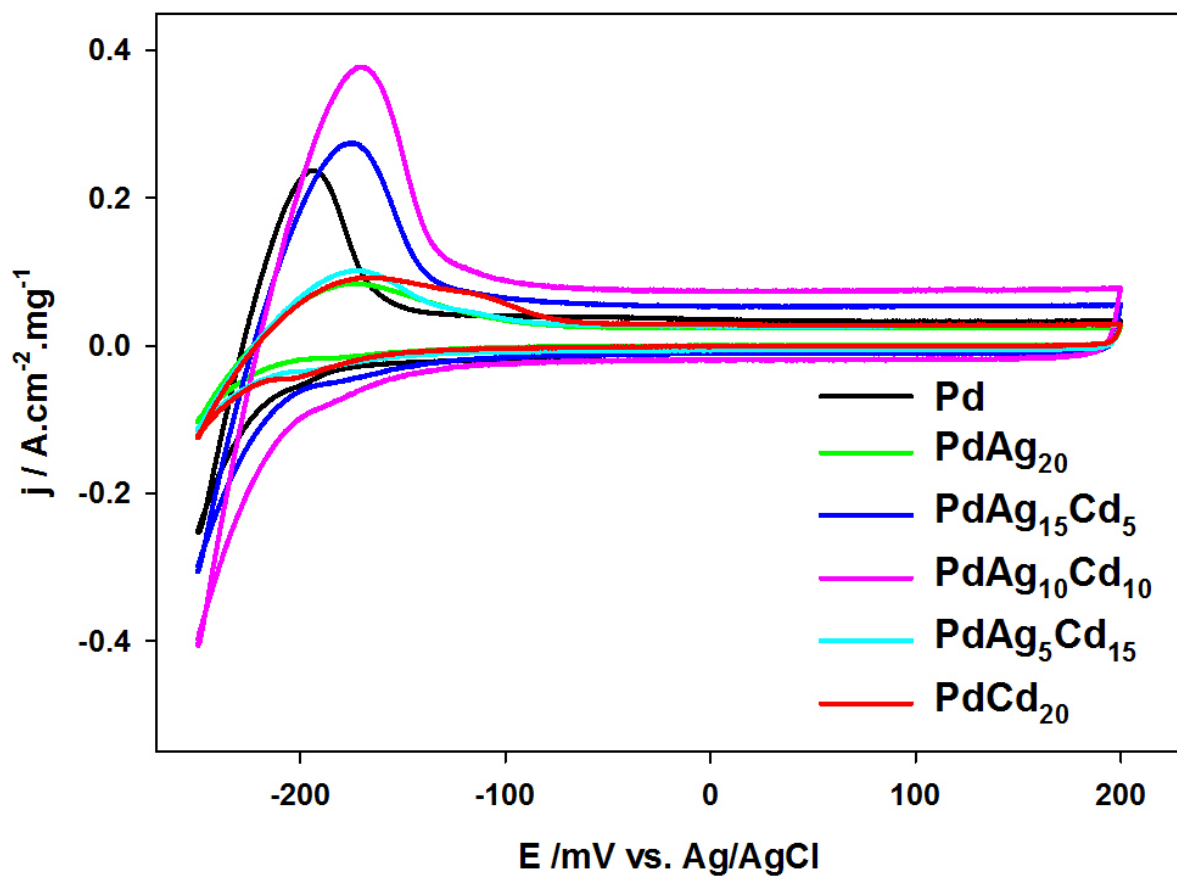


**Figure 3.5.** Cyclic voltammograms of the Pd-based nanostructures in 0.5 M H<sub>2</sub>SO<sub>4</sub> at a scan rate of 5 mV/s.

from -250 to 200 mV. With the addition of Ag and/or Cd, the peak became broader and the peak potential shifted to the positive direction, in comparison to the Pd/PAC200. By varying the amounts of Ag and Cd that are incorporated into the Pd of the tri-metallic alloys, the capacity of hydrogen sorption of the PAC200 supported Pd-Ag-Cd nanoparticles is strongly impacted. The peak intensity of the hydrogen desorption was increased in the following order: Pd/PAC200 < PdAg<sub>5</sub>Cd<sub>15</sub>/PAC200 < PdAg<sub>10</sub>Cd<sub>10</sub>/PAC200. In contrast, the hydrogen desorption peak of the PdAg<sub>20</sub>/PAC200, PdCd<sub>20</sub>/PAC200 and PdAg<sub>5</sub>Cd<sub>15</sub>/PAC200 nanoparticles was much smaller than that of the Pd/PAC200 sample.

### **3.5 Potential and Composition Dependence of Pd-based Catalysts on Hydrogen**

#### **Electrosorption.**

The synthesized Pd-based catalysts were studied at various electrode potentials, ranging from -200 to -250 mV versus Ag/AgCl. The potential was initially held constant for one minute followed by cyclic voltammetry, which was run immediately afterward, proceeding from the held potential to 200 mV. A holding period of one minute was determined by a series of hydrogen discharge experiments (not shown here). It was revealed that one minute was of a sufficient duration to achieve the complete saturation of hydrogen into the thin film of the Pd-based nanoparticles coated on the glass carbon electrode. For clarification, Figure 3.6 only shows the anodic scan of the CVs for the Pd/PAC200 (a) and PdAg<sub>10</sub>Cd<sub>10</sub>/PAC200 nanoparticles (b) recorded at a sweep rate of 5 mV/s following the complete saturation with hydrogen at various potentials (-200 to -250 mV). The intensity of the hydrogen desorption/oxidation peak is strongly contingent on the held electrode potential, where the lower the potential, the larger the peak. A lower electrode potential, under electrochemical conditions, corresponds to a higher hydrogen pressure in gas-phase experiments.<sup>32,33</sup> The lowest

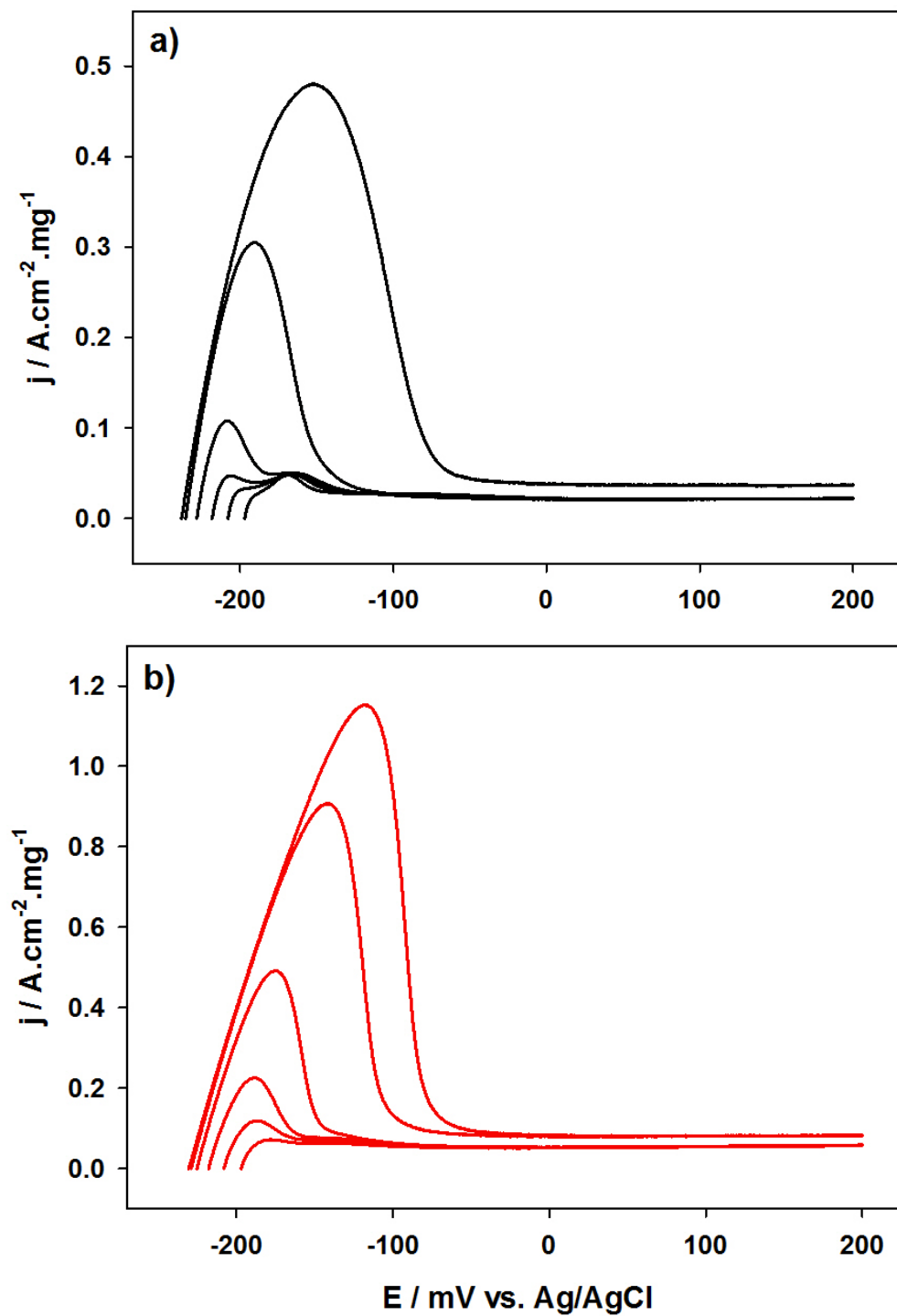


**Figure 3.6.** Anodic sweeps of desorption of hydrogen from Pd/PAC200 (a) and PdAg<sub>10</sub>Cd<sub>10</sub>/PAC200 (b) after holding the potential at various cathodic limits for one min in 0.5 M H<sub>2</sub>SO<sub>4</sub>. The scan rate was 5 mV/s.

electrode potential used in this study was -250 mV, as significant hydrogen evolution was observed when the applied potentials were lower than -250 mV.

In order to quantitatively examine the effect of the held potential on the capacity of the hydrogen sorption into the Pd-based PAC200 nanoparticles, the total hydrogen discharge was calculated by integrating the hydrogen desorption/oxidation peak shown in Figure 3.6. The overall hydrogen oxidation charges ( $Q_H$ ) for each Pd-based PAC200 nanoparticles at the different held potentials are displayed in Figure 3.7. For all the synthesized Pd-based PAC200 nanoparticles,  $Q_H$  was slightly increased when the held potential was decreased from -200 to -220 mV. A significant increase appeared when the held potential was further decreased from -220 to -250 mV.

As previously stated, variations in the amounts of Ag and Cd that are incorporated into the Pd of the tri-metallic alloys strongly impacted the capacity of hydrogen sorption of the Pd-Ag-Cd nanoparticles. When the Ag or Cd contents are maximized (at an atomic +15%), the catalytic hydrogen sorption capacity is shown to decrease. This becomes more apparent with regards to an increase in Cd, wherein an equal atomic percent, as seen in the PdAg<sub>10</sub>Cd<sub>10</sub> sample, gives rise to the highest  $Q_H$ , indicating improved hydrogen sorption capabilities under electrochemical conditions. The sudden decrease in the sorption capabilities of maximized Ag and Cd contents may be accounted for by the properties of nanomaterials. It is commonly known that the properties of nanomaterials are dependent on the size of their crystallite structures. As seen previously<sup>29,31</sup>, exceeding optimized alloy percentages greatly decreases the ability of the nanoparticles to sorb hydrogen. With specific regard to the PdAg<sub>5</sub>Cd<sub>15</sub> sample, the hydrogen sorption decrease may also be attributed to variation in reduction potentials. Both Pd<sup>2+</sup> and Ag<sup>+</sup> are easily reduced, allowing the relative quantities of Pd and Ag

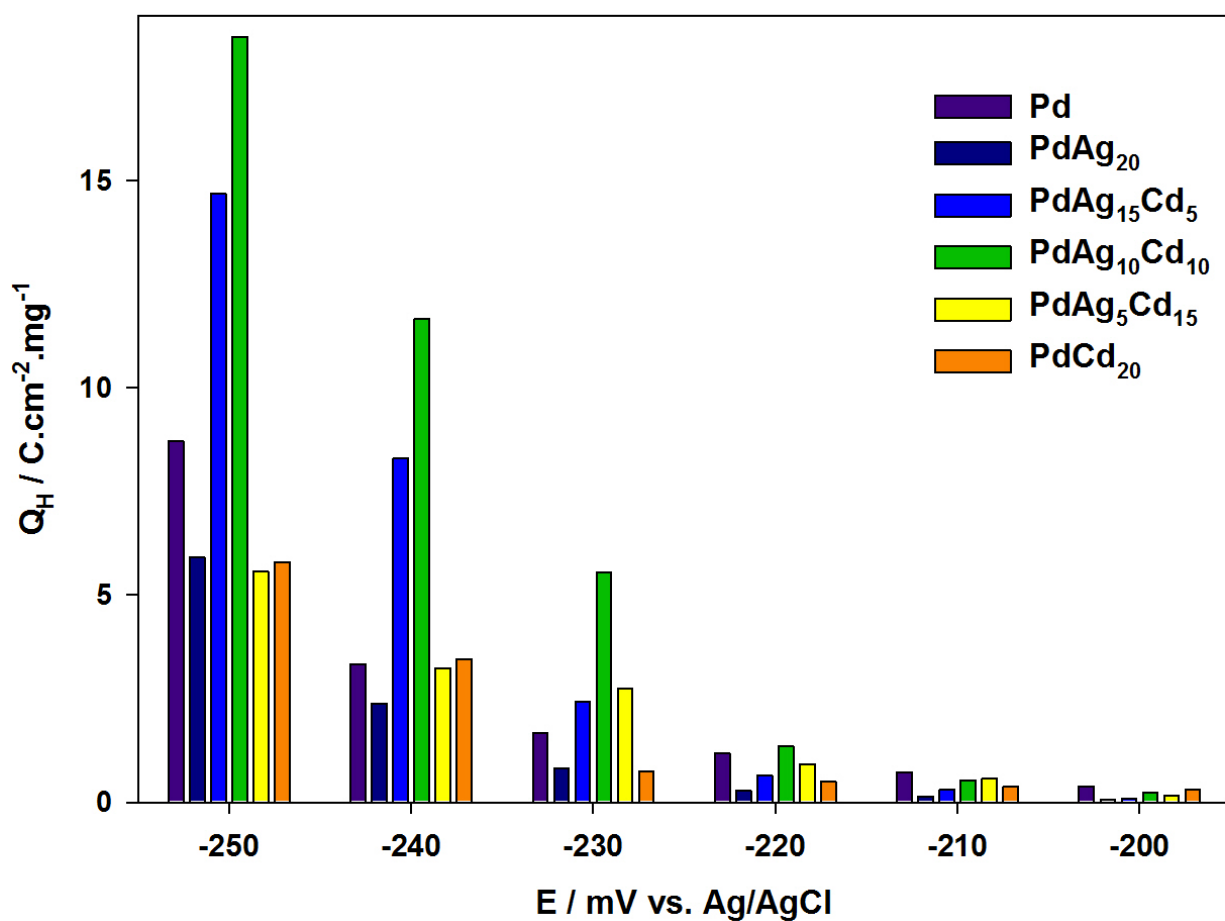


**Figure 3.7.** The overall hydrogen oxidation charges ( $Q_H$ ) for each Pd based sample at various cathodic limits.

to grow at a similar rate. In comparison,  $\text{Cd}^{2+}$  is much more difficult to reduce causing the Cd nanoparticle growth to remain in closer proximity to the outer surface. This variation in reduction rate could lead to an enriched Cd content on the surface, straying further from the ideal catalyst surface composition.

The above results indicate that both potential and composition play a significant role in the overall capacity for hydrogen sorption. Indicating that with regards to Pd-Ag-Cd catalysts optimized hydrogen sorption results appear at a held potential of -250 mV and an equal Ag and Cd composition,  $\text{PdAg}_{10}\text{Cd}_{10}$ . As seen with the CVs (Figure 3.5), the  $Q_{\text{H}}$  at -250 mV was increased in the following order:  $\text{Pd}/\text{PAC200} < \text{PdAg}_5\text{Cd}_{15}/\text{PAC200} < \text{PdAg}_{10}\text{Cd}_{10}/\text{PAC200}$ , with the  $\text{PdAg}_{20}/\text{PAC200}$ ,  $\text{PdCd}_{20}/\text{PAC200}$  and  $\text{PdAg}_5\text{Cd}_{15}/\text{PAC200}$  nanoparticles possessing smaller hydrogen desorption charges than that of the  $\text{Pd}/\text{PAC200}$  sample. The charges for hydrogen desorption on the Pd-Ag-Cd nanoparticles with 5/15%, 10/10%, and 15/5% Ag/Cd were 5.57, 18.49, and 14.69  $\text{C}/\text{cm}^2\cdot\text{mg}$  respectively. Hence, it was clear that the  $\text{PdAg}_{10}\text{Cd}_{10}$  catalyst possessed the highest capacity for hydrogen sorption.

### 3.6 Synergistic Effects of Activated Carbon Supported $\text{PdAg}_{10}\text{Cd}_{10}$ Nanoparticles

The spillover effect is well known in the field of heterogeneous catalysis,<sup>34</sup> and it has been largely debated recently in relation with hydrogen storage in adsorbed states.<sup>9,35-37</sup> Hydrogen spillover is commonly described as the dissociative adsorption of  $\text{H}_2$  on metal catalyst particles, followed by the migration of H atoms to the support and diffusion of the atoms on the support.<sup>27,28</sup> Attaining enhanced hydrogen storage on adsorbents such as activated carbon, may be achieved by exploiting hydrogen spillover at the gas-solid interface.<sup>2,10</sup> To assess the hydrogen uptake enhancement of the PAC200 supported  $\text{PdAg}_{10}\text{Cd}_{10}$  nanoparticles at the electrode-electrolyte interface, we further studied the electrochemical behaviors of the

PAC200 support in the absence of any metal catalyst and the PdAg<sub>10</sub>Cd<sub>10</sub> catalysts in the absence of the PAC200 support. CVs at -250 mV for the PAC200 support and PdAg<sub>10</sub>Cd<sub>10</sub>, Figure 3.8 and Figure 3.9 respectively, were performed to determine individual hydrogen sorption capabilities. Due to the lack of catalyst present with the PAC200 sample in Figure 3.8 the mass taken into consideration was the mass of total PAC200. Under electrochemical conditions at room temperature, PAC200 exhibits no peak due to desorption of hydrogen, indicating the necessary presence of a catalyst. With respect to the PdAg<sub>10</sub>Cd<sub>10</sub> catalyst, a peak due to desorption of hydrogen was present after scanning the electrode potential from -250 mV to 200 mV (Figure 3.9), which is different from the CV curves displayed in Figure 3.5. To measure the hydrogen sorption capacity of the PdAg<sub>10</sub>Cd<sub>10</sub> nanoparticles dispersed on a glass carbon electrode (GCE) surface, the anodic sweeps of the hydrogen desorption from PdAg<sub>10</sub>Cd<sub>10</sub> after being held at various electrode potentials for one minute are presented in Figure 3.10. The peak intensity was increased with the negative shifting of the applied cathodic potential limits. The insert of Figure 3.10 displays the hydrogen desorption charge ( $Q_H$ ) of the PdAg<sub>10</sub>Cd<sub>10</sub> nanoparticles versus potential. For comparison, the anodic sweeps of the PdAg<sub>10</sub>Cd<sub>10</sub> nanoparticles and the PAC200 supported PdAg<sub>10</sub>Cd<sub>10</sub> nanoparticles after being held at -250 mV for one minute are presented in Figure 3.11a. It should be noted that the non-supported PdAg<sub>10</sub>Cd<sub>10</sub> catalyst current density ( $j$ ) is multiplied by a factor of 50. Upon first glance, it is evident that a positive oxidation peak potential shift occurs when the PdAg<sub>10</sub>Cd<sub>10</sub> nanoparticles were dispersed on PAC200. In addition, a drastic increase in the desorption peak was observed when compared to that of the unsupported PdAg<sub>10</sub>Cd<sub>10</sub> catalysts. Taking into account of the electrochemical results presented in Figure 3.8 – 3.10, the drastic difference seen in Figure 3.11a confirms the occurrence of a significant synergistic effect,<sup>38-40</sup> which may be

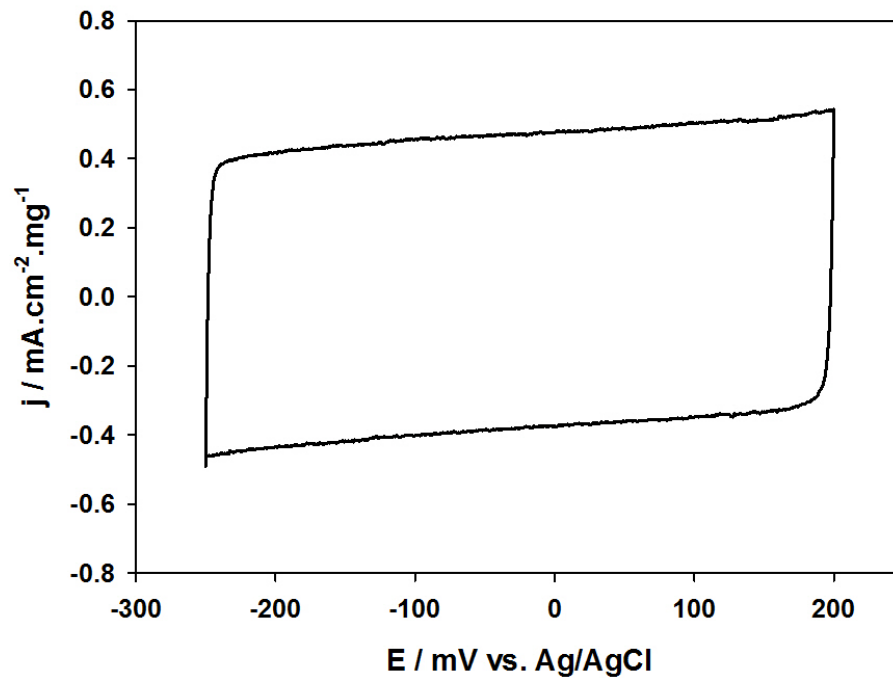


**Figure 3.8.** Cyclic voltammogram of the PAC200 sample in 0.5 M H<sub>2</sub>SO<sub>4</sub> at a scan rate of 5 mV/s.

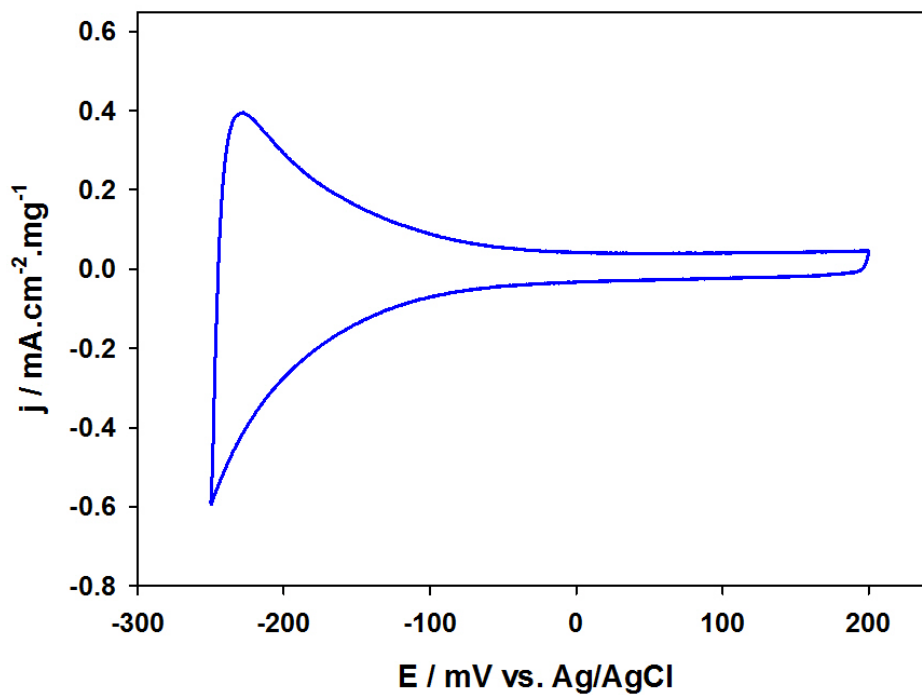


**Figure 3.9.** Cyclic voltammogram of the PdAg<sub>10</sub>Cd<sub>10</sub> nanostructures in 0.5 M H<sub>2</sub>SO<sub>4</sub> at a scan rate of 5 mV/s.

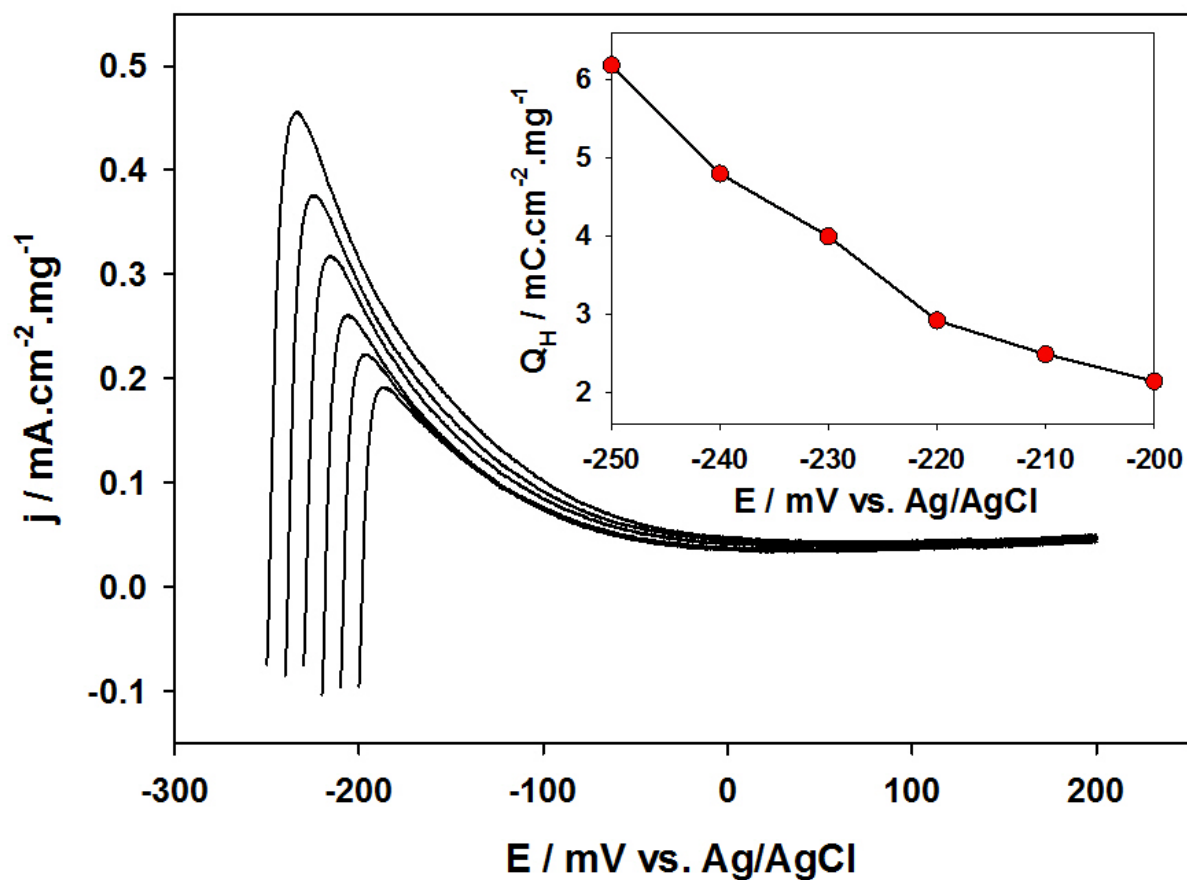


**Figure 3.10.** Anodic sweeps of desorption of hydrogen from  $\text{PdAg}_{10}\text{Cd}_{10}$  after holding the potential at various cathodic limits for one min in 0.5 M  $\text{H}_2\text{SO}_4$ . The scan rate was 5 mV/s. Hydrogen desorption charge ( $Q_H$ ) of the  $\text{PdAg}_{10}\text{Cd}_{10}$  nanoparticles versus potential is shown in the inset.

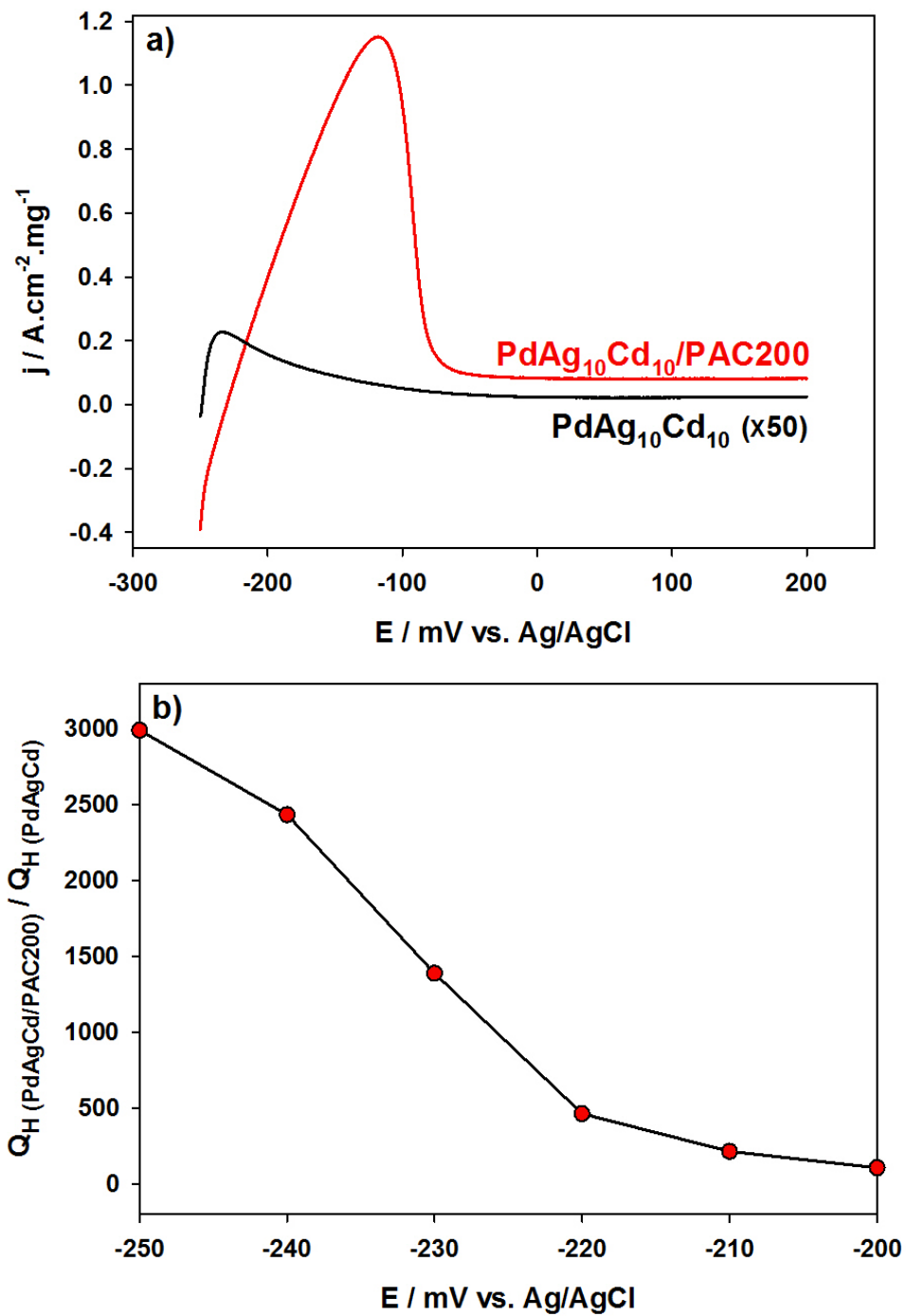


**Figure 3.11.** Anodic sweeps of the  $\text{PdAg}_{10}\text{Cd}_{10}/\text{PAC200}$  and  $\text{PdAg}_{10}\text{Cd}_{10}$  nanoparticle samples after holding the potential at -250 mV for one min. in 0.5 M  $\text{H}_2\text{SO}_4$  at a scan rate of 5 mV/s are shown in (a). Note: the  $\text{PdAg}_{10}\text{Cd}_{10}$  non-supported sample's current density ( $j$ ) is multiplied by a factor of 50 for viewing purposes. Corresponding ratios of charge due to hydrogen desorption versus potential (b) follows.

attributed to the hydrogen surface diffusion. Wieckowski and co-workers studied CO surface diffusion on Pt and PtRu nanoparticles using  $^{13}\text{C}$  electrochemical nuclear magnetic resonance spectroscopy,<sup>41</sup> showing that CO surface diffusion is very rapid and that the addition of Ru to Pt further increases the surface diffusion rates of CO. In the case of the PAC200 supported PdAg<sub>10</sub>Cd<sub>10</sub> nanoparticles, when the electrode potential was held at -250 mV, hydrogen ions were electrochemically reduced to hydrogen atom initially at the PdAg<sub>10</sub>Cd<sub>10</sub> nanoparticles and subsequently diffused to the activated carbon. To assess the level of the enhancement due to the synergistic effect between the PdAg<sub>10</sub>Cd<sub>10</sub> nanoparticles and the activated carbon, Figure 3.11b displays the corresponding  $Q_{\text{H, supported}}/Q_{\text{H, non-supported}}$  ratios for PdAg<sub>10</sub>Cd<sub>10</sub> at various potentials. Significant increase was observed as the potential was shifting to more negative. At -250 mV, the hydrogen sorption capacity of the PdAg<sub>10</sub>Cd<sub>10</sub>/PAC200 nanoparticles was ~3000 times higher than that of the non-supported PdAg<sub>10</sub>Cd<sub>10</sub> catalyst. The above results show that the dispersal of the PdAg<sub>10</sub>Cd<sub>10</sub> catalyst onto the surface of the PAC200 is an important factor to facilitate the improved electrochemical hydrogen storage of the activated carbon.

### 3.7 Conclusions

In summary, the PdAgCd catalysts were uniformly dispersed onto the surface of Norit PAC200 activated carbon using a facile sodium borohydride reduction method at room temperature. This method is effective for the control of the composition of the formed PdAgCd catalysts. The enhancement of hydrogen storage in this tri-metallic alloy, in contrast to Pd and the bi-metallic PdAg and PdCd catalysts, was determined via electrochemical methods. Additionally, through a comparison of the supported and non-supported Pd-Ag-Cd catalysts, it was found that synergistic effects between the nanoparticles and the carbon substrate drastically increased hydrogen storage capability. The significant synergistic effect can be attributed to the

electrochemical reduction of hydrogen ions initially at the Pd-based nanoparticles and the hydrogen surface diffusion subsequently to the activated carbon. The optimized composition of the Pd-Ag-Cd alloys was determined to be Pd<sub>80</sub>Ag<sub>10</sub>Cd<sub>10</sub> with the highest hydrogen sorption capacity of 18.49 C/cm<sup>2</sup>·mg. With increased kinetics and a decrease in the phase transition, the significant enhancement of hydrogen sorption, in comparison to the Pd-Ag and Pd-Cd bimetallic alloys, makes PdAgCd catalysts attractive and promising for use as hydrogen dissociation catalysts for applications in both hydrogen purification and storage.

## References

- (1) Wang, L.; Yang, R. T. *J. Phys. Chem. C* **2008**, *112*, 12486.
- (2) Wang, L.; Yang, R. T. *J. Catal. Rev.: Sci. & Eng.* **2010**, *52*, 411.
- (3) Schlapback, L.; Züttel, A. *Nature* **2001**, *414*, 353.
- (4) Schlapback, L. *Nature* **2009**, *460*, 809.
- (5) Eberle, U.; Felderhoff, M.; Schüth, F. *Angew. Chem. Int. Ed.* **2009**, *48*, 6608.
- (6) Paster, M. D.; Ahluwalia, R. K.; Berry, G.; Elgowainy, A.; Lasher, S.; McKenney, K.; Gardiner, M. *Int. J. Hydrogen Energy* **2011**, *36*, 14534.
- (7) Yamauchi, M.; Kobayashi, H.; Kitagawa, H. *ChemPhysChem* **2009**, *10*, 2566.
- (8) Zacharia, R.; Kim, K. Y.; Fazle Kibria, A. K. M.; Nahm, K. S. *Chem. Phys. Lett.* **2005**, *412*, 369.
- (9) Adams, B. D.; Ostrom, C. K.; Chen, S.; Chen, A. *J. Phys. Chem. C* **2010**, *114*, 19875.
- (10) Adams, B. D.; Chen, A. *Mater. Today* **2011**, *14*, 282.
- (11) Ströbel, R.; Garche, J.; Moseley, P. T.; Jörissen, L.; Wolf, G. *J. Power Sources* **2006**, *159*, 781.
- (12) Li, Y.; Yang, R. T. *J. Am. Chem. Soc.* **2006**, *128*, 726.
- (13) Oriňáková, R.; Oriňák, A. *Fuel* **2011**, *90*, 3123.
- (14) Jurewicz, K.; Frackowiak, E.; Béguin, F. *Technol.* **2002**, *77-78*, 415.

- (15) Fernández, P. S.; Castro, E. B.; Real, S. G.; Martins, M. E. *Int. J. Hydrogen Energy* **2009**, *34*, 8115.
- (16) Duncan, H.; Lasia, A. *Electrochem. Acta* **2007**, *52*, 6195.
- (17) Masika, E.; Mokaya, R. *J. Phys. Chem. C* **2012**, *116*, 25734.
- (18) Contescu, C. I.; Brown, C. M.; Liu, Y.; Bhat, V. V.; Gallego, N. C. *J Phys. Chem. C*. **2009**, *113*, 5886.
- (19) Yürüm, Y.; Taralp, A.; Veziroglu, T. N. *Int. J. Hydrogen Energy* **2009**, *34*, 3784.
- (20) Jena, P. *J. Phys. Chem. Lett.* **2011**, *2*, 206.
- (21) Parambath, V. B.; Nagar, R.; Sethupathi, K.; Ramaprabhu, S. *J. Phys. Chem. C* **2011**, *115*, 15679.
- (22) Łukaszewski, M.; Żurowski, A.; Grdeń, M.; Czerwiński, A. *Electrochem. Commun.* **2007**, *9*, 671.
- (23) Łukaszewski, M.; Kędra, T.; Czerwiński, A. *Electrochim. Acta* **2010**, *55*, 1150.
- (24) Łukaszewski, M.; Klimek, K.; Żurowski, A.; Kędra, T.; Czerwiński, A. *Solid State Ionics* **2011**, *190*, 18.
- (25) Hao, S.; Shol, D. S. *J. Phys. Chem. C* **2013**, *117*, 1217.
- (26) Chen, C.-H.; Chung, T.-Y.; Shen, C.-C.; Yu, M.-S.; Tsao, C.-S.; Shi, G.-N.; et al. *Int. J. Hydrogen Energy* **2013**, *38*, 3681.
- (27) Yang, Y. X.; Singh, R. K.; Webley, P. A. *Adsorption* **2008**, *14*, 256.
- (28) Zhao, W.; Fierro, V.; Zoltea, C.; Izquierdo, M. T.; Chevalier-César, C.; Latroche, M.; Celzard, A. *Int. J. Hydrogen Energy* **2012**, *37*, 5072.
- (29) Adams, B. D.; Wu, G.; Nigro, S.; Chen, A. *J. Am. Chem. Soc.* **2009**, *131*, 6930.
- (30) Adams, B. D.; Ostrom, C. K.; Chen, A. *Langmuir* **2010**, *26*, 7632.
- (31) Chen, S.; Adams, B. D.; Chen, A. *Electrochim. Acta* **2010**, *56*, 61.
- (32) Comisso, N.; De Ninno, A.; Del Giudice, E.; Mengoli, G. Soldan, P. *Electrochim. Acta* **2004**, *49*, 1379.
- (33) Zurowski, A.; Łukaszewski, M.; Czerwinski, A. *Electrochim. Acta* **2006**, *51*, 3112.

## Chapter 4. Enhanced Electrocatalytic Activity of Pd Nanoparticle Modified TiO<sub>2</sub> Nanotubes: A Comparison of UV and EC Pretreatment Methods

### 4.1 Introduction

Fuel cells, with high-energy efficiency and clean emissions, transpire as promising energy solutions for the future. For portable electronics and automobile industry applications, polymer electrolyte membrane fuel cells (PEMFCs) are emerging as among the top promising candidates due to their advantages of high power densities and compact nature.<sup>1-3</sup> Due to its potential for a wide range of applications, titanium dioxide (TiO<sub>2</sub>)<sup>4-9</sup> has received considerable attention for its use as a support material. Titania nanotubes (TiO<sub>2</sub> NTs) in particular have received sizeable consideration recently as a result of their large surface area, low cost, and semiconducting properties.<sup>10-12</sup> TiO<sub>2</sub> NTs peculiar architecture, a large active surface area without an increase in geometric area, and improved stability due to strong electronic interactions between the support and deposits are some of its most desired properties.<sup>4,13,14</sup> As well, the nanotubular substrate arrangement can contribute to reduced accumulation of catalyst, leading to an increase in reactivity and specific reaction rates.<sup>4,14</sup> This allows for a considerable decrease in the loading of expensive noble metal catalysts.

A relatively simple technique for fabrication, electrochemical anodization of titanium in fluorinated electrolytes, is employed in this study. The anodization of TiO<sub>2</sub> NTs in a fluoride-based electrolyte (i.e. DMSO + HF) offers relative ease in preparation and controlled synthesis; however, presents the issue of comparatively low activity.<sup>15-22</sup> Considerable efforts have been made to further improve the conductivity of TiO<sub>2</sub> NT supports by means of various modifications. These modifications are primarily carried out via heat treatments, the introduction of other elements, or the introduction of tube-wall decorations.<sup>4,14-16,23</sup> In the

present study, we have investigated the effects of the ultraviolet light and electrochemical pretreatment methods on TiO<sub>2</sub> NTs with the aim of improving their electroactivity. Using Pd as the dispersed catalyst, the effects of the pretreatment methods were further examined through hydrogen electrosorption and formic acid electrooxidation. The objectives of this study were three-fold: (i) to further enhance the electroactivity of the TiO<sub>2</sub> NT support, (ii) to compare the efficacy of pretreatment methods, and (iii) to subsequently improve the electroactivity of the substrate while decreasing the noble metal load. Our studies have shown that UV and EC pretreatments of TiO<sub>2</sub> NTs significantly increase the electroactivity of the substrate, demonstrating a considerable enhancement in current under various electrochemical conditions.

## 4.2 Experimental Section

The TiO<sub>2</sub> NT supported Pd nanostructures were fabricated using a room temperature impregnation method, as described in Chapter 2. NaBH<sub>4</sub> was used as the reducing agent and Pd(NO<sub>3</sub>)<sub>2</sub> served as the metal precursor. UV and EC pretreatments of the TiO<sub>2</sub> NTs were carried out as described in Chapter 2. Four coats of the prepared Pd solution (described in Chapter 2) were deposited onto the surface of the TiO<sub>2</sub> NTs. All of the electrodes that were fabricated and studied had similar coating loads between 0.15 mg to 0.20 mg. The coating loads of the electrodes were determined by weighing the TiO<sub>2</sub> NT plate prior to and after being coated with the Pd nanostructures with a mass balance, accurate to 0.01 mg.

The surface morphology of the fabricated samples was characterized using SEM and EDX analysis. SEM images and surface analysis via EDX technique were obtained using a Hitachi Su-70 Schottky Field Emission SEM. The XRD patterns of the as-prepared samples were recorded using a Philips PW 1050-3710 Diffractometer with Cu K $\alpha$  radiation.

An investigation of the electrochemical performance of the electrodes was carried out in a

three-electrode electrochemical cell at room temperature (see Chapter 2). The reference electrode was Ag/AgCl (1 M KCl) and the fabricated Pd/TiO<sub>2</sub> NT electrodes were used as the working electrode. An electrolyte of 0.5 M H<sub>2</sub>SO<sub>4</sub> was employed to examine the hydrogen sorption and desorption behaviours of the electrode, and an electrolyte of 0.5 M H<sub>2</sub>SO<sub>4</sub> + 0.1 M HCOOH was used to investigate the activity of formic acid electrooxidation. Prior to the electrochemical experiments, ultrapure argon gas (99.999%) was bubbled through the desired electrolyte solution for approximately 15 minutes. Subsequently, argon was allowed to flow continuously above the solution during the electrochemical measurements.

Electrochemical methods used in this work included cyclic voltammetry (CV), linear sweep voltammetry (LSV), chronoamperometry (CA), and electrochemical impedance spectroscopy (EIS). Hydrogen electrosorption studies were performed at a constant potential for 10 minutes, allowing for full hydrogen saturation. A scan rate of 20 mV/s was utilized for cyclic voltammetry to desorb the absorbed and adsorbed hydrogen. The amount of sorbed hydrogen was calculated in the form of the oxidation charge,  $Q_H$ , which was obtained by the integration of voltammetric curves that were recorded during hydrogen desorption. Regarding the electrooxidation of formic acid, chronoamperometric measurements were carried out by initially holding the potential at 0 mV for 10 seconds, then stepping to various potentials for 10 minutes. The amplitude of modulation potentials for EIS measurements was 10 mV. Mott-Schottky plots were measured with VoltaLab 80 Potentiostat (PGZ402), with the potential range varied from -400 mV to 1200 mV vs. Ag/AgCl.

### **4.3 Surface Analysis of the TiO<sub>2</sub> NT Electrodes**

The surface morphology of the prepared catalysts, which were dispersed on the TiO<sub>2</sub> nanotubes, was characterized using SEM. Typical SEM images of TiO<sub>2</sub> NTs, UV treated

Pd/TiO<sub>2</sub> NTs and EC treated Pd/TiO<sub>2</sub> NTs are depicted in Figure 4.1a, 4.2a and 4.2b, respectively. As shown in Figure 4.1a, the self-organized nanotubes formed on the pure titanium plate via the electrochemical anodization technique. All samples consisted of pored arrays with diameters in the range of 70 to 90 nm. EDX spectra (Figure 4.1b) of the TiO<sub>2</sub> NTs revealed strong oxygen and titanium peaks, confirming the composition of the formed TiO<sub>2</sub> NTs. Figure 4.1c displays the XRD patterns of the pretreated TiO<sub>2</sub> NT samples. The marked peaks (\*) are derived from the Ti substrate and the anatase phase of the TiO<sub>2</sub> NTs. Comparatively, there was no notable difference in the crystalline structure between the TiO<sub>2</sub> NT samples. Of note, however, it was visually evident that a drastic transition in the colour of the TiO<sub>2</sub> NTs (from light blue/grey to dark blue) occurred upon application of the pretreatments. For the Pd doped TiO<sub>2</sub> NT samples (Figure 4.2a and 4.2b) the Pd nanoparticles ranged in size from 7 to 11 nm, and were generally situated on the surface of the TiO<sub>2</sub> NT support in the form of Pd clusters. The EDX spectra of the Pd doped samples (Figure 4.2c) again displayed strong oxygen and titanium peaks, which confirmed the composition of the formed TiO<sub>2</sub> NTs. As well, the spectra indicated the successful incorporation of palladium into the TiO<sub>2</sub> NT substrates.

#### **4.4 General Cyclic Voltammetric Behaviour of the Pd/TiO<sub>2</sub> NT Nanostructures**

For general hydrogen electroadsorption characterization of the treated and untreated TiO<sub>2</sub> nanotubes, cyclic voltammograms (CVs) were recorded in 0.5 M H<sub>2</sub>SO<sub>4</sub> at a scan rate of 20 mV/s (Figure 4.3). The main regions present in these CVs include the hydrogen region and the double layer region. Within the hydrogen region, hydrogen adsorption/absorption and subsequent desorption occur, showing a minimal increase in current peak density amongst all three samples. The largest notable change occurred within the double layer region, where a significant increase in the double layer capacitance was seen with the pretreated samples in

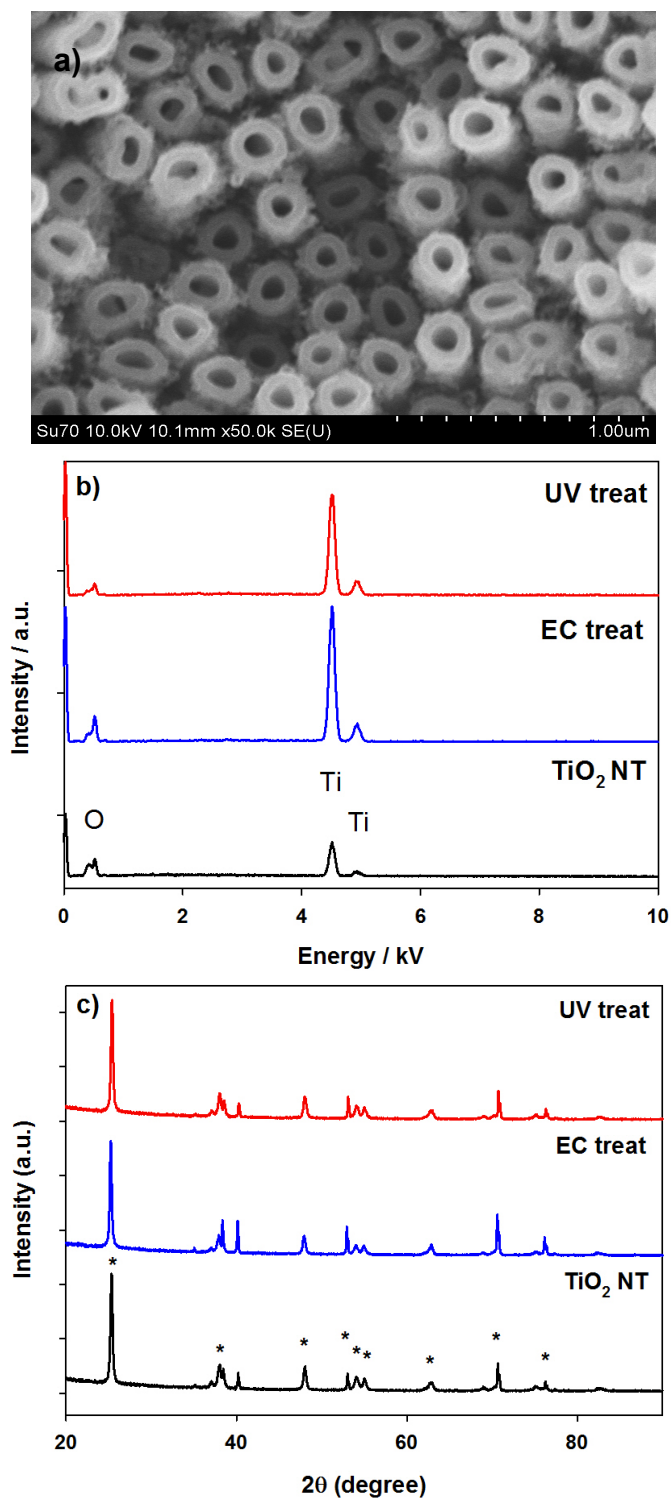


**Figure 4.1.** SEM images of TiO<sub>2</sub> NTs (a), at 50,000 × magnification. EDX spectra (b) and XRD patterns (c) of the prepared TiO<sub>2</sub> NT samples prior to and following the UV and EC pretreatment. Diffraction peaks belonging to the Ti substrate and the anatase phase of the TiO<sub>2</sub> NTs are labeled with (\*).

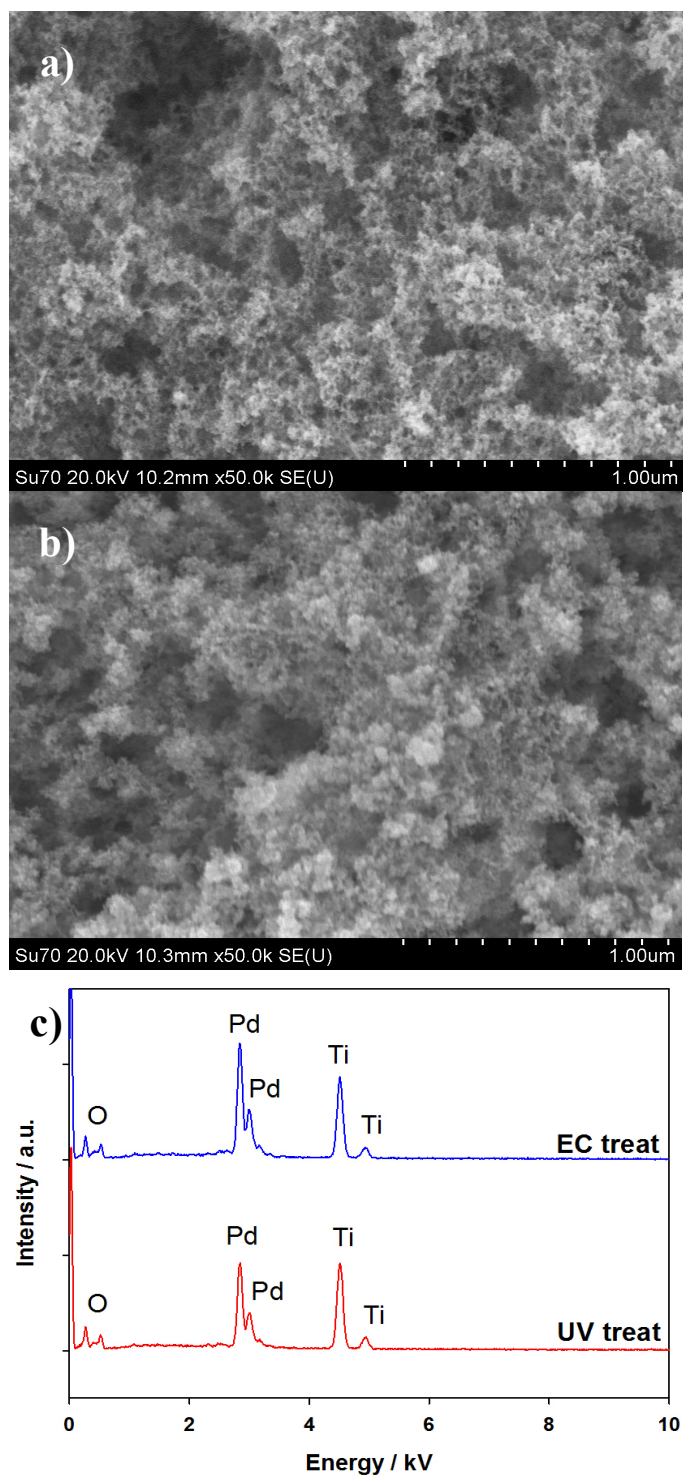


**Figure 4.2.** SEM images of Pd-doped TiO<sub>2</sub> NTs with UV pretreatment (a), and EC pretreatment (b), at 50,000 × magnification, and EDX spectra of the samples (c).

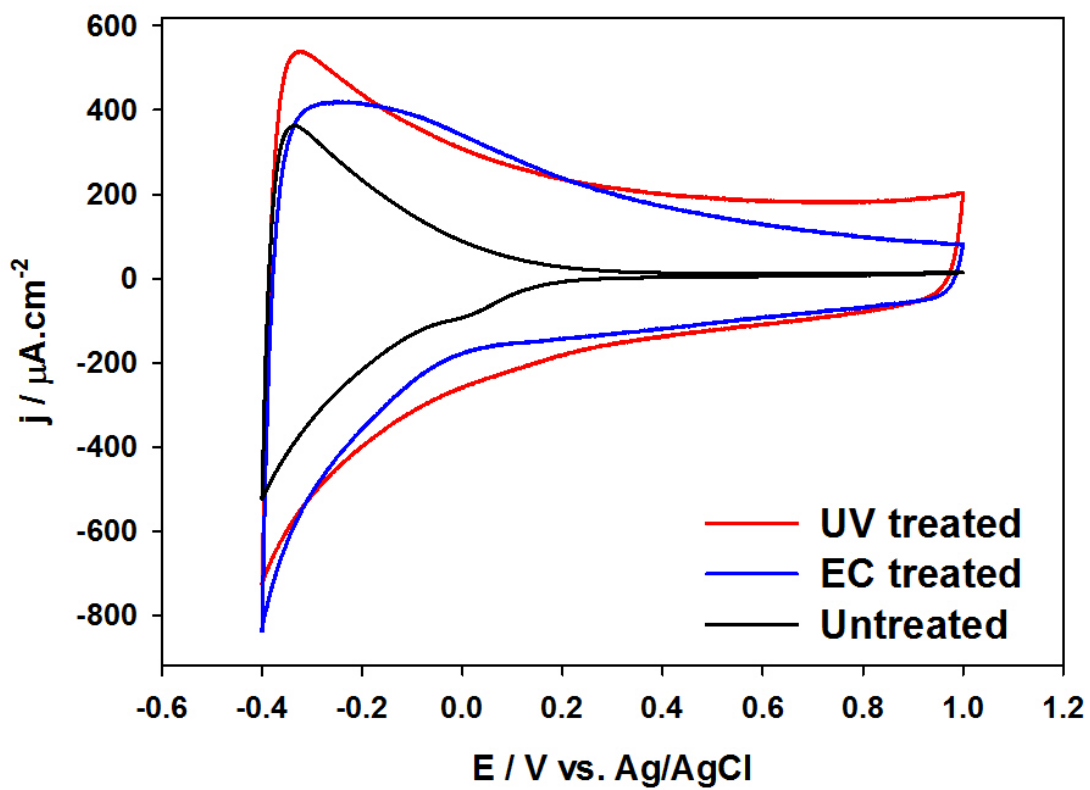


**Figure 4.3.** Cyclic voltammograms of  $\text{TiO}_2$  NTs after varying treatment methods in 0.5M  $\text{H}_2\text{SO}_4$  at a scan rate of 20 mV/s.

comparison to the untreated TiO<sub>2</sub> NTs.

Once doped with palladium, cyclic voltammograms (CVs) were performed to further characterize the samples in 0.5 M H<sub>2</sub>SO<sub>4</sub> at a scan rate of 20 mV/s. Figure 4.4 shows the CV results of the pretreated and untreated Pd doped TiO<sub>2</sub> NTs. It should be noted that the overall current density is normalized by the total mass of the Pd catalyst load carried by the TiO<sub>2</sub> NTs. Compared to the CVs of the un-doped samples in Figure 4.3, a significant increase in the current density took place. With the addition of the Pd catalyst, the hydrogen region was also extended into the double layer. This can be attributed to the catalytic properties of Pd toward hydrogen dissociation.<sup>24</sup> Regarding the UV pretreated Pd doped sample, the presence of two anodic peaks was noted. This provided evidence of structural changes, as well as new interactions formed between the Pd active sites and TiO<sub>2</sub> NTs.

## **4.5 Electrosorption of Hydrogen**

### **4.5.1 Potential and Treatment Method Dependence of Hydrogen Electrosorption in the Pd/TiO<sub>2</sub> NT Nanostructures.**

The capacity of the prepared Pd nanostructures for hydrogen adsorption/absorption was studied using cyclic voltammetry at various potentials, from -200 to -350 mV. Prior to running cyclic voltammetry, the potential was held at a constant potential for 10 minutes to ensure the complete saturation of hydrogen. Figure 4.5 illustrates the anodic sweeps of the CVs of the Pd nanostructures supported on the various pretreated TiO<sub>2</sub> NT samples following the complete saturation with hydrogen at various potentials. The full desorption of hydrogen is notable for each sample at a scan rate of 20 mV/s. This was validated by the completion of the anodic curve to the double layer prior to the limit of 400 mV. As seen for all three Pd samples, there is a sharp transition between -320 and -330 mV. Compared to the amount of hydrogen that was

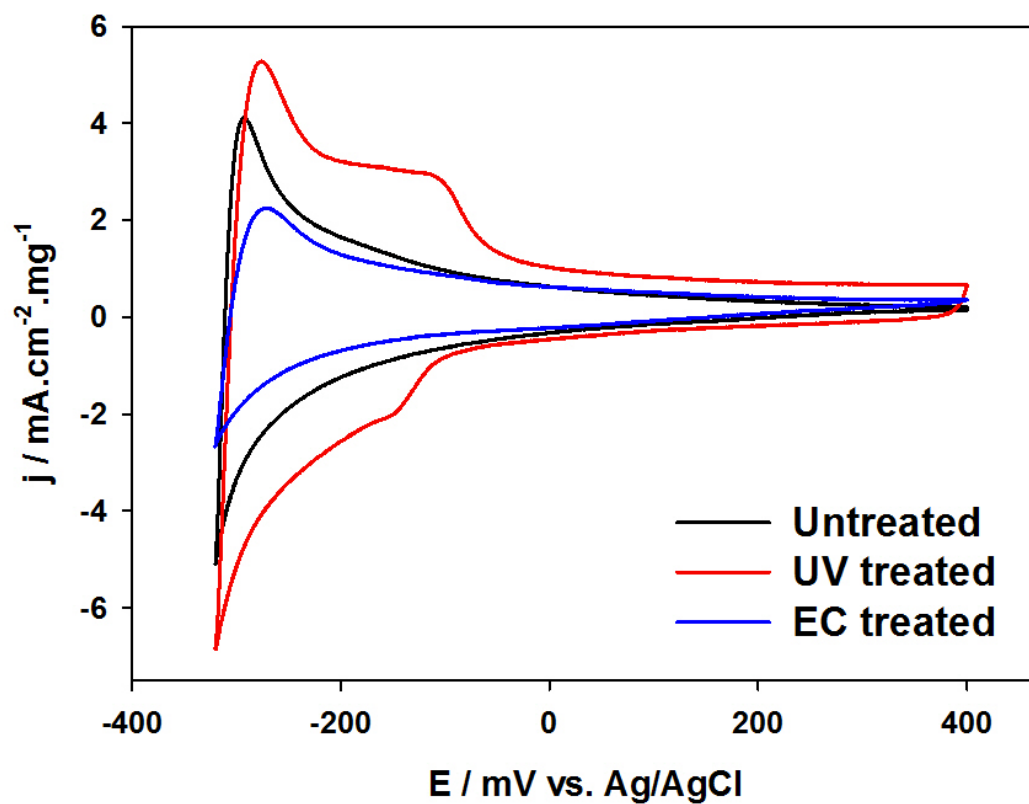


**Figure 4.4.** Cyclic voltammograms of Pd-doped TiO<sub>2</sub> NTs in 0.5M H<sub>2</sub>SO<sub>4</sub> at a scan rate of 20 mV/s.

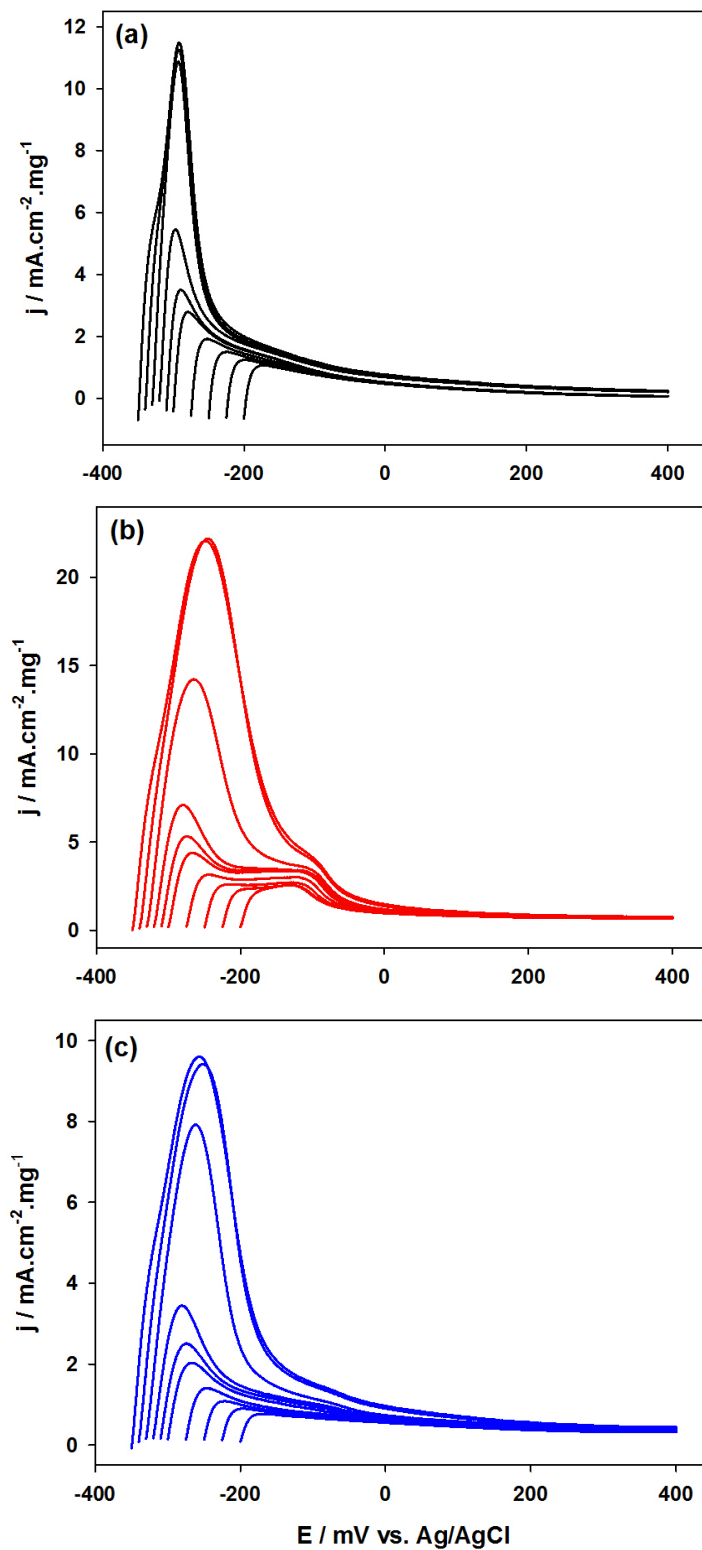


**Figure 4.5.** Anodic sweeps of desorption of hydrogen from untreated (a), UV treated (b), and EC treated (c) Pd/TiO<sub>2</sub> NTs after holding the potential at various cathodic limits for ten minutes in 0.5M H<sub>2</sub>SO<sub>4</sub>. The scan rate was 20 mV/s.

desorbed at potentials more negative than -330 mV, the amounts of hydrogen desorbed above -320 mV (more positive) are negligible. For the UV and EC treated samples, the transition between -320 mV and -330 mV were slightly less abrupt than the untreated TiO<sub>2</sub> NT sample. This phase is referred to as the  $\alpha$  to  $\beta$  phase transition, where both phases exist mutually.<sup>25</sup> In the case of Pd for all TiO<sub>2</sub> NT samples, at potentials more positive than -320 mV, there is exclusive  $\alpha$ -phase hydrogen, whereas at potentials  $\leq$  -330 mV there is exclusive  $\beta$ -phase hydrogen.

Hydrogen oxidation charges ( $Q_H$ ) for each Pd sample were used to quantitatively examine the effect of the held potential on the capacity of hydrogen sorption into the treated Pd doped TiO<sub>2</sub> NT samples. The total hydrogen discharge was calculated by integrating the hydrogen desorption/oxidation peaks shown in Figure 4.5. The overall  $Q_H$  for each Pd /TiO<sub>2</sub> NT electrode at different held potentials are displayed in Figure 4.6. As seen in the anodic sweeps, as the applied potential becomes increasingly negative, the amount of hydrogen desorbed increases. The maximum  $Q_H$  is seen at -350 mV for all of the Pd samples under study. At potentials more negative, a substantial amount of hydrogen evolution was observed. From the  $Q_H$  it becomes evident that in comparing the impacts of pretreatment methods, UV pretreatment significantly enhances hydrogen uptake, while EC pretreatment results in a hydrogen uptake that is practically equivalent to that of the non-treated sample, with a slight increase nearer to the maximum potential. The largest enhancement in the UV pretreated samples  $Q_H$  arises at potentials more negative than -320 mV. This occurrence may be accounted for by an enhancement in surface area<sup>17</sup> due to a reduction in impurities after undergoing UV treatment. As for the EC pretreated sample, the enhancement nearer -350 mV might be accounted for by the increased activity and stability of the electrode. At the maximum

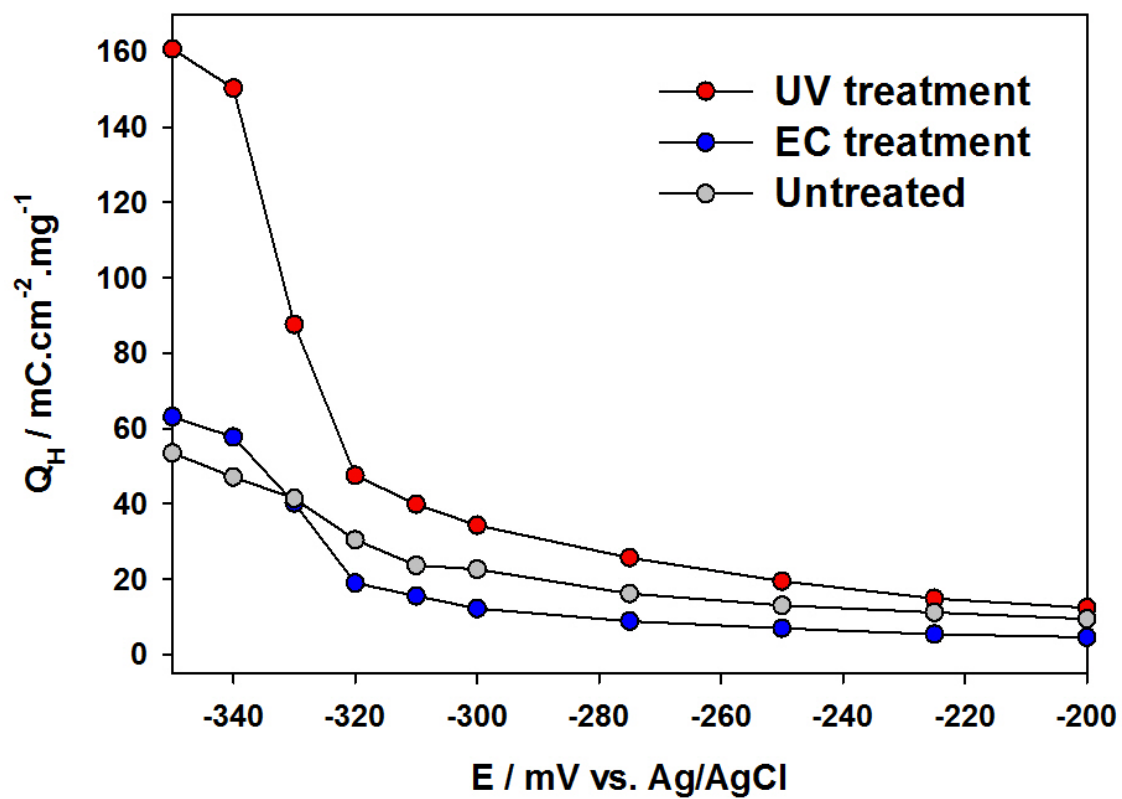


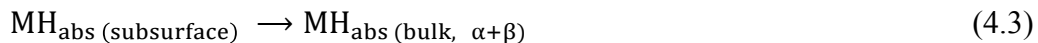
**Figure 4.6.** Hydrogen oxidation charges ( $Q_H$ ) versus potential for the prepared Pd/TiO<sub>2</sub> NT electrodes at various cathodic limits.

applied potential, -350 mV,  $Q_H$  increased as follows: UV treated Pd/TiO<sub>2</sub> NT >> EC-treated Pd/TiO<sub>2</sub> NT > un-treated Pd/TiO<sub>2</sub> NT.

The above results indicate that the applied electrode potential plays a significant role in the overall capacity for hydrogen sorption. Additionally, pretreatment methods, such as UV and EC, have the ability to increase electrocatalytic activity. In a direct comparison of peak current density ( $j$ ), the peak intensity was increased in the following order: UV treated Pd/TiO<sub>2</sub> NT >> non-treated Pd/TiO<sub>2</sub> NT > EC-treated Pd/TiO<sub>2</sub> NT.

#### 4.5.2 Kinetics of Hydrogen Electrosorption in Pd/TiO<sub>2</sub> NT Nanostructures.

Using chronoamperometry, the kinetics of hydrogen sorption into the pretreated Pd samples were examined (chronoamperometric curves;  $i - t$ , not shown here). After holding the Pd electrodes at a potential in the double layer region (200 mV) where no hydrogen adsorption/absorption occurs, the potential was stepped down to a more negative value. The transition to a more negative potential in the hydrogen sorption region, between -200 and -350 mV, allowed for the reduction of H<sup>+</sup> ions to adsorbed H atoms. The adsorbed H atoms subsequently permeated into the Pd crystal lattice. Contingent on the applied potential, a bulk phase of the adsorbed hydrogen will occur in the  $\alpha$  or  $\beta$  phase. The adsorption/absorption process can be described by the following equations:<sup>26</sup>



The time required to reach steady state electrode saturation with hydrogen was determined at various potentials, with times recorded in Figure 4.7. For each sample, as the electrode potential is decreased, the adsorption time increases to a sharp maximum. The sharp maxima occur at -

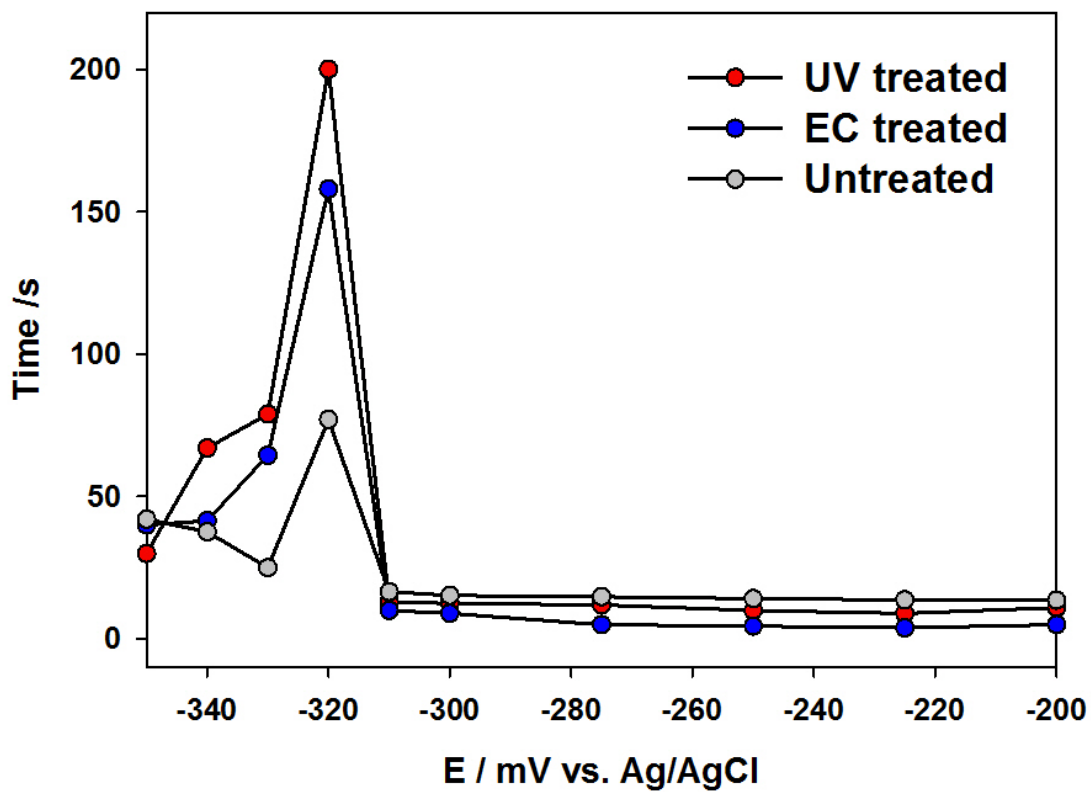


**Figure 4.7.** The time necessary for obtaining steady state saturation of the Pd/TiO<sub>2</sub> NT electrodes with absorbed hydrogen in association with potential.

320 mV for all samples. Following the maximum, there is a decrease in the saturation time. Comparing the potential for time maxima to  $Q_H$ , it was revealed that the slowest step potentials are within the phase transition region. This indicates that the  $\alpha$  to  $\beta$  phase transition is the rate-limiting step in the absorption process. With the pretreated samples the time maxima increases, which suggests a slight decrease in adsorption kinetics.

#### 4.6 Electrooxidation of Formic Acid on Pd/TiO<sub>2</sub> NT Nanostructures

The catalytic activity of the Pd nanostructures towards formic acid oxidation was examined with linear sweep voltammetry. Linear sweep voltammograms (LSVs) of the Pd electrodes recorded in 0.5 M H<sub>2</sub>SO<sub>4</sub> + 0.1 M HCOOH are displayed in Figure 4.8. As mentioned above, the overall current density is normalized by the total mass of the Pd catalyst load on the TiO<sub>2</sub> NTs. Regarding the LSVs, all three samples possess an anodic peak within the hydrogen region at a potential between -200 and 0 mV. For both the EC and UV pretreated samples, a second anodic peak is seen to follow the first. The lack of a prominent peak in the untreated sample can be attributed to poor conductivity. This second peak occurs near 100 mV for both EC and UV pretreated Pd/TiO<sub>2</sub> NT samples, indicating dominant formic acid oxidation via the direct pathway. Comparing the pretreatment methods, the UV irradiated sample possesses the highest peak current density, indicating enhanced electrooxidation of formic acid.

To further investigate the activity and stability of the electrodes, chronoamperometry was employed. High anodic current densities of formic acid oxidation occur in the potential range of 0 to 500 mV, with a peak forming at ~100 mV. Thus, chronoamperometric measurements were recorded at a held potential of 100 and 200 mV for all samples, as shown in Figure 4.9. From the chronoamperometric curves at the two applied electrode potentials, it can be seen that the UV pretreated Pd/TiO<sub>2</sub> NT sample exhibited both the maximum initial and the

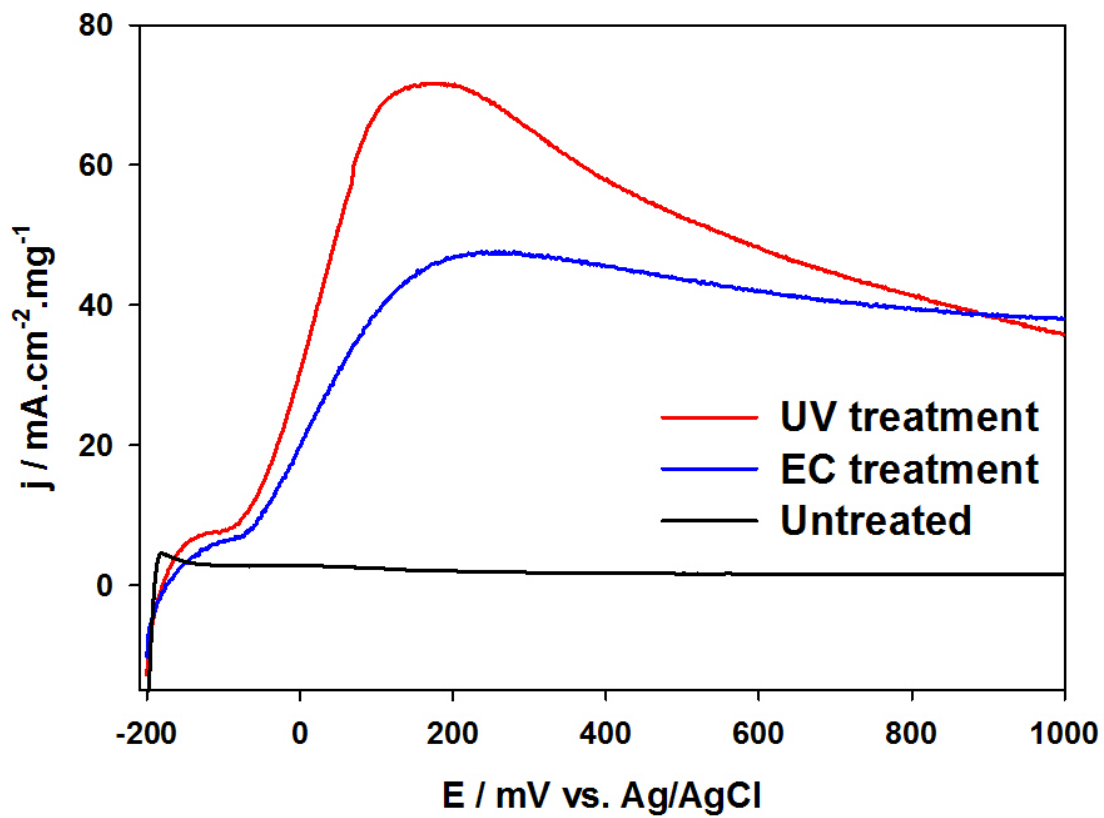


**Figure 4.8.** Linear sweep voltammograms of Pd/TiO<sub>2</sub> NT electrodes in 0.5 M H<sub>2</sub>SO<sub>4</sub> + 0.1 M HCOOH at a scan rate of 20 mV/s.

steady-state oxidation current densities, followed by the EC pretreatment. The results indicate that both UV and EC pretreated samples exhibit an improved activity for formic acid oxidation than the untreated sample, which was prepared by the same method. In Figure 4.9a and b, the curves of the pretreated samples have a sharp initial current drop, followed by a slow decay. As shown in Figure 4.9b, it is apparent that the UV pretreated samples decayed at a more rapid rate than the EC pretreated sample, indicating an increased stability of the EC pretreated sample at a higher potential. For all samples, a decrease in activity over time may be attributed to poisoning species that were present during the electrocatalytic oxidation of formic acid.<sup>27</sup>

For the characterization of the electronic properties of the TiO<sub>2</sub> nanotubes, Mott-Schottky measurements were carried out in 0.5 M H<sub>2</sub>SO<sub>4</sub>. A Mott-Schottky plot (1/C<sup>2</sup> vs. E) of the treated and non-treated samples is shown in Figure 4.10, which was obtained at a frequency of 1000 Hz. The capacitance was calculated from the imaginary component of impedance (Z<sub>i</sub>) using the relationship<sup>28</sup>:

$$Z_i = 1/2\pi fC \quad (4.4)$$

Using the Mott-Schottky plot, the donor density (N<sub>D</sub>) can be calculated from the slope according to<sup>28-30</sup>:

$$\frac{1}{C^2} = \frac{2}{e\epsilon\epsilon_0 N_D} \left( E - E_{fb} - \frac{kT}{e} \right) \quad (4.5)$$

Where *C* is the capacitance of the space charge region [F·m<sup>-2</sup>];  $\epsilon$  is the average value of the dielectric constant of the semiconductor (~120 for TiO<sub>2</sub>);  $\epsilon_0$  is the permittivity of free space charge (8.854×10<sup>-12</sup> F·m<sup>-1</sup>); and *e* is the absolute value of the electron charge (1.602×10<sup>-19</sup> C). As the donor density is dependent on the dopant level, it plays a key role in the determination of electronic conductivity. In the investigated potential range, sigmoidal plots (typical of n-type

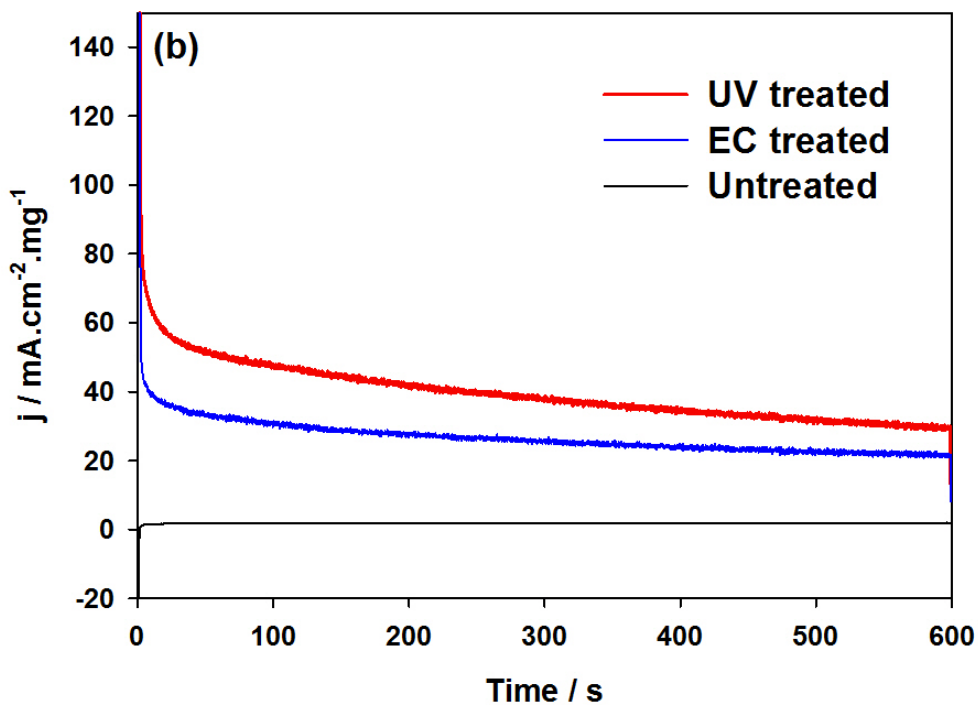
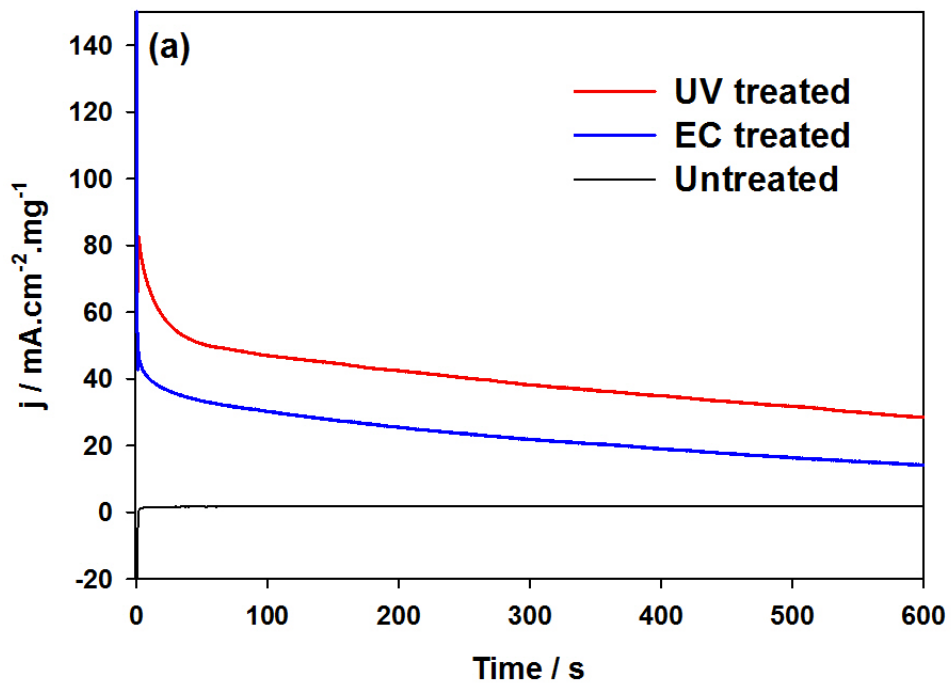


**Figure 4.9.** Amperometric *i-t* curves of HCOOH electrooxidation on the Pd/TiO<sub>2</sub> NTs in 0.5 M H<sub>2</sub>SO<sub>4</sub> + 0.1 M HCOOH at a potential of 100 mV (a) and 200 mV (b) vs. Ag/AgCl.

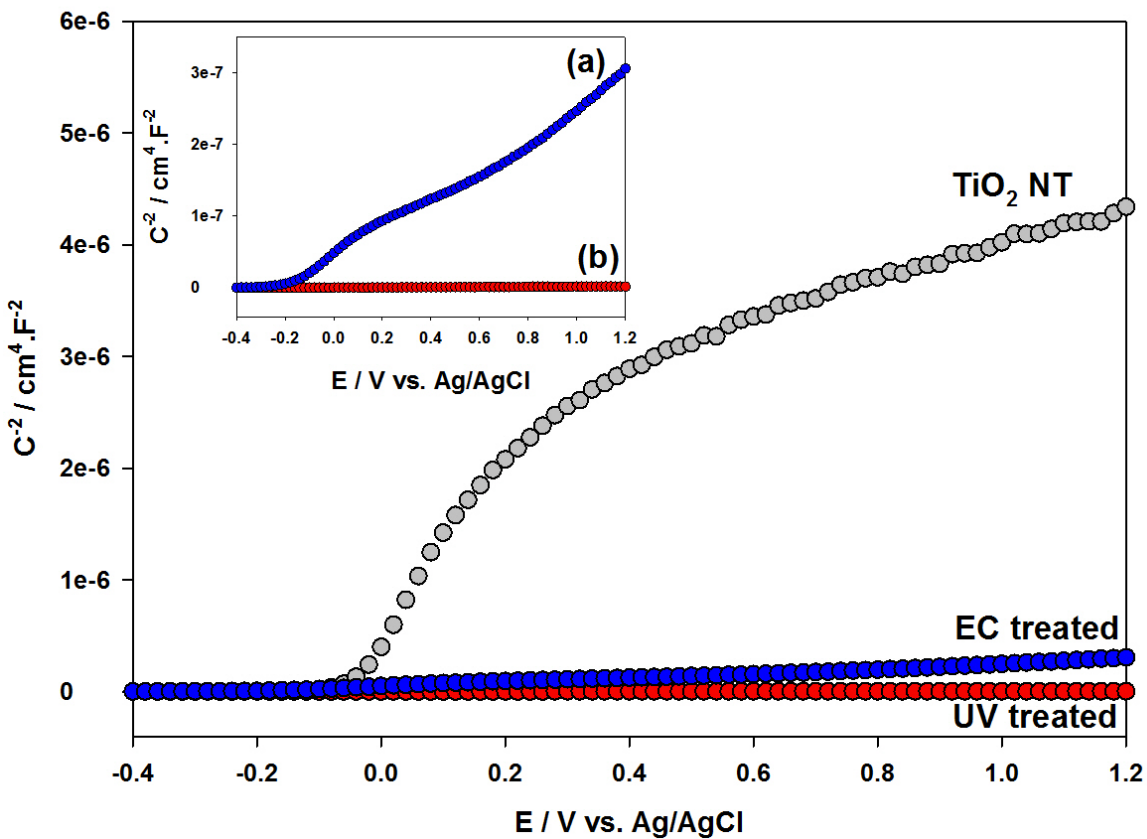


**Figure 4.10.** Mott-Schottky plot of the TiO<sub>2</sub> nanotubes in 0.5 M H<sub>2</sub>SO<sub>4</sub> at 1000 Hz without (grey) and with (blue + red) pretreatment. EC pretreatment (a) and UV pretreatment (b) of Pd/TiO<sub>2</sub> NTs Mott-Schottky plot is shown in the inset.

semiconductors) are observed. As well, a marked change of slope, close to the flat band potential (between -0.2 to 0.2 V vs. Ag/AgCl) for each sample show a good linear relationship. From this, the donor densities for the untreated TiO<sub>2</sub> NTs, EC and UV pretreated Pd/TiO<sub>2</sub> NTs were estimated to be  $1.308 \times 10^{25} \text{ m}^{-3}$ ,  $4.422 \times 10^{26} \text{ m}^{-3}$  and  $6.225 \times 10^{28} \text{ m}^{-3}$ , respectively. Comparatively, it is evident that the UV pretreatment leads to an enhanced donor density over the EC pretreatment.

#### 4.7 Conclusions

Through the course of this study, the successful enhancement of the electroactivity of TiO<sub>2</sub> nanotube supports was demonstrated. The electrochemical and ultraviolet pretreatment methods employed on TiO<sub>2</sub> NTs, exhibited a considerable increase in the double layer capacitance. Under various electrochemical conditions, the investigated pretreated Pd doped TiO<sub>2</sub> NTs showed a significant enhancement in current, proving the pretreatment methods to be successful in the modification of nanotube properties. In comparing the efficacy of pretreatment methods, the UV surpassed that of EC in all aspects of activity toward hydrogen storage and the oxidation of formic acid. However, the EC pretreated samples demonstrated a slight increase in stability compared to that of the UV pretreated samples at higher potentials. The ability to increase electroactivity following electrochemical pretreatment methods, while using only small quantities of Pd nanocatalysts, demonstrated significant improvements in electrode efficacy. The modifications articulated above make TiO<sub>2</sub> NT supports increasingly attractive and suitable for various applications that rely on enhanced electrical properties.

#### References

- (1) Rice, C.; Ha, S.; Masel, R. I.; Waszczuk, P.; Wieckowski, A.; Barnard, T. *J. Power Sources*. **2002**, *111*, 83.

- (2) Rice, C.; Ha, S.; Masel, R. I.; Wieckowski, A. *J. Power Sources*. **2003**, *115*, 229.
- (3) Yu, X.; Pickup, P. G. *J. Power Sources* **2008**, *182*, 124.
- (4) Roy, P.; Berger, S.; Schmuki, P. *Angew. Chem. Int. Ed.* **2011**, *50*, 2904
- (5) Zhang, J. W.; Wang, Y.; Jin, Z. S.; Wu, Z. S.; Zhang, Z. J. *Appl. Surf. Sci.* **2008**, *254*, 4462.
- (6) Pillai, P.; Raja, K. S.; Misra, M. *J. Power Sources* **2006**, *161*, 524.
- (7) Xu, S.; Du, A. J.; Liu, J.; Ng, J.; Sun, D. D. *Int J. Hydrogen Energy* **2011**, *36*, 6560.
- (8) Liu, Z.; Pesic, B.; Raja, K. S.; Rangaraju, R. R.; Misra, M. *Int. J. Hydrogen Energy* **2009**, *34*, 3250.
- (9) Huang, S.-Y.; Ganesan, P.; Popov, B. N. *Appl. Catal., B.* **2011**, *102*, 71.
- (10) Wang, J.; Wang, L.; Zhao, J.; Wand, B.; Wang, G. *Physica E* **2009**, *41*, 838.
- (11) Fen, L. B.; Han, T. K.; Nee, N. M.; Ang, B. C.; Johan, M. R. *Appl. Surf. Sci.* **2011**, *258*, 431.
- (12) Chen, X.; Mao, S. S. *Chem. Rev.* **2007**, *107*, 2891.
- (13) Tian, M.; Malig, M.; Chen, S.; Chen, A. *Electrochem. Commun.* **2011**, *13*, 370.
- (14) Rohani, S.; Isimjan, T.; Mohamed, A.; Kazemiaz, H.; Salem, M.; Wang, T. *Front. Chem. Sci. Eng.* **2012**, *6*, 112.
- (15) Tian, M.; Thind, S. S.; Chen, S.; Matasovsky, N.; Chen, A. *Electrochem. Commun.* **2011**, *13*, 1186.
- (16) Sang, L. X.; Zhang, Z. Y.; Ma, C. F. *Int. J. Hydrogen Energy* **2011**, *36*, 4732.
- (17) Thind, S. S.; Wu, G.; Tian, M.; Chen, A. *Nanotechnology* **2012**, *23*, 475706
- (18) Ji, Y. J.; Lin, K. C.; Zheng, H. G.; Zhu, J. J.; Samia, A. C. S. *Electrochem Commun.* **2011**, *13*, 1013.
- (19) Mazare, A.; Paramasivam, I.; Lee, K.; Schmuk, P. *Electrochem Commun.* **2011**, *13*, 1030.
- (20) Liu, Z. Y.; Zhang, X. T.; Nishimoto, S.; Jin, M.; Tryk, D. A.; Murakami, T.; Fujishima, A. *J. Phys. Chem. C* **2011**, *112*, 253.
- (21) Liu, Y. B.; Li, J. H.; Zhou, B. X.; Bai, J.; Zheng, Q.; Zhang, J. L.; Cai, W. M. *Environ. Chem. Lett.* **2009**, *7*, 363.

- (22) Varghese, O. K.; Paulose, M.; LaTempa, T. J.; Grimes, C. A. *Nano Letters* **2009**, *9*, 731.
- (23) Wen, H.; Liu, Z.; Yang, Q.; Li, Y.; Yu, J. *Electrochim. Acta* **2011**, *56*, 2914.
- (24) Adams, B. D.; Chen, A. *Mater. Today* **2011**, *14*, 282.
- (25) Gabrielli, C.; Grand, P. P.; Lasia, A.; Perrot, H. *J. Electrochem Soc.* **2004**, *151*, A1937.
- (26) Gabrielli, C.; Grand, P. P.; Lasia, A.; Perrot, H. *J. Electrochem Soc.* **2004**, *151*, A1925.
- (27) Zhou, Y.; Liu, J.; Ye, J.; Zou, Z.; Ye, J.; Gu, J.; Yu, T.; Yang, A. *Electrochim. Acta* **2010**, *55*, 5024.
- (28) Bott, A.W. *Current Separations* **1998**, *17*, 87.
- (29) Gelderman, K.; Lee, L.; Donne, S. W. *J Chem. Education* **2007**, *84*, 685.
- (30) Muñoz, A. G. *Electrochim. Acta* **2007**, *52*, 4167.

- (34) Conner, C. W.; Falconer, J. L. *Chem. Rev.* **1995**, *95*, 729.
- (35) Wang, L.; Yang, R. T. *Energy Environ. Sci.* **2008**, *1*, 268.
- (36) Cheng, H.; Chen, L.; Cooper, A. C.; Sha, X.; Pez, G. P. *Energy Environ. Sci.* **2008**, *1*, 338.
- (37) Stuckert, N. R.; Wang, L.; Yang, R. T. *Langmuir* **2010**, *26*, 11963.
- (38) Chen, X.; Zhang, Y.; Gao, X. P.; Pan, G. L.; Jiang, X. Y.; Qu, J. Q.; Wu, F.; Yan, J.; Song, D. Y. *Int. J. Hydrogen Energy* **2004**, *29*, 743.
- (39) Asmussen, R. M.; Adams, B. D.; Chen, S.; Shah, B.; Chen, A. *J. Electroanal. Chem.* **2013**, *688*, 151.
- (40) Zhuang, L.; Jin, J.; Abruña, H. D. *J. Am. Chem. Soc.* **2007**, *129*, 11033.
- (41) Babu, P. K.; Chung, J.-H.; Oldfield, E.; Wieckowski, A. *Electrochim. Acta* **2008**, *53*, 6672.

## Chapter 5. Palladium-Lead Nanoparticles deposited on TiO<sub>2</sub> Nanotubes towards Formic Acid Electro-oxidation

### 5.1 Introduction

Technological advances in modern society spawn the rapid growth of power and energy requirements for portable devices. Current portable technologies have inherent limitations that make the prospective implementation of micro fuel cells increasingly appealing. Micro fuel cells, as compared to the most competitive rechargeable batteries, are capable of delivering higher energy density power sources.<sup>1</sup> As a topic that warrants research, direct fuel cell development using organic molecules, such as methanol and formic acid, are being used as models. Both direct formic acid fuel cells (DFAFCs) and direct methanol fuel cells (DMFCs) have the potential for miniaturization.<sup>2</sup> However due to their reasonably high power output and low fuel permeation rate through the proton exchange membrane, DFAFCs reveal to be more appealing than their counterpart, DMFCs.<sup>4-6</sup>

The development of novel anode materials to facilitate formic acid oxidation is a prerequisite to enabling the application of DFAFCs. In the past, a variety of Pt based<sup>4-19</sup> and Pd based<sup>1,17,20-26</sup> catalysts have been employed for the electrochemical oxidation of formic acid. While platinum is the most widely utilized catalyst, it fails to satisfy market demands due to CO poisoning, which limits its overall activity. In contrast, Pd promotes the electrochemical reaction of formic acid oxidation via a more direct (dehydrogenation) oxidation pathway.<sup>22</sup> Despite Pd's superior performance; it has insufficient stability over time, which necessitates further improvements. Strategies for enhancing both the catalytic activity and stability of Pd include the creation of bimetallic surfaces and the introduction of an active yet stable support.<sup>22,27</sup> Ideally, through the introduction of an additional metal, the optimization of

HCOOH absorption may be attained via a combination of electronic, bifunctional and site-size effects.<sup>28</sup> Bimetallic anode catalysts often exhibit enhanced performance in comparison to pure catalysts due to the incorporated second metal, which serves to weaken CO adsorption.<sup>5,13,29</sup> During the oxidation process Pd is prone to relatively high corrosion rates, hampering its practical application in fuel cells. The introduction of a stable support such as TiO<sub>2</sub> NTs, may lead to enhanced activity as well as stability.<sup>30</sup>

In this study, a series of PdPb nanostructures with Pb contents that ranged from 0 to 20 at.%, were grown directly on TiO<sub>2</sub> NTs using a facile room temperature reduction method. The desired outcome was to decrease the overall noble metal load, while developing a more active catalyst. The electrochemical behaviours of the Pd based nanoparticles deposited on TiO<sub>2</sub> NTs in the oxidation of formic acid were investigated, revealing that small incorporations of Pb metal increase the overall activity of the Pd catalyst and reduce the noble metal load.

## 5.2 Experimental Section

A series of PdPb nanoparticles were synthesized and directly dispersed onto TiO<sub>2</sub> NT substrates using a room temperature impregnation method, as described in Chapter 2. NaBH<sub>4</sub> was used as the reducing agent and Pd(NO<sub>3</sub>)<sub>2</sub> and Pb(NO<sub>3</sub>)<sub>2</sub> served as the metal precursors. In all cases, the volumes of the precursors and introduced reducing agent added were kept constant at 5 mM and 0.125 M, respectively. Varying amounts of the Pb(NO<sub>3</sub>)<sub>2</sub> precursor were added to fabricate the desired ratio of Pd:Pb. Prior to the PdPb nanoparticle deposition, the TiO<sub>2</sub> NT substrates underwent UV pretreatment. The UV pretreatment method of the TiO<sub>2</sub> NTs was carried out as described in Chapter 2. Four coats of the prepared PdPb solution (see Chapter 2) were deposited onto the surface of the TiO<sub>2</sub> NTs. The coating loads of the electrodes were determined by weighing the TiO<sub>2</sub> NT plates prior to and after being coated with the PdPb

nanostructures with a mass balance, accurate to 0.01 mg.

The surface morphology of the fabricated samples was characterized using SEM and EDX analysis. SEM images and surface analysis via the EDX technique were obtained using a Hitachi Su-70 Schottky Field Emission SEM.

For all electrochemical experiments, a three-electrode cell system, as described in Chapter 2, was employed at room temperature. The reference electrode was Ag/AgCl (1 M KCl), and all fabricated Pd-Pb/TiO<sub>2</sub> NT electrodes were used as the working electrode. An electrolyte of 0.5 M H<sub>2</sub>SO<sub>4</sub> was employed to examine the hydrogen sorption and desorption behaviours of the electrode and an electrolyte comprised of 0.5 M H<sub>2</sub>SO<sub>4</sub> + 0.1 M HCOOH was used to investigate the activity of formic acid electrooxidation. Prior to the electrochemical experiments, ultrapure argon gas (99.999%) was bubbled through the desired electrolyte solution for approximately 15 minutes. Subsequently, the argon was allowed to flow continuously above the solution during the electrochemical measurements. Electrochemical methods used in this work included cyclic voltammetry (CV), linear sweep voltammetry (LSV), chronoamperometry (CA), and electrochemical impedance spectroscopy (EIS). Chronoamperometric measurements were carried out by initially holding the potential at 0 mV for 10 seconds, then stepping to various potentials for 10 minutes. The amplitude of modulation potentials for the EIS measurements was 10 mV. Mott-Schottky plots were measured with a VoltaLab 80 Potentiostat (PGZ402) with the potential range for capacitance measurements from -400 mV to 1200 mV vs. Ag/AgCl.

### **5.3 Surface Analysis of the TiO<sub>2</sub> NT Electrodes**

Scanning electron microscopy (SEM) was utilized to characterize the surface morphology of the prepared catalyst dispersed on the TiO<sub>2</sub> NT samples. Typical SEM images

of the Pd and PdPb<sub>5</sub> nanoparticles deposited on the TiO<sub>2</sub> NT samples are displayed in Figure 5.1. All TiO<sub>2</sub> NTs were grown directly on Ti plates via an electrochemical anodization method. The tops of the nanotubes were open with average diameters in the range of from 70 to 90 nm. The nanoparticles were dispersed onto the TiO<sub>2</sub> NT support using a room temperature sodium borohydride reduction method. The nanoparticles ranged in size from 7 to 12 nm with fairly uniform distribution among the nanotubes. The alloyed metals possessed a slightly larger nanoparticle size in comparison to their Pd and Pb counterparts. As the volume of Pb was increased in the Pd-Pb alloyed catalysts, a slight increase in nanoparticle size occurred, as well as a discernible decrease in uniform distribution. The general surface composition of the prepared anodes was characterized using EDX, following deposition (Figure 5.2). Each prepared sample displayed strong oxygen and titanium peaks, which confirmed the composition of the formed TiO<sub>2</sub> NTs. Additionally, the spectra showed the successful incorporation of the palladium-lead nanoparticles into the TiO<sub>2</sub> NT substrates.

#### **5.4 General Cyclic Voltammetric Behaviour of the Pd, Pb and PdPb/TiO<sub>2</sub> NT Nanostructures**

The electrochemical characterization of the synthesized electrodes was carried out using cyclic voltammetry in 0.5 M H<sub>2</sub>SO<sub>4</sub> at a scan rate of 20 mV/s. Figure 5.3 shows the CVs of the Pd, Pb and PdPb nanocatalysts, running from -350 to 400 mV. From the CV curves in Figure 5.3, two regions of note include the hydrogen and double layer domains. Within the hydrogen region (-350 - 0 mV), subsequent adsorption/absorption and desorption occur. Pd shows typical hydrogen adsorption/absorption and desorption behavior. As the amount of Pb is varied, changes in the peak current of hydrogen adsorption occur. Compared to pure Pd, Pd<sub>95</sub>Pb<sub>5</sub> and Pd<sub>90</sub>Pb<sub>10</sub> show an improvement in the hydrogen adsorption peak current density. Among the

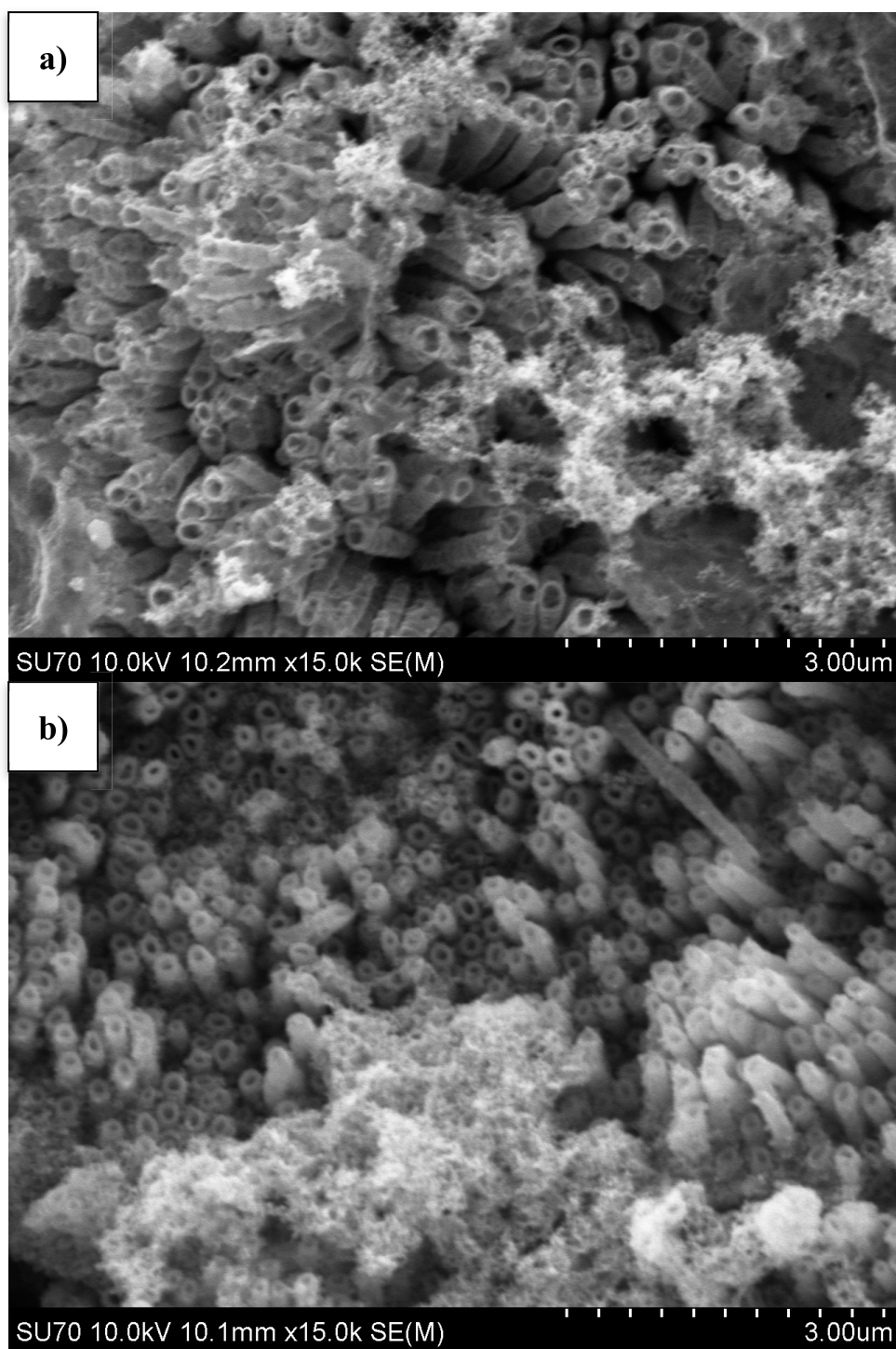


**Figure 5.1.** SEM images at 15,000× magnification of Pd (a) and PdPb<sub>5</sub> (b) deposited TiO<sub>2</sub> NT samples.

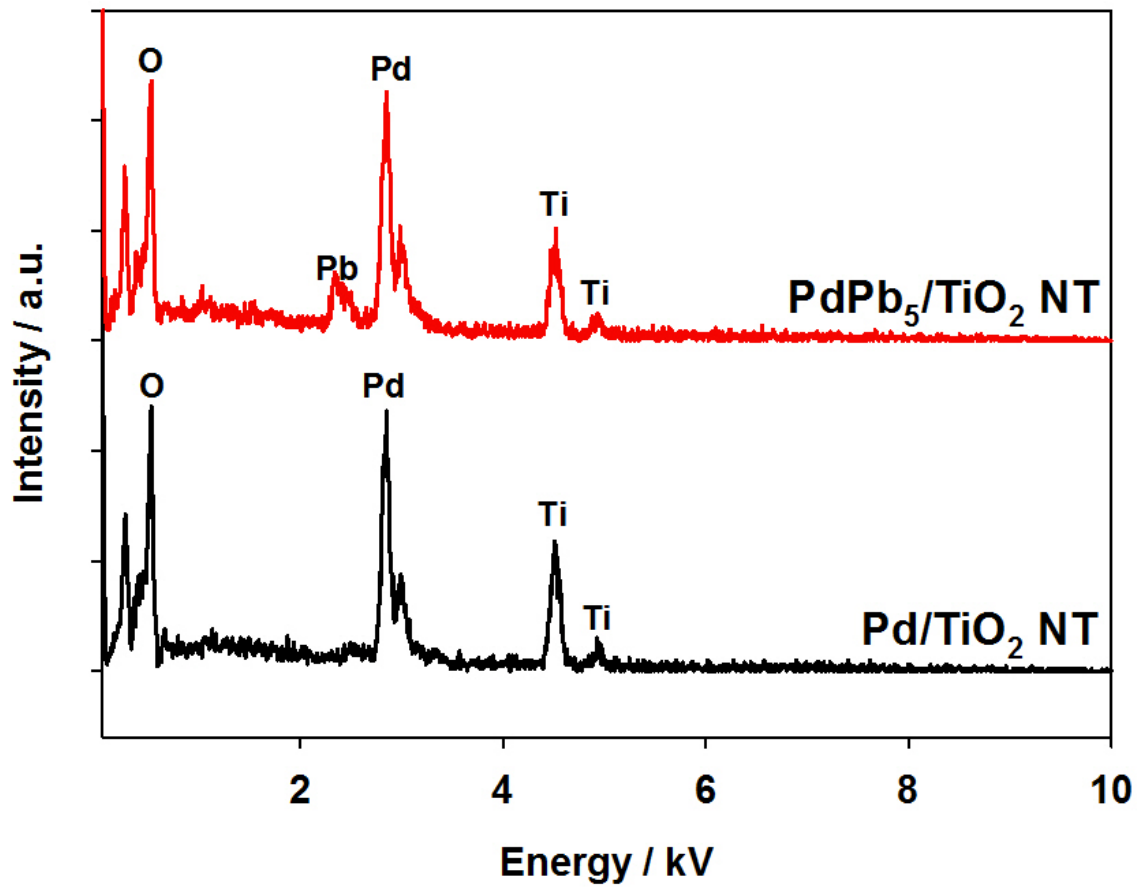


**Figure 5.2.** EDX spectra of the fabricated pure Pd and PdPb<sub>5</sub> nanoparticles deposited on the TiO<sub>2</sub> NT substrates.

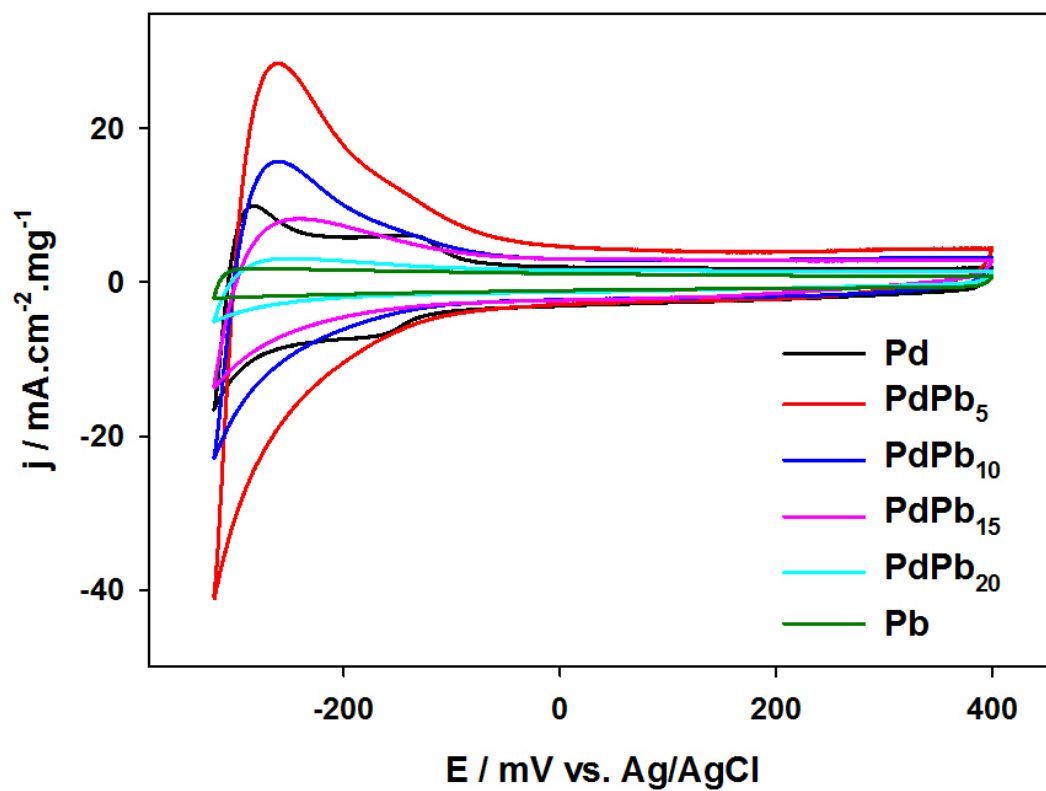


**Figure 5.3.** Cyclic voltammograms of the Pd-based nanoparticles recorded in 0.5 M  $\text{H}_2\text{SO}_4$  at a scan rate of 20 mV/s.

prepared PdPb samples, increased amounts of Pb (from 5 to 20 at.%) resulted in a decrease in the hydrogen adsorption peak current. The peak current of hydrogen adsorption diminished as the bulk percentage of Pb was increased, which indicated a reduced available electroactive surface area for hydrogen adsorption and desorption. This might be attributed to the hydrogen absorbing nature of pure Pb itself.

### **5.5 Electrooxidation of Formic Acid on Pd, Pb and PdPb/TiO<sub>2</sub> NT Nanostructures.**

To study the electrochemical activity of the nanostructured Pd/Pb samples toward the oxidation of formic acid, linear sweep voltammograms (LSVs) were recorded in 0.5 M H<sub>2</sub>SO<sub>4</sub> + 0.1 M HCOOH, running from -200 to 1000 mV (vs. Ag/AgCl) at a scan rate of 20 mV/s. The resulting LSV curves are displayed in Figure 5.4, with the overall current density normalized by the total mass of the catalyst load on the TiO<sub>2</sub> NTs. For all tested electrodes, a peak appears at approximately -200 to -50 mV within the hydrogen region, as is seen in the CVs. Following the first anodic peak a second arises with an onset of -50 mV for Pd, PdPb<sub>5</sub> and PdPb<sub>10</sub> near 100 mV. This anodic peak corresponds to the oxidation of formic acid primarily via the direct pathway.<sup>31</sup> The peak potential increased in the following order: PdPb<sub>10</sub><Pd<PdPb<sub>5</sub>. The PdPb<sub>5</sub> catalyst exhibited superior electrocatalytic activity in the oxidation of formic acid when compared to that of pure Pd. The lack of an anodic peak for Pb/TiO<sub>2</sub> NTs indicates that the Pb catalyst has no electrocatalytic activity towards formic acid electrooxidation. From this it can be concluded that the alloying degree of the Pd-Pb nanoparticles is a critical factor in the electrocatalytic activity of PdPb/TiO<sub>2</sub> NT catalysts for formic acid electro-oxidation.

Chronoamperometric analysis was carried out to further evaluate the activity and stability of the prepared electrodes for formic acid electrooxidation. Figure 5.5 shows the chronoamperometric curves for Pd, PdPb<sub>5</sub> and PdPb<sub>10</sub> at 150 mV, which corresponds to the

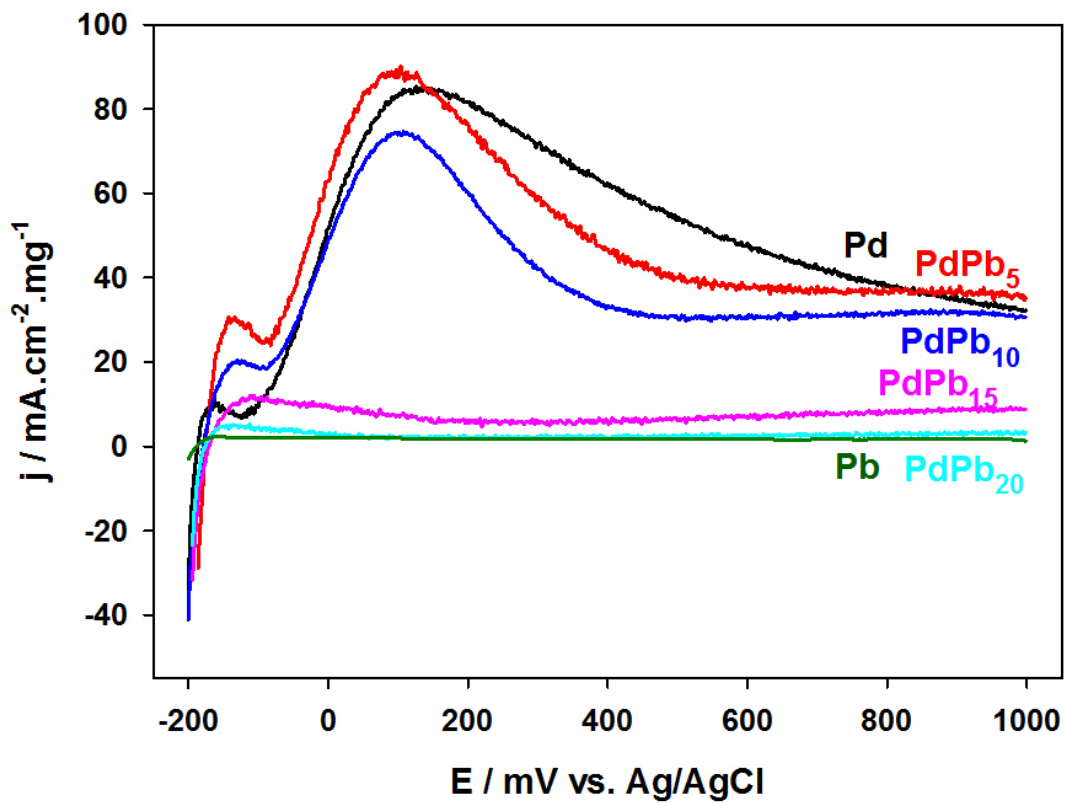


**Figure 5.4.** Linear sweep voltammograms of Pd-based/TiO<sub>2</sub> NT electrodes recorded in 0.5 M H<sub>2</sub>SO<sub>4</sub> + 0.1 M HCOOH at a scan rate of 20 mV/s.

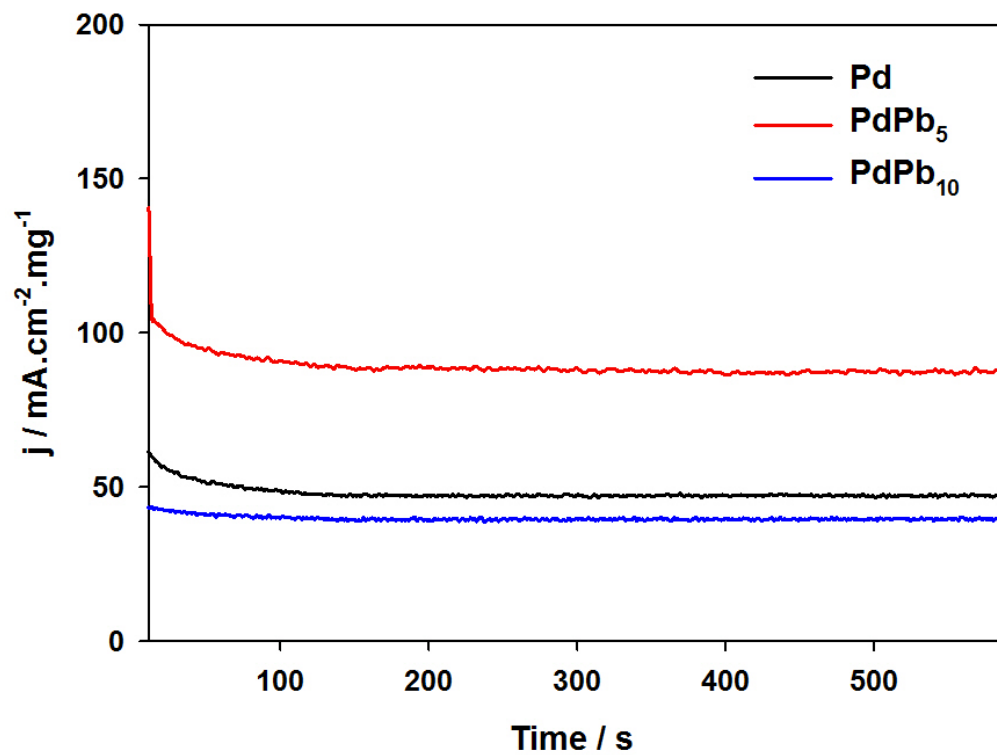


**Figure 5.5.** Chronoamperometric curves for the electrooxidation of HCOOH on the Pd and PdPb catalysts recorded in 0.5 M H<sub>2</sub>SO<sub>4</sub> + 0.1 M HCOOH at a potential of 150 mV vs. Ag/AgCl.

peak potential of the direct oxidation of formic acid. From the chronoamperometric curves, it is evident that the maximal initial and steady state oxidation current densities are obtained with PdPb<sub>5</sub>/TiO<sub>2</sub> NTs. The chronoamperometric measurements indicate that PdPb<sub>5</sub> has better activity along with stability towards formic acid oxidation. These results are in good agreement with the voltammetric results.

To further characterize the electronic properties of the TiO<sub>2</sub> nanotubes, Mott-Schottky measurements were carried out in a 0.5 M H<sub>2</sub>SO<sub>4</sub> solution at 500 Hz. The Mott-Schottky plot (1/C<sup>2</sup> vs. E) of the Pd, PdPb<sub>5</sub> and PdPb<sub>10</sub> TiO<sub>2</sub> NT samples is shown in Figure 5.6. The Mott-Schottky plot can be used to estimate the donor density (N<sub>D</sub>)<sup>32-34</sup>:

$$\frac{1}{C^2} = \frac{2}{e\epsilon\epsilon_0 N_D} \left( E - E_{fb} - \frac{kT}{e} \right) \quad (5.2)$$

Where  $C$  is the capacitance of the space charge region [F·m<sup>-2</sup>];  $\epsilon$  is the average value of the dielectric constant of the semiconductor (~120 for TiO<sub>2</sub>);  $\epsilon_0$  is the permittivity of free space charge (8.854×10<sup>-12</sup> F·m<sup>-1</sup>); and  $e$  is the absolute value of the electron charge (1.602×10<sup>-19</sup> C). The donor density is dependent on the dopant level and plays a key role in the determination of electronic conductivity. In the investigated potential range, sigmoidal plots (typical of n-type semiconductors) are observed, along with a marked change of slope near the flat band potential. Within the flat band potential there is a good linear relationship between C<sup>-2</sup> and the potential for all investigated samples. From this, the donor density for the Pd/TiO<sub>2</sub> NTs, PdPb<sub>5</sub>/TiO<sub>2</sub> NTs and PdPb<sub>10</sub>/TiO<sub>2</sub> NTs were estimated to be 1.158×10<sup>28</sup> m<sup>-3</sup>, 8.321×10<sup>27</sup> m<sup>-3</sup> and 9.572×10<sup>28</sup> m<sup>-3</sup> respectively. Comparatively, the donor density decreases in the following order: PdPb<sub>10</sub><Pd<PdPb<sub>5</sub>; a trend that is consistent with voltammetric and chronoamperometric measurements.

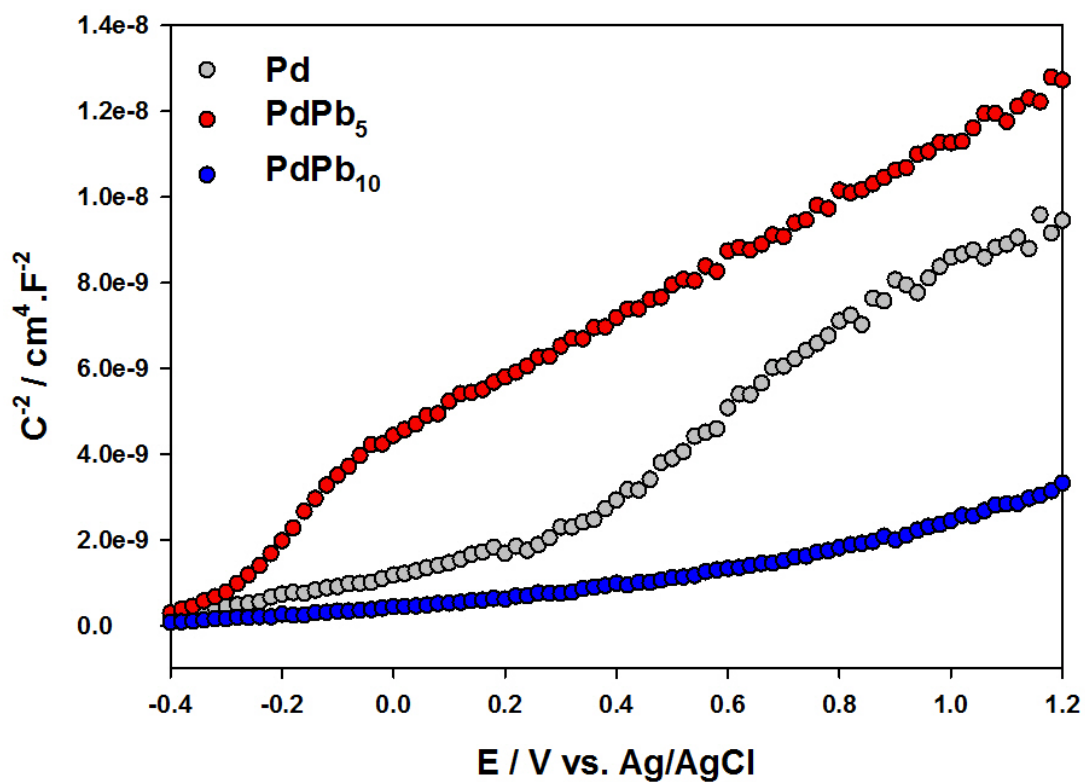


**Figure 5.6.** Mott-Schottky plot of the Pd and PdPb doped TiO<sub>2</sub> nanotubes determined in 0.5 M H<sub>2</sub>SO<sub>4</sub> at 500 Hz following UV pretreatment.

## 5.6 Conclusions

PdPb nanoparticles were easily dispersed onto the surface of TiO<sub>2</sub> NTs using a facile sodium borohydride reduction method at room temperature. The enhancement of electrochemical activity toward the electrooxidation of formic acid was observed in both voltammetric and chronoamperometric measurements for PdPb<sub>5</sub>/TiO<sub>2</sub> NTs in comparison to that of pure Pd. The successful reduction of the Pd noble metal load was achieved at an optimal percentage of 5% Pb, revealing an increased current density for formic acid oxidation.

## References

- (1) Brandt, K.; Steinhausen, M.; Wandelt, K. *J. Electroanal. Chem.* **2008**, *616*, 27.
- (2) Kim, H. S.; Morgan, R. D.; Gurau, B.; Masel, R. I. *J. Power Source.* **2009**, *188*, 118.
- (3) Wang, R.; Liao, S.; Ji, S. *J. Power. Source.* **2008**, *180*, 205.
- (4) Rice, C.; Ha, S.; Masel, R. I.; Waszczuk, P.; Wieckowski, A.; Barnard, T. *J. Power. Source.* **2002**, *111*, 83.
- (5) Chen, W.; Xu, L.-P.; Chen, S. *J. Electroanal. Chem.* **2009**, *631*, 36.
- (6) Baik, S. M.; Han, J.; Kim, J.; Kwon, Y. *Int. J. Hydrogen Energy* **2011**, *36*, 14719.
- (7) Chumillas, S.; Busó-Rogero, C.; Solla-Gullón, J.; Vidal-Iglesias, F. J.; Herrero, E.; Feliu, J. M. *Electrochem. Commun.* **2011**, *13*, 1194.
- (8) Herrero, E.; Llorca, M. J.; Feliu, J. M.; Aldaz, A. *J. Electroanal. Chem.* **1995**, *394*, 161.
- (9) Liu, W.; Huang, J. *J. Power Source.* **2009**, *189*, 1012.
- (10) Choy M., M.; Hahn, F.; Léger, J.-M.; Lamy, C.; Ortega, J. M. *Thin Solid Films* **2007**, *515*, 3611.
- (11) Ren, F.; Zhou, W.; Du, Y.; Yang, P.; Wang, C.; Xu, J. *Int. J. Hydrogen Energy* **2011**, *36*, 6414.
- (12) Seland, F.; Tunold, R.; Harrington, D. A. *Electrochimica Acta* **2008**, *53*, 6851.

- (13) Tripković, A. V.; Popović, K. Dj.; Stevanović, R. M.; Socha, R.; Kowal, A. *Electrochem. Commun.* **2006**, *8*, 1492.
- (14) Wang, Z.; Qiu, K. *Electrochem. Commun.* **2006**, *8*, 1075.
- (15) Winjobi, O.; Zhang, Z.; Liang, C.; Li, W. *Electrochimica Acta* **2010**, *55*, 4217.
- (16) Yi, Q.; Chen, A.; Huang, W.; Zhang, J.; Liu, X.; Xu, G.; Zhou, Z. *Electrochem. Commun.* **2007**, *9*, 1513.
- (17) Yi, Q.; Huang, W.; Liu, X.; Xu, G.; Zhou, Z.; Chen, A. *J. Electroanal. Chem.* **1995**, *394*, 161.
- (18) Wang, X.; Hu, J.-M.; Hsing, I.-M. *J. Electroanal. Chem.* **2004**, *562*, 73.
- (19) Zhou, W.; Xu, J.; Du, Y.; Yang, P. *Int. J. Hydrogen Energy* **2011**, *36*, 1903.
- (20) Dai, L.; Zou, S. *J. Power Source.* **2011** *196*, 9369.
- (21) Hoshi, N.; Nakamura, M.; Kida, K. *Electrochem. Commun.* **2007**, *9*, 279.
- (22) Park, I.-S.; Lee, K.-S.; Yoo, S. J.; Cho, y.-H.; Sung, Y.-E. *Electrochimica Acta* **2010**, *55*, 4339.
- (23) Wang, Y.; Wu, B.; Gao, Y.; Tang, Y.; Lu, T.; Xing, W.; Liu, C. *J. Power Source.* **2009**, *192*, 372.
- (24) Yi, Q.; Huang, W.; Liu, X.; Xu, G.; Zhou, Z.; Chen, A. *J. Electroanal. Chem.* **2008**, *619-620*, 197.
- (25) Zhang, G.; Wang, Y.; Wang, X.; Chen, Y.; Zhou, Y.; Tang, Y.; Lu, L.; Bao, J.; Lu, T. *Appl. Catal. B: Environ.* **2011**, *102*, 614.
- (26) Zhu, Y.; Kang, Y.; Zou, Z.; Zhou, Q.; Zheng, J.; Xia, B.; Yang, H.
- (27) Qu, W.-L.; Wang, Z.-B.; Sui, X.-L.; Gu, D.-M.; Yin, G.-P. *Int. J. Hydrogen Energy* **2012**, *37*, 15096.
- (28) Arenz, M.; Stamenkovic, V.; Schmidt, T. J.; Wandelt, K.; Ross, P. N.; Markovic, N. M. *Phys. Chem. Chem. Phys.*, **2003**, *5*, 4242.
- (29) Haan, J. L.; Stafford, K. M.; Morgan, R. D.; Masel, R. I. *Electrochimica Acta* **2010**, *55*, 2477.
- (30) Tian, M.; Malig, M.; Chen, S.; Chen, A. *Electrochem. Commun.* **2011**, *13*, 370.

(31)Liu, Z.; Hong, L.; Tham, M. P.; Lim, T. H.; Huixin, J. *J. Power Source*. **2006**, *161*, 831.

(32)Bott, A.W. *Current Separations* **1998**, *17*, 87. *Electrochem. Commun.* **2008**, *10*, 802.

(33)Gelderman, K.; Lee, L.; Donne, S. W. *J. Chem. Education* **2007**, *84*, 685.

(34)Muñoz, A. G. *Electrochim. Acta* **2007**, *52*, 4167.

## Chapter 6. Summary and Future Work

The unique catalytic and hydrogen adsorbing properties of Pd-based nanomaterials make them attractive for the technological development of a hydrogen-based economy. Advances in Pd-based material development show promise in hydrogen purification, hydrogen storage, and fuel cell catalysis applications. A room temperature impregnation method was employed to synthesize the Pd-containing nanomaterials that were examined in this work. All the synthesized Pd-based materials were characterized using a combination of surface analytical techniques, electrochemical methods and gas adsorption. The primary results obtained during the course of this M.Sc. project are summarized below.

### 6.1 Synthesis and Electrochemical Study of Pd-based Tri-metallic Nanoparticles for Enhanced Hydrogen Storage

The success of acceptable hydrogen storage capacities on high surface area carbon materials at ambient temperatures requires the combination of both physisorption and chemisorption. Despite solely relying on physisorption for hydrogen uptake in carbon, the dispersal of transition metal catalysts on carbon materials significantly enhances hydrogen uptake at ambient temperatures via the process of hydrogen spillover in the gas phase. In Chapter 3, hydrogen electrosorption onto the activated carbon materials modified with Pd, PdAg<sub>5</sub>Cd<sub>15</sub>, PdAg<sub>10</sub>Cd<sub>10</sub>, PdAg<sub>15</sub>Cd<sub>5</sub>, PdAg<sub>20</sub> and PdCd<sub>20</sub> dissociation catalysts was investigated in an acidic medium using cyclic voltammetry and chronoamperometry. The incorporation of Cd and Ag into the Pd of the tri-metallic alloy strongly impacts its capacity of hydrogen sorption. It was seen that at maximized Ag or Cd contents (at an atomic +15%), the catalytic hydrogen sorption capacity decreased. It was found that the optimized composition of the Pd-Ag-Cd alloys was Pd<sub>80</sub>Ag<sub>10</sub>Cd<sub>10</sub>, with the highest hydrogen sorption capacity at a hydrogen

desorption charge ( $Q_H$ ) of  $18.49 \text{ C/cm}^2 \cdot \text{mg}$ . Additionally, through a comparison of supported and non-supported Pd-Ag-Cd catalysts, it was found that synergistic effects between the metal and carbon drastically increased the capacity for hydrogen storage. With increased kinetics and a decrease in the phase transition, the significant enhancement of hydrogen sorption, in comparison to the Pd-Ag and Pd-Cd bi-metallic alloys, was further demonstrated. These findings verified that Pd-Ag-Cd catalysts are attractive candidates in serving as hydrogen dissociation catalysts for applications in both hydrogen purification and storage.

## **6.2 Enhanced Electrocatalytic Activity of Pd Nanoparticle Modified TiO<sub>2</sub> Nanotubes: A Comparison of UV and EC Pretreatment Methods**

Polymer electrolyte membrane fuel cells (PEMFCs) have emerged among the top candidates for applications in the automotive and portable electronic device sectors. Serving as promising solutions for future energy strategies, fuel cells require advanced electrocatalyst material development for hydrogen purification, hydrogen storage and formic acid oxidation. Titania nanotubes (TiO<sub>2</sub> NTs) with large surface areas, low cost and high stability appeal to the fuel cell masses as a suitable support material. Although TiO<sub>2</sub> NTs present many advantages, low conductivity issues will need to be addressed as a prerequisite to their acceptance as a suitable support. In Chapter 4, the investigation of the effects of UV light and electrochemical pretreatment methods on TiO<sub>2</sub> NTs is studied. Using Pd as the dispersed catalyst, Pd/TiO<sub>2</sub> NT electrodes were examined in an acidic medium for hydrogen electrosorption and formic acid electrooxidation. Both UV and electrochemical pretreatment methods enabled significant enhancements in the electroactivity of the TiO<sub>2</sub> NT substrates, with UV pretreatments dominating overall efficacy. The enhancement of electroactivity, following pretreatments methods, resulted in the effective reduction of typical noble metal loads. The above

modifications make the TiO<sub>2</sub> NT supports increasingly suitable for various applications that rely on enhanced electrical properties.

### **6.3 Palladium-Lead Nanoparticles Deposited on TiO<sub>2</sub> Nanotubes towards Formic Acid Electro-oxidation**

Direct formic acid micro fuel cells for portable device applications require further development of anode materials to facilitate improved electrooxidation. In Chapter 5, the formic acid electrooxidation properties of Pd-Pb/TiO<sub>2</sub> NT alloys with a 0 to 20 at.% were studied. The PdPb nanoparticles were easily dispersed onto the surface of UV pretreated TiO<sub>2</sub> NTs using a facile sodium borohydride reduction method at room temperature. Compared to pure Pd, Pd<sub>95</sub>Pb<sub>5</sub> and Pd<sub>90</sub>Pb<sub>10</sub> catalysts showed improved electrocatalytic abilities. Compositions of PdPb that exceeded 10% Pb content resulted in diminished efficacies, which was indicative of smaller available electroactive surface areas. The incorporation of small amounts of Pb metal into Pd catalysts results in an increase in catalytic activity, followed by the reduction of the overall noble metal load.

### **6.4 Closing Remarks and Future Work**

In summary, tri-metallic PdAgCd nanomaterials have been directly dispersed onto activated carbon and coated on glassy carbon electrodes. The ideal catalyst composition was determined to be Pd<sub>80</sub>Ag<sub>10</sub>Cd<sub>10</sub>, which exhibited the highest capacity for hydrogen sorption. This PdAgCd catalyst outperformed Pd, PdAg<sub>20</sub> and PdCd<sub>20</sub> nanoparticles.

The performance of Pd catalysts dispersed on UV light and electrochemically pretreated TiO<sub>2</sub> NTs has been investigated. It was found that both UV and electrochemical pretreatment

methods caused significant enhancements in the electroactivity of the TiO<sub>2</sub> NT substrate, with UV pretreatments dominating overall efficacy.

PdPb (0 to 20 at.%) nanoparticles were successfully dispersed onto the surface of UV pretreated TiO<sub>2</sub> NTs and examined for their electrocatalytic activity towards the oxidation of formic acid. The electrochemical catalytic activity of Pd in the oxidation of formic acid was slightly improved with the incorporation of 5% Pb.

It is apparent that limitations imposed by the cost of modern technology strongly impede progress towards a commercialized hydrogen economy. Development of anode materials is a critical element toward further advancements in this area. The results of this M.Sc. project indicate that Pd-based materials are promising for applications in stationary power supplies, personal transportation, and small portable electronics as hydrogen storage materials and dissociation catalysts. Specific molecular composition, adjusted through the alloying of Pd with other metals, appears to be critical for anode material enhancement. Along with catalyst composition, factors such as support materials are also influential in varying the number of available active sites and for the provision of enhanced stabilization. Future work may focus on the following aspects: (i) optimization of Pd-based alloy geometry, composition and structure toward a further enhancement of their catalytic activity and stability; (ii) further exploration of variations in catalyst synthesis processes to enhance catalytic activity; and (iii) further investigation of novel catalyst morphologies to enhance catalytic activity.